**Calorimetric Systems to Explore Radiative Thermal Transport and the Thermodynamics of Hydrogen ($H_2$) Reactions for Energy Utilization**

by

Ju Won Lim

A dissertation submitted in partial fulfillment
of the requirements for the degree of
Doctor of Philosophy
(Materials Science and Engineering)
in the University of Michigan
2024

Doctoral Committee:

Professor Pramod Sangi Reddy, Co-Chair
Professor Edgar Meyhofer, Co-Chair
Professor Vikram Gavini
Associate Professor Xiaogan Liang

Ju Won Lim

juwonlim@umich.edu

ORCID iD: 0000-0001-7021-3173

**Acknowledgements**

Throughout my PhD journey, I believe that I underwent substantial personal growth in various aspects. Research is an ongoing and demanding endeavor, as it entails developing novel concepts and objectively validating them. Moreover, research demanded a sustained investment of time and effort over an extended period, often without immediate gratification, given the need to delve into uncharted territories. During my research, I encountered numerous difficulties that left me feeling frustrated. To overcome those challenges, I faced various situations in which I needed to understand the process of accurately identifying a problem, analyzing the objective reasons behind it, and taking on the challenge of solving it. In the end, I realized that with each progressive step, it became increasingly important to venture beyond my comfort zone, leading me to engage in introspection and personal development in many ways. Stepping out of my comfort zone was indeed daunting, but the sense of fulfillment I experienced upon conquering that fear was immeasurable, contributing significantly to my mental maturity. The successful completion of my PhD at the University of Michigan is attributed to the exceptional support of my advisors and colleagues, whose contributions made my academic journey possible.

Prof. Pramod Reddy presented an ambitious research vision that addressed significant questions, inspiring me to tackle important yet challenging research inquiries. It has been a delightful experience learning from him over these years. I've acquired extensive knowledge in nanofabrication, experimentation, electrical/mechanical engineering, and the enhancement of logical thinking throughout my PhD program. I am immensely grateful to Prof. Reddy for his

guidance, support, and mentorship throughout this journey. I also want to express my deep gratitude to my co-advisor, Prof. Edgar Meyhofer, for his constant moral support and guidance, along with his exceptional skill in fixing malfunctioning instruments and circuits during the difficulties I faced when trying to resolve unsuccessful experiments. His profound insights and extensive knowledge across various fields served as valuable guidance whenever I encountered seemingly insurmountable research obstacles. Additionally, I wish to express my gratitude to my committee members, Prof. Vikram Gavini and Prof. Xiaogan Liang, for dedicating their time and providing valuable suggestions to improve my research and dissertation. Their challenging questions during my dissertation proposal exam pushed me to delve into deeper levels of thinking.

I would also like to convey my appreciation to Dr. Rohith Mittapally, both as a mentor and a friend. When we embarked on our 'near-field thermophotovoltaics project,' he provided consistent support and shared his extensive expertise in nanofabrication. Prof. Amin Reihani played a pivotal role in helping my calorimeter achieve research objectives that approached the limits of resolution. He has been my research mentor and friend, consistently demonstrating care and sharing his extensive knowledge of nanofabrication gained through years of experience. I am also indebted to my lab colleagues and former members, including Prof. Dakotah Thompson, Dr. Sunghoon Hur, Dr. Shen Yan, Dr. Zhongyong Wang, Dr. Evan Fleming, Yuxuan Luan, Ayan Majumder, Kanishka Panda, Audrey Rose Gutierrez, Jian Guan, Ratul Mali, and colleagues. I'd like to convey my heartfelt gratitude to all my family and friends in both South Korea and Michigan.

I am grateful for the sources of funding that have made the projects in this work possible. I am thankful for support from DOE-BES through a grant from the Scanning Probe Microscopy Division under award No. DESC0004871 (experiments and analysis), and support from the Army

Research Office under award No. MURI W911NF-19-1-0279 (fabrication of devices, analysis). Additionally, this work was pursued with support from Google LLC and the Anthropocene Institute, as well as the Rackham Predoctoral Fellowship from the University of Michigan.

Finally, I wish to convey my profound appreciation to my family for their immeasurable affection. Both my parents and my brother have stood as unwavering sources of support, consistently supplying me with the resilience and resolve to navigate life's journey. Their steadfast encouragement and love have played a pivotal role in helping me overcome the hurdles I encountered during my graduate studies, ultimately contributing to my personal growth and development.

## Table of Contents

## List of Tables

## List of Figures

## Abstract

Thermal radiation plays a crucial role in various technological applications, ranging from thermal energy conversion devices to the manufacturing of electronic devices. In this dissertation, I discuss how nanoscale thermal radiation can be controlled via thin films and how phase transitions in thin films can be employed to control the flow of heat. Moreover, I describe how novel calorimetric tools can be developed to probe the thermodynamics of chemical reactions with nanomaterials.

In Chapter 1, prior to presenting my research, I discuss background material covering the quantification of heat flow in calorimetry, conceptual discussions regarding the blackbody limit, hydrogenation reactions of transition metals, and related topics.

In Chapter 2, I outline how I developed a photonic thermal transistor comprising a source-drain device (hot and cold electrodes) and a vanadium oxide-based planar gate electrode, whose dielectric properties can be adjusted by changing its temperature. I demonstrate that when the gate, located near (< ~1 μm) the source-drain device, undergoes a metal-insulator transition, the radiative heat transfer between the source and drain changes by a factor of three. These findings are supported by detailed calculations that highlight the mechanism of thermal modulation. Furthermore, in contrast to past thermal transistors, for which the transition time varies from minutes to hours depending on the device configuration, I show that this photonic thermal transistor features a much faster switching time (~500 ms as opposed to minutes) due to the small thermal mass of the nanoscale devices employed in the work. The advances described here are

expected to open new opportunities for designing photonic thermal circuits or computing systems for advanced thermal management.

In Chapter 3, I present my exploration of radiative heat transfer (RHT) between objects separated by nanometer-sized vacuum gaps to measure the thickness-dependence of RHT between planar nanofilms. This phenomenon is remarkably distinct from far-field thermal radiation and can exceed the blackbody radiation limit by orders of magnitude. I report direct measurements of the thickness-dependence of RHT between two planar magnesium fluoride nanofilms (thickness ranging from 20 to 500 nm) performed using microfabricated devices and a custom-developed nanopositioner. These results directly demonstrate, for the first time, that nanofilms have the capability to enhance thermal radiation by up to 800 times beyond the blackbody limit. Moreover, they prove to be as effective as bulk materials when the dimensions of the nanoscale gaps are smaller than the thickness of the nanofilm. Additionally, I show that computations based on fluctuational electrodynamics align well with the observed gap-size dependence of the heat transfer coefficient for films of various thicknesses. These calculations not only show agreement between theory and experimental results but also offer a physical understanding of the observed dependence. The techniques and insights derived from the experiments presented in this study pave the way for a systematic exploration of novel thin films for near-field thermal and radiative energy systems.

In Chapter 4, I describe the construction of a calorimetric system with a resolution of <3 $\mu W/\sqrt{Hz}$ and long-term stability of <4 μW/hour. The study of calorimetry involving reactions with nanomaterials is currently of significant interest, demanding high-resolution heat flow measurements and long-term thermal stability. Using the custom-built high-resolution calorimetric system I developed, I measure the heat output during the absorption of hydrogen in Pd

nanoparticles. By monitoring the heat output associated with the conversion of Pd metal into its metal-hydride phase, I describe the thermodynamics of the hydrogenation of Pd. This calorimetric system enables the direct measurement of heat energy during the hydrogenation process, providing an opportunity to explore both the thermodynamics and kinetics associated with the reaction.

Finally, in Chapter 5, I provide a summary of my work and discuss future research directions and ideas to advance the scope of my findings. This work paves the way for exploring hydride-based hydrogen storage systems by storing substantial amounts of hydrogen in hydride nanomaterials. These findings will open up the possibility of hydrogen utilization for fuel cells, which serve as a clean and sustainable energy source for various applications.

# Chapter 1 Overview

## 1.1 Perspective

The development of sustainable energy sources is critical for various purposes, including mitigating the environmental impact of fossil fuels, reducing carbon emissions, and fostering the development of industries and overall economic prosperity[1-4]. Among various energy sources, research into the utilization of thermal energy has garnered significant attention, considering the large amounts of heat waste that are dissipated into the environment[5-8]. To utilize thermal energy effectively, studying the control of heat flow and the measurement of generated energy is necessary for conducting quantitative analysis and effectively managing thermal energy. In this context, my work specifically focuses on controlling thermal flux and measuring released thermal energy, both of which are closely related to addressing significant global energy demand.

One promising way to harness thermal energy is to develop devices that function as switches to control heat flow[9, 10]. To utilize thermal energy by controlling heat flow, a photonic thermal transistor—a device that switches the flow of photons based on temperature or thermal changes—has been theoretically explored[11-15]. Thermal transistors can be utilized in thermoelectric generators to harvest waste heat and convert it into usable electrical energy. In this application, the thermal transistor regulates the flow of heat from a hot source (such as an engine or industrial process) to a cooler environment. The development of a thermal transistor promises breakthroughs by offering a means to actively control and modulate the flow of heat, providing a significant impact on the fields of thermal management, electronics, and energy harvesting[13-15]. This opens

up possibilities for sustainable and efficient energy conversion, particularly in environments where temperature differentials exist, such as in industrial applications or electrical appliances.

Another crucial aspect in the field of thermal energy involves the development of a calorimetric system to precisely measure and estimate the generated heat[16, 17], allowing for the quantification of thermal energy. For instance, when hydrogen reacts with a transition metal, the transformation into a hydride is an exothermic process due to the increased stability of metal hydrides compared to the individual metal and hydrogen atoms[18, 19]. That is, the increased stability of the metal hydride compared to its constituents leads to the release of heat during the formation process. Calorimetric systems enable accurate measurement of released heat during this reaction, providing essential information associated with the reaction and thermal energy generation[20, 21]. High-resolution calorimeters allow for further study of the thermodynamic properties of materials during the hydrogenation reaction, facilitating a deeper understanding of the mechanism of thermal energy generation. Additionally, calorimetry systems support kinetic studies by providing real-time data on heat changes throughout the reaction, aiding in the identification of the hydrogen uptake and release processes[22, 23].

Overall, the work presented in this dissertation explores controlling the heat currents and measuring the generated thermal energy, emphasizing their potential in thermal energy harvesting and utilization. Furthermore, it delves into calorimetry systems to precisely measure the generated heat energy during hydrogen absorption reactions, suggesting the possibility of utilizing hydrogen-related technologies. By advancing our understanding of thermal science and engineering, designing materials, and implementing innovative technologies, we can pave the way for a more sustainable and energy-efficient future.

## 1.2 Background

Thermal energy originating from the sun, geothermal, biomass, and nuclear sources stands out as a prominent resource, drawing considerable attention for its potential applications in heating, electricity generation, and industrial processes[24, 25]. Its pivotal role extends across various industrial, residential, and technological applications, influencing the methods by which we harness, manage, and utilize heat energy. Today, thermal control is integral to numerous sectors, influencing the efficiency, sustainability, and safety of various processes. In industrial settings, precise heat management is essential for optimizing manufacturing processes, ensuring product quality, and minimizing energy waste[26, 27].

In thermal science, heat transfer represents the flow of energy from a higher temperature to an object with a lower temperature[28, 29]. Heat transfer can occur through diverse mechanisms, including conduction, convection, and radiation, mediated by carriers such as electrons, phonons, and photons[29]. Among these methods, radiative heat transfer occurs through the transfer of heat via electromagnetic waves, specifically infrared waves at room temperature (*e.g.*, ~10 μm at 300 K)[30, 31]. Unlike conduction and convection, radiation does not require a medium for heat transfer because heat is emitted in the form of electromagnetic waves, capable of traveling through a vacuum.

### *1.2.1 Quantifying Heat Flow in Calorimetry*

A conceptual illustration of a calorimeter's heat flow is presented in Figure 1-1. The calorimeter, when modeled using a simplified lumped parameter approach, appears as a structure linked to its environment through a thermal connection characterized by thermal conductance ($G_{Th}$). A heat input power, $q_{Th}$, results in a corresponding temperature change, $\Delta T$, within the device. The quantification of the heat input is achieved using equation (1-1)[32]:

$$q_{\mathrm{Th}} = G_{\mathrm{Th}} \times \Delta T \qquad (1\text{-}1)$$

The equation emphasizes that achieving high heat flow resolution in calorimeter design necessitates low thermal conductance ($G_{\mathrm{Th}}$) and highly sensitive thermometry. To measure the temperature change, platinum (Pt) is a common material used as a resistance thermometer, known for its linear change in resistance ($R$) within small temperature variations ($T$)[33, 34]. The temperature coefficient of resistance ($TCR$) for platinum is approximately $1.8\times10^{-3}$ $K^{-1}$ at room temperature, where $TCR = (dR/dT) \times R^{-1}$.

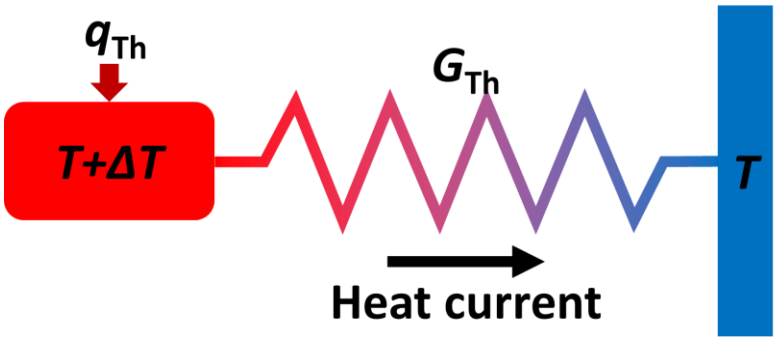


Figure 1-1. The diagram illustrates a calorimeter system operating at temperature $T$, where bodies are interconnected to facilitate heat flow, identified by thermal conductance $G_{\mathrm{Th}}$. The introduction of heat input power, indicated as $q_{\mathrm{Th}}$, into the device results in a temperature rise denoted by $\Delta T$.

Among various heat transfer mechanisms, thermal radiation is one of the fundamental processes. Thermal radiation, a phenomenon occurring in substances with temperatures higher than absolute zero, entails the emission of electromagnetic waves[31]. This emission signifies the transformation of thermal energy into electromagnetic energy, where thermal energy corresponds to the kinetic energy resulting from the random movements of atoms and molecules in matter. The kinetic interactions among charged particles within atoms and molecules, specifically protons and electrons, induce charge acceleration and dipole oscillation, leading to the emission of photons

that carry energy away from the source. In thermal radiation, heat current moves from a higher temperature to a lower temperature through the transmission of photons.

The power radiated from an object is determined by the Stefan-Boltzmann law of radiation, as described in the equation (1-2)[35]:

$$q_{Th} = \sigma \epsilon A T^4 \qquad (1\text{-}2)$$

where $\sigma$ is the Stefan-Boltzmann constant, $\epsilon$ is the emissivity of the material, $T$ is the absolute temperature of the object, and $A$ is the surface area of the object. The total energy radiated per unit surface area of an object is directly proportional to the fourth power of the object's absolute temperature.

### *1.2.2 Two Exceptional Scenarios Exceeding the Blackbody Limit*

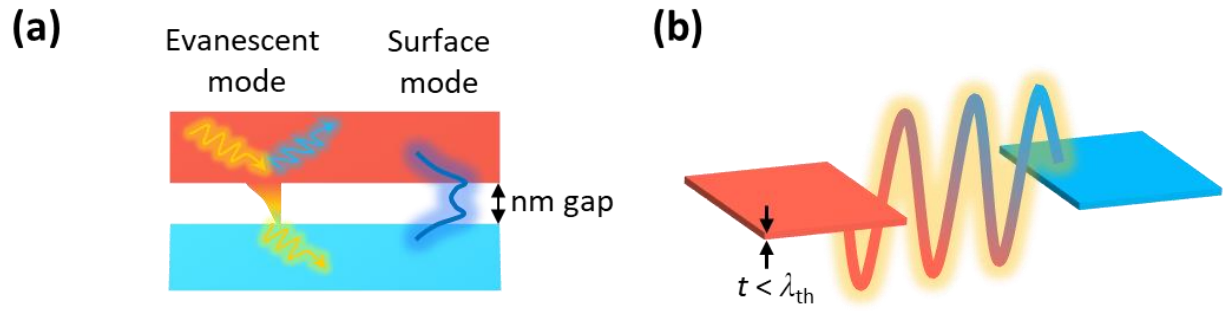


Figure 1-2. Two exceptional scenarios exceeding the blackbody limit. (a) Schematic illustrating near-field heat transfer between two objects with a gap distance of less than $\lambda_{th}$, showcasing the exchange of thermal energy through evanescent mode or surface mode waves. (b) Schematic illustrating radiative heat transfer between two objects when one or more dimensions of the objects are smaller than $\lambda_{th}$.

In the case of thermal radiation, there are two exceptional scenarios where heat transfer exceeds a blackbody limit, and these techniques can be employed to regulate the radiative heat current. For instance, recent experiments reveal that when planar surfaces are in close proximity—*i.e.*, when the gap size is significantly smaller than the thermal wavelength ($\lambda_{Th} \approx 10$ μm at room temperature)—the rates of radiative heat transfer can significantly surpass the blackbody limit[36,

[37]. This enhancement is attributed to contributions from evanescent and surface modes, involving the interaction of electromagnetic waves at the surfaces of the objects, and can be harnessed to enhance radiative heat transfer (see Figure 1-2a)[36]. Another example that exceeds the blackbody limit between two-body (or multi-body) systems is achieved by reducing the dimension of the device to less than a sub-wavelength (see Figure 1-2b)[38, 39]. In this design, radiative heat transfer rates exceeding the blackbody limit by more than two orders of magnitude can be attained due to enhanced emission and absorption of photons in the in-plane direction[38]. With this knowledge, we can devise a strategy to regulate the radiative heat current by (1) adjusting the gap between the two objects and (2) employing two or more devices with a thickness smaller than the thermal wavelength.

### *1.2.3 Calorimetry on Hydrogen ($H_2$) Absorption Reaction*

Hydrogen ($H_2$) is one of the potential candidates for a renewable energy source, including in fuel cell and hydrogen vehicle applications. To utilize and store $H_2$, researchers have extensively investigated various hydrogen storage systems employing different materials, including metal hydrides (MHs), complex hydrides, chemical hydrides, adsorbents, nanomaterials (such as nanotubes, nanofibers, nanospheres, and nanoparticles), clathrate hydrates, polymer nanocomposites, and metal-organic frameworks[40-45]. Among these, MHs offer several advantages in hydrogen storage systems due to their unique properties. MHs exhibit highly reversible hydrogen absorption/desorption properties, enabling them to release stored hydrogen as required and absorb it back when surplus hydrogen is available. The absorption/desorption process of $H_2$ on palladium (Pd) metal is given by[46, 47]:

$$\mathrm{Pd} + \frac{x}{2}\,\mathrm{H_2} \leftrightarrow \mathrm{PdH}_x + \Delta\mathrm{H} \qquad (1\text{-}3)$$

The hydrogen uptake on metal nanoparticles, often referred to as hydrogen adsorption, is generally an exothermic process[47] (see Figure 1-3a). This means that the process releases energy in the form of heat. The exothermic nature of hydrogen uptake on metal nanoparticles can be attributed to the formation of strong metal-hydrogen bonds during the adsorption process. When hydrogen molecules come into contact with the metal surface, they undergo a series of interactions leading to the breaking of the H-H bond in the hydrogen molecule and the formation of metal-hydrogen bonds. The sequence of $H_2$ absorption on metal occurs in three steps[43]: (1) $H_2$ is dissociated into H; (2) H diffuses into the metal lattice; and (3) H atoms occupy the interstitial metal sites (see Figure 1-3b). The energy released during the formation of these bonds contributes to the overall exothermicity of the process. This procedure plays a vital role in diverse applications, including the storage of hydrogen in materials for fuel cells or other sectors within the hydrogen-based energy industry.

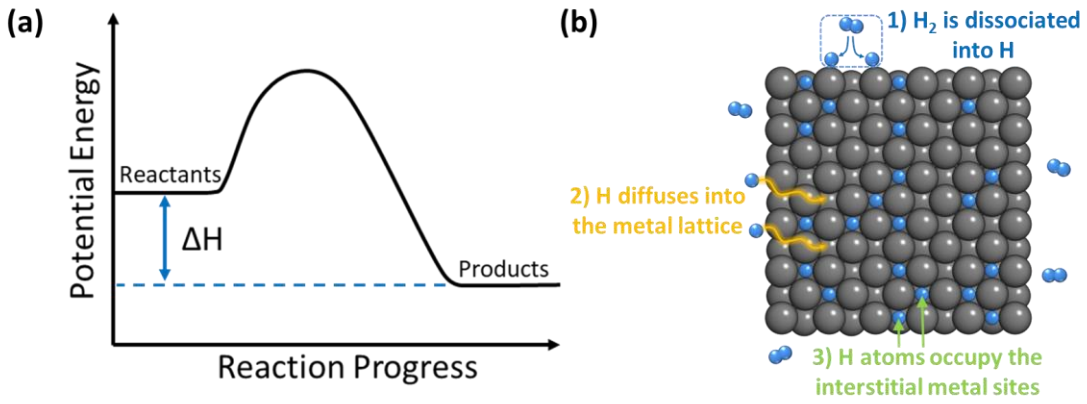


Figure 1-3. Explanation of reaction mechanism and energy diagram. (a) Potential energy diagram illustrating the exothermic hydrogen uptake process on metal nanoparticles. This exothermicity is attributed to the potential energy change associated with the formation of metal-hydrogen bonds during the $H_2$ adsorption process. (b) Graphical representation detailing the three-step $H_2$ absorption processes during the hydrogenation reaction on metal, as explained in the diagram.

### 1.3 Structure of This Dissertation

In Chapter 1, I provide a summary of thermal science and calorimetry relevant to my work. This background material provides the information necessary to understand the work described in this dissertation and helps clarify the significance of my research.

In Chapter 2, I present a nanoscale radiative thermal transistor comprising source, drain, and gate devices. Using microfabricated devices, I illustrate the control of heat currents in a three-body system consisting of source, drain, and gate terminals. Specifically, I demonstrate the control of heat current between a source and a drain by adjusting the temperature of a gate terminal coated with vanadium oxide ($VO_x$), which undergoes a thermally-driven metal-insulator transition, altering its dielectric properties. Additionally, I describe the time-response of the transistor and show that the switching speed of the device is a few hundred times faster than any previously reported thermal transistor. Finally, I discuss the mechanisms underlying the operation of the thermal transistor.

In Chapter 3, I investigate the limits to near-field radiative heat transfer (RHT). I describe experiments where the near-field radiative heat transfer enhancements of $MgF_2$ thin films were studied. Specifically, I demonstrate that nanofilms can enhance thermal radiation to be up to 800 times larger than that of the blackbody limit, proving their effectiveness comparable to bulk materials when nanoscale gaps have dimensions smaller than the film thickness. The experimental methods and findings outlined in this chapter lay the foundation for a systematic exploration of innovative thin films for near-field thermal and energy systems.

In Chapter 4, I introduce a calorimetric device designed for measuring the enthalpy of reactions involving gas-phase reactants with metal nanomaterials. This apparatus can quantify the overall thermal energy output when the Pd nanomaterial sample reacts with gas-phase reactants

(*e.g.*, $H_2$). To validate the performance of the instrument, a series of experiments were conducted, specifically examining $H_2$ absorption on Pd nanoparticles under varying pressures and temperatures. I explain the generated heat energy when Pd nanoparticles react with $H_2$ under different temperature and pressure conditions. The outcomes of these experiments align well with previous studies, confirming the capability of conducting high-resolution calorimetry on nanomaterials.

Finally, in Chapter 5, I summarize my work, discuss future work, and outline strategies to emphasize the significance of my research and its potential impact on society.

## Chapter 2 A Nanoscale Photonic Thermal Transistor for Sub-Second Heat Flow Switching

### 2.1 Abstract

Control of heat flow is critical for thermal logic devices and thermal management and has been explored theoretically[27, 48-50]. However, experimental progress on active control of heat flow has been limited. Here, we describe a novel nanoscale radiative thermal transistor that consisting of a hot source and a cold drain (both are ~250 nm-thick silicon nitride membranes), which are analogous to the source and drain electrodes of a transistor. The source and drain are in close proximity to a vanadium oxide ($VO_x$)-based planar gate electrode, whose dielectric properties can be adjusted by changing its temperature. We demonstrate that when the gate is located close (< ~1 μm) to the source-drain device and undergoes a metal-insulator transition, the radiative heat transfer between the source and drain can be changed by a factor of three. More importantly, in contrast to past thermal transistors, our nanomembrane-based thermal transistor features a much faster switching time (~500 ms as opposed to minutes) due to the small thermal mass of our nanoscale devices. Our experiments are supported by detailed calculations that highlight the mechanism of thermal modulation. We anticipate that the advances reported here will open new opportunities for designing thermal circuits or thermal logic devices for advanced thermal management.

### 2.2 Introduction

Thermal radiation plays an important role in heat-to-electricity conversion[5, 51, 52], near-field heat transfer[37, 53-55], and photonic cooling[56, 57]. Further, theoretical work[11, 12, 49, 58-60] has also

explored how radiative thermal transistors can be created. Analogous to electrical transistors, which are three-terminal transconductance devices where the current flow between the source and drain is regulated by a gate voltage[61, 62], current thermal transistors are based on three-terminal thermal designs where the temperature of a gate electrode controls the heat flow between two other terminals (source and drain), enabling heat flow switching. While some recent experimental studies[14, 15, 63, 64] have explored the creation of thermal transistors based on heat conduction and radiation, so far no near-field photonic thermal transistors—i.e., devices that control the flow of photons based on temperature or thermal changes—have been experimentally explored. Furthermore, these past demonstrations feature relatively slow switching times due to the large thermal mass of the employed devices and the challenges in rapidly modulating device material properties. The experimental demonstration of fast thermal transistors has also been hampered by the lack of the required experimental apparatus for precise thermal measurements and the challenges associated with the fabrication of appropriate micro- and nanoscale devices. Given the substantial potential of photonic thermal transistors for thermal energy utilization and modulation, along with its applicability in thermal logic circuits and computing, the necessity for an in-depth inquiry into this technology is crucial[14, 49, 50, 63].

In this work, we experimentally demonstrate a nanoscale radiative thermal transistor—a three terminal system consisting of source, drain, and gate devices (see Figures 2-1a, b). We show that the heat current between the source and the drain ($\dot{Q}_{S\text{-}D}$) can be controlled by changing the temperature of the gate, which is located below the source-drain device at a gap size $d$ (see Figure 2-1c), and is coated with a phase change material (vanadium oxide, $VO_x$) whose dielectric properties are strongly dependent on temperature[65, 66]. We note that $VO_x$ was selected as the gate material because it undergoes a metal-insulator transition at a relatively low temperature (~340 K)

compared to other phase-transition materials (e.g., $Ti_3O_5$, $LaCoO_3$, $Ti_2O_3$, $NbO_2$), whose transition temperatures range from 448 to 1,081 K[67]. The relatively low transition temperature makes it more suitable for practical applications operating in ambient conditions. Using these microfabricated devices, we show that the heat transfer between the source and the drain (see Figure 2-1a and Figure 2-5) can be modulated by up to a factor of three when the gap size between the source-drain device and the gate is less than ~1 μm and the gate undergoes a thermally-driven metal-insulator transition. Importantly, we demonstrate that our radiative thermal transistor achieves a switching time of less than a second (~500 ms), which is ~200 times faster than the fastest reported thermal transistor demonstrated to date (1.7 min)[15] and even faster than the switching times in older works, which ranged from a few minutes to an hour[14, 15, 63]. This sub-second scale fast-switching thermal transistor offers significant potential to explore new avenues in thermal-based computing systems, signal processing, and data transmission[50, 68, 69].

## 2.3 Experimental Procedure and Methods

### *Measurement of the source and the drain temperature*

The source-drain device is oriented in parallel with respect to the gate device in a high vacuum chamber (pressure < $10^{-6}$ Torr) using a custom-built nanopositioner[70]. During the measurements, the drain is nominally at room temperature ($T_{Amb}$ ~298 K), while the source temperature is modulated by supplying a fixed amplitude $I_{AC,f}$ = 12 μA sinusoidal current at a frequency of 1 Hz to the platinum heater line integrated into the suspended source membrane. The applied current isothermally heats up the source by ~4.8 K at a frequency of 2 Hz. The frequency of 1 Hz was selected as this frequency was sufficiently low to achieve a full thermal response, as seen in Figure 2-3d where the normalized temperature response is shown as a function of frequency. The amplitude of the temperature oscillation of the source ($\Delta T_{S,2f}$) at 2 Hz was estimated

by monitoring the voltage oscillation at 3 Hz ($\Delta V_{S,3f}$) across the Pt heater line with an SR830 lock-in amplifier. The temperature fluctuation of the source ($\Delta T_{S,2f}$) at 2 Hz was determined from the measured voltage ($\Delta V_{S,3f}$) following the equation: $\Delta T_{S,2f} = 2\Delta V_{S,3f}/I_{AC,f}R\alpha$, where $R$ is the electrical resistance of the Pt heater (~16.8 kΩ) and $\alpha$ is the TCR of the Pt heater ($1.75\times10^{-3}$ $K^{-1}$). More details of the electrical response, TCR measurement, and beam conductance measurement of the source are provided in Figure 2-9.

The heat flux from the source to the drain results in temperature oscillations ($\Delta T_{D,\,2f}$) of the drain at 2 Hz. In order to measure $\Delta T_{D,\,2f}$, a direct current $I_{DC}$ = 10 μA was applied across the Pt thermometer that is integrated into the drain device. Voltage oscillations ($\Delta V_{D,2f}$) at a frequency of 2 Hz were measured with an SR830 lock-in amplifier. Finally, $\Delta T_{D,2f}$ was determined from the equation $\Delta T_{D,2f} = \Delta V_{D,2f}/I_{DC}R\alpha$, where R and α are the electrical resistance and the TCR, respectively, for the drain Pt thermometer.

***Measurement of gate temperature***

To determine the temperature of the gate, we first measured the temperature coefficient of resistance (TCR) of the gate device under vacuum condition in a cryostat. The TCR was determined by observing the change in resistance under a current ($I_{AC}$ = 10 μA, f = 101 Hz) to ensure negligible self-heating while varying the temperature using a cryostat (Janis ST-100). We then proceeded to measure the resistance of the gate device while applying a bipolar voltage ranging from 0 V to ±4.0 V. By combining these measurements, we were able to estimate the temperature of the gate device at different power values, which in turn provided us with the beam conductance at each temperature. The temperature of the gate was measured at various bipolar voltages: 25 ℃ at 0 V, 33 ℃ at ±1.0 V, 54 ℃ at ±2.0 V, 68 ℃ at ±2.5 V, 83 ℃ at ±3.0 V, 100 ℃

at ±3.5 V, and 117 ℃ at ±4.0 V, respectively, with a temperature uncertainty of < ±1 K for each measurement. A more detailed method for measuring the gate temperature is explained in Figure 2-10.

***Derivation of radiative conductance and details of the conductance measurement***

To calculate the radiative conductance ($G_{S-D}$) between the source and the drain, a lumped thermal model was used. In this model, $G_{Th}$ is the total thermal conductance of the source and drain devices and is dominated by the conduction through the beams but has some contributions from a radiative exchange with the gate and the ambient. The characteristics of the source and drain devices are nearly identical since they were fabricated using the same procedure; hence, $G_{Th}$ is almost equal for both devices (Figure 2-9). It should be noted that $G_{Th}$ mostly comprises thermal conduction through the beams (~250 nW/K as shown in Figure 2-9), with a minor influence from near-field coupling between the source and gate. As the gap gets smaller, the near-field contribution can reach magnitudes of about 10 - 30 nW/K, depending on the gate temperature, which means that the radiative exchange between each membrane and the gate depends on the gap size. Thus, the value of $G_{Th}$ for each gap $d$ can be calculated using the equation $G_{Th} = P_{Joule}/\Delta T_S$, where $P_{Joule}$ represents the power dissipated in the Pt heater ($P_{Joule}=I_{AC}^2 R/2$), $R$ is the resistance of serpentine platinum, $\Delta T_S$ indicates the temperature change of the source ($\Delta T_S=2\Delta V_S/I_{AC}R\alpha$), and $I_{AC}$ is an alternating current (we chose $I_{AC}$ = 12 μA at $f$ = 1 Hz). Based on the lumped thermal model illustrated in Figure 2-2a, the radiative heat flow to the drain can be defined as $Q_{S-D} = G_{Th}\times\Delta T_D$. Accordingly, the radiative conductance between the source and drain device is given by $G_{S-D} = Q_{S-D}/(\Delta T_S - \Delta T_D)$, or equivalently $G_{S-D}=(G_{Th})\times[(\Delta T_S/\Delta T_D) -1]^{-1}$.

***Thermal frequency response of the source and gate devices***

To analyze the thermal frequency response of the source devices, a sinusoidal current with a fixed amplitude of $I_f$ = 6 μA was passed through the integrated platinum resistance thermometer (PRT) to induce Joule heating. This resulted in a temperature increase of approximately 1.2 K at a frequency of 2*f*. The frequency of the supplied current was varied within a wide range, from 0.1 Hz to 100 Hz, causing corresponding heat $Q_{2f} = I_{AC2} R/2$ across the integrated Pt heater at 2*f*. This heat dissipation led to a temperature fluctuation ($\Delta T_{2f}$) in the source, which was determined by measuring the 3f component of the voltage ($\Delta V_{3f}$) across the PRT using a lock-in amplifier. The temperature fluctuation can be calculated using the following equation:

$$\Delta T_{2f} = \frac{2\Delta V_{3f}}{I_f R \alpha} \qquad (2\text{-}1)$$

where $R$ and $\alpha$ denote the resistance and TCR of the device, respectively. Figure 2-3d illustrates the normalized temperature rises of the source device. The normalization point was selected at the frequency where the maximum temperature rise was observed. A complete thermal response is achieved at 2*f* below approximately 2.6 Hz, beyond which the signal begins to roll-off. The measured cutoff frequency of the source device was found to be 6.89 Hz.

To measure the thermal frequency response of the gate device, the same method was used, except for the amplitude of the current (see Figure 2-3e). A sinusoidal current with a fixed amplitude of $I_f$ = 1 mA was applied through the Si serpentine, resulting in Joule heating of the gate device at a frequency of 2*f* ($\Delta T$ ~1.5 K). Compared to the thermal frequency response measurement of the source device, a relatively large current was applied to the gate. This is because the beam thermal conductance of the gate (~ 0.4 mW/K at room temperature) is much larger compared to the source device (~ 250 nW/K), thus more current is required to raise the gate device. The frequency of the supplied current was varied across a wide range, from 0.1 Hz to 100 Hz, causing

corresponding heat dissipation $Q_{2f} = I_{AC}^2 R/2$ across the Si heater at $2f$. For the gate, a full thermal response was achieved at frequencies below ~2 Hz, beyond which the signal begins to roll-off. The measured cut-off frequency of the gate device was 5.33 Hz.

***Transient time response measurement***

To experimentally determine the thermal response time of the device, we modulated the gate temperature using a square-wave approach. The temperature was biased from 330 K to 354 K with a period of 20 seconds with a 50 % duty cycle. The square wave rise and fall time was rolled off to ~300 ms, in order to reduce any capacitive voltage spikes in the measurement. The source was heated using an AC current with an amplitude of 12 μA and a heating frequency of 6 Hz to enable a fast thermal response in the experimental setup. We collected the temperature data of the source and drain from this measurement at a sampling rate of 50 Hz for a total duration of 12 hours using an integration time of 100 ms on the lock-in amplifier (SR830). Finally, to improve the signal-to-noise ratio, we averaged the temperature data over approximately 2160 periods. Using a lumped capacitance analysis, we estimated the thermal time constant (switching time) to be the interval when the radiative conductance has changed by $1 - e^{-1}$ (~63.2 %) of its total change. We see from our measurements that we achieved an off-on switching time ($\tau_{\text{Off-On}}$) of ~ 470 ms and an on-off switching time ($\tau_{\text{On-Off}}$) of ~ 500 ms. This shows that this thermal transistor does indeed have a very symmetric, sub-second switching characteristic.

***Computing the radiative conductance and Poynting fluxes in the many-body system with SCUFF-EM***

The source and drain membranes were modelled as 80 µm long, 60 µm wide, and 250 nm thick silicon nitride (SiN) membranes. The gate was modelled as a 180 µm long, 60 µm wide, and 10 µm thick doped silicon substrate with 150 nm $VO_x$ coated on all sides. These dimensions were chosen to keep the computations tractable without altering the physics of the problem. We chose to model the gate with $VO_x$ coating on all sides as we were not able to get a converged solution with $VO_x$ only present on the top layer, which was most likely caused by the computational challenges of three-material junctions (vacuum, doped Si, and $VO_x$). As shown in Figure 2-8, the presence of $VO_x$ on all the other sides except the top surface plays little to no role in the heat transfer from the source to the drain, mainly because the 10 µm-thick doped Si layer becomes opaque to all thermal radiation.

For the Poynting flux calculations, we changed the width of all the membranes, i.e., the source, drain, and gate, from 60 µm to 30 µm. These calculations are computationally demanding and thus a full-scale geometry could not be modelled. Thermally-induced surface current sources were set up in the source at 300 K and the spatial distribution of the Poynting flux was evaluated at 0.1 eV and 0.1286 eV for gap sizes of 25 µm and 3 µm, respectively.

### 2.4 Results and Analysis

In this work, we employed two independently microfabricated devices. The first device (see Figure 2-1a), referred to as the source-drain device in this work, consists of two SiN membranes that form the source (i.e., the thermal emitter) and drain (i.e., the thermal receiver) of our thermal transistor and are coplanar. These membranes are 250 nm thick and contain a serpentine platinum resistor. This serpentine line functions as a heater in the source and as a thermometer in the drain (Figure 2-1a). The source and the drain are separated by a fixed distance of 20 µm and are suspended by long beams affixed to a silicon handler chip. The gap

size of 20 μm was intentionally chosen to ensure that the near-field radiative heat transfer effect, which becomes considerable when the gap size is smaller than the thermal wavelength $\lambda_{th}$ (~10 μm at 300 K), is negligible[38, 71]. We note that the source and drain membranes feature internal tensile stresses that ensure that they have excellent planarity and are co-planar, as confirmed by laser scanning confocal microscopy (see Figures 2-1d, e). Shields to prevent any heat exchange between beams are also visible in the confocal microscopy image. Further details about the fabrication of the source-drain device are provided in Figure 2-5.

The bottom device used in this work, called the gate (see Figure 2-1b), consists of the suspended portion of a Si device that is supported by two beams. The suspended region features a doped silicon resistor heater/thermometer and a 15 μm-tall silicon mesa, which is coated with a 150 nm-thick $VO_x$ film. To achieve the phase transition of $VO_x$ ($VO_x$ films undergo a metal-insulator transition at ~68 °C[72]), we applied a bipolar voltage to the integrated silicon resistor to heat the gate. The bipolar voltage helped maintain the voltage of the gate region close to 0 V and minimized the electrostatic interaction between the top and bottom devices. As described in the Methods section, the silicon resistor is used to heat up the temperature of the gate region, which enabled us to systematically vary the temperature of the gate and thus control the phase (metal or insulator) of the $VO_x$ film integrated into the gate. More details about the fabrication and characterization of the gate device can be found in Figure 2-6, Figure 2-7, and Figure 2-10.

In order to demonstrate modulation of heat flows via thermal inputs to the gate, we first placed the two devices (both top and bottom devices) in a custom-built nanopositioner[70] that allows parallelization of the devices as well as control of the gap size ($d$) between them in a high vacuum environment (~1 μTorr). In Figure 2-1c, we schematically depict the relative orientation of the devices. After the system had reached thermal equilibrium with the vacuum chamber (i.e., when

the temperature drift of the devices was <1 mK/hr), we first adjusted the gap size ($d$) to 25 μm. Next, we applied an alternating electrical current (AC) of suitably chosen amplitude at a frequency ($f$) of 1 Hz to the PR heater of the source to sinusoidally modulate the temperature of the source ($\Delta T_{S,2f}$) at 2 Hz. The radiative heat current from the source to the drain produced temperature oscillations of the drain ($\Delta T_{D,2f}$) at 2 Hz, which were quantified by passing a fixed sensing DC current ($I_{DC}$) of 10 μA through the drain's PR thermometer to measure the voltage fluctuations at 2 Hz using a lock-in amplifier (see Methods). We note that there are negligible thermal gradients within the suspended membranes (discussed in more detail in Figure 2-11d), which is key to accurately measuring the heat fluxes. The measured $\Delta T_{D,2f}$ as a function of $\Delta T_{S,2f}$ is shown in Figure 2-1g at a large separation distance ($d$ = 25 μm) with a gate temperature ($T_G$) of 25 °C and is found to be linearly related. These data enabled the calculation of the thermal conductance ($G_{S-D}$) between the source and drain devices via $G_{S-D} = (G_{Th})\times[(\Delta T_S/\Delta T_D) - 1]^{-1}$, where $G_{Th}$ is the total thermal conductance of each suspended device (see Figure 2-2a), which encompasses conduction through the support beams and radiative exchange with the gate (see Methods for details on how $G_{Th}$ is determined at each gap size).

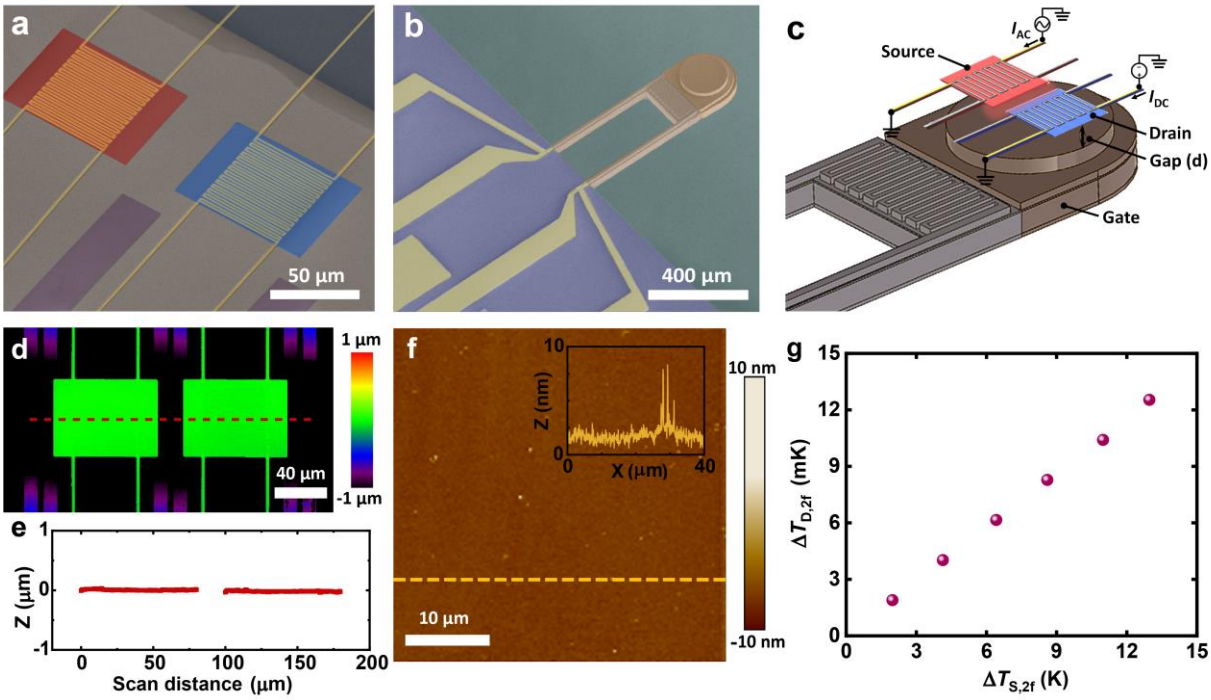


Figure 2-1. Experimental and computationally predicted conductance results. (a) False-colored scanning electron microscope (SEM) image of the nanofabricated source and drain device, showing a coplanar silicon nitride (SiN) membrane device with integrated Pt serpentine. (b) False-colored SEM image of the fabricated gate device featuring an incorporated Si heater and a layer of $VO_x$. (c) Schematic of the nanofabricated three-body system. (d) Confocal microscope scan of the source-drain device. (e) Profile along the dashed scan line in Figure 2-1d, demonstrating excellent planarity of the device. (f) Atomic force microscopy (AFM) image of the gate coated with $VO_x$. The inset in Figure 2-1f indicates a scanned height profile along the dashed line. (g) The amplitude of the temperature oscillation of the drain ($\Delta T_{D,2f}$) was studied as a function of the amplitude of temperature oscillations of the source ($\Delta T_{S,2f}$). The source temperature was modulated at a frequency of 2 Hz, with the gate positioned far away ($d$ ~25 µm) from the source-drain device, while maintaining a temperature of 25 °C.

Next, we repeated this process for a range of gap sizes (from 25 µm to contact) and gate temperatures (25 °C to 117 °C) at a fixed value of $\Delta T_S$ (~4.8 K). We note that in performing these experiments, the gap distance between the devices was controlled using a combination of a piezoelectric actuator and a stepper motor mounted on a translational stage. In Figure 2-2b, we illustrate the approach process with a time trace where the gap size between the gate and the source-drain devices was systematically reduced in steps of ~0.35 µm from ~8 µm to contact (a shorter range of gap sizes is shown for clarity). The values of $\Delta T_S$ and $\Delta T_D$, at a $T_G$ of 25 °C, were simultaneously recorded for each gap separation, $d$. The middle and bottom panels of Figure 2-2b

show the simultaneously measured temperature changes in the source ($\Delta T_S$) and drain ($\Delta T_D$) devices, respectively. The point of physical contact between the gate and the source-drain electrodes was indicated by a large simultaneous change in the temperature of both the source and drain.

To calculate $G_{S-D}$ (see above), we use the measured values of $\Delta T_S$ and $\Delta T_D$ for various gap sizes between the source-drain device and the gate and for various temperatures of the gate electrode. The results for the full range of gap sizes are shown in Figure 2-2c. The data shown in dark blue in Figure 2-2c correspond to the situation where the gate is at room temperature (25 ℃), i.e., when the $VO_x$ film is in the insulating phase. For this case, the measured conductance was ~240 pW/K for a large gap separation (~25 μm) between the source-drain device and the gate. As the gap distance was reduced to ~16.5 μm, we observed a modest increase in the conductance to a maximum value ($G_{S-D,max}$) of 257.2 pW/K. Interestingly, as reported in a recent study[38], the measured conductance is much larger than that expected from the blackbody limit (~4 pW/K) calculated from far-field radiative heat theory (FF-RHT), see Supplementary Materials for more details of this estimate of the blackbody limit. As the gap size was decreased further to ~10 μm, there was a gradual decline in $G_{S-D}$, followed by a more rapid decrease for even smaller gaps. This more rapid decrease in $G_{S-D}$ below ~10 μm occurs due to the strong influence and interaction of the gate on the guided modes supported by the source and drain membranes[73], which is discussed in more detail below. Finally, we note that the minimum value of the source-drain thermal conductance ($G_{S-D,min}$), ~13 pW/K, was reached just before contact between the gate and the source-drain device.

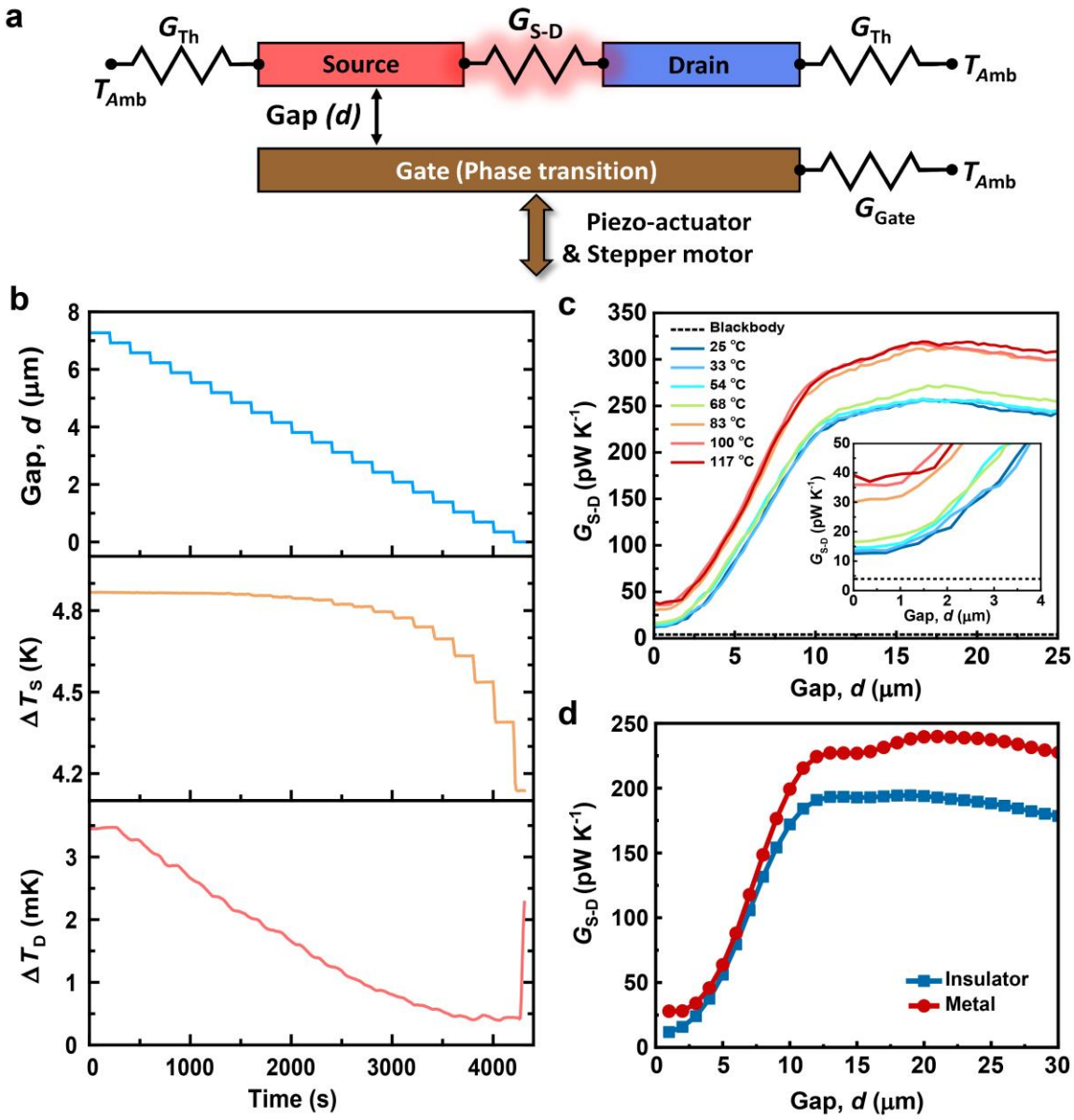


Figure 2-2. Measured and computationally predicted conductance between the source and the drain device. (a) Thermal resistance network corresponding to the thermal transistor. Both the suspended source and drain membranes have a total thermal conductance of $G_{Th}$, while the gate has a beam conductance of $G_{Gate}$. The height of the gate is adjusted using a piezoelectric actuator and a stepper motor, separated from the source-drain device by a gap distance $d$. Devices are placed in an environment at ambient temperature, $T_{amb}$. (b) Time series of a representative measurement as the gate approaches the source-drain device at 25 ℃. The top graph shows the measured gap distance between the source-drain device and the gate until contact. The corresponding time plots show the amplitude of temperature oscillations for the source (middle panel) and the drain (bottom panel) over time. (c) Experimental data for the radiative conductance $G_{S-D}$ as a function of the gap, $d$. The effect of the phase transition can be clearly seen when the temperature of the gate changes from 25 ℃ to 117 ℃. A noticeable change in the conductance was observed when the gate temperature crossed the phase transition threshold (from 68 ℃ to 83 ℃). (d) SCUFF-EM calculations of the radiative conductance between the source and drain electrodes when the gate is in the insulator and metallic phases. It can be clearly seen that there is a good qualitative agreement with the experimental data in panel c.

Similar behavior in the gap dependence of $G_{S\text{-}D}$ was found for a range of gate temperatures ($T_G$ = 33 ℃ and 54 ℃, respectively), as shown in Figure 2-2c. As the gate temperature approached the phase transition temperature (~68 ℃), a noticeable change in thermal conductance was observed, confirming that the $VO_x$ began to undergo a transition from an insulating state to a metallic state. Once the gate temperature was increased to 83 ℃ or higher, where $VO_x$ is in its metallic state, the conductance increased to a higher value at every gap size (see Figure 2-2c). Specifically, at these higher gate temperatures, it was observed that when $d$ is 25 μm, $G_{S\text{–}D}$ is ~310 pW/K, which is larger than the conductance observed when the gate was in the insulating phase. This is likely because the gate has a higher reflectivity in the metallic phase, resulting in an enhancement of the number of photons received by the drain electrode[39]. At these high temperatures, as $d$ was further reduced, $G_{S\text{-}D}$ decreased continuously, reaching a minimum value of ~39 pW/K right before contact between the gate and the source-drain device.

The above-described experiments reveal that the heat current between the source and drain can be controlled by either changing the phase of the $VO_x$ film integrated into the gate or by changing the gap distance $d$ between the gate and the source-drain device. Past work[11, 63, 74, 75] has referred to devices that allow control of heat flow between two objects via a third object (including the introduction of ions as the electrolyte) as a thermal transistor. Following this convention, the device discussed in this work also represents a thermal transistor in which the heat current between the source and the drain is controlled by a third body (gate). In order to make this explicit, in Figure 2-3a we symbolically represent our device as a thermal transistor where the gate plays a role similar to the gate electrode of an electrical transistor and controls the flow of heat between the source and the drain, which are analogous to the source and drain electrodes of an electrical transistor.

In order to directly illustrate this switching action, we apply a bipolar voltage (ranging from 0 V to ± 4.0 V) to the resistor integrated into the gate that enables varying the temperature of the gate from 25 ℃ to 117 ℃. At any given gap size, the "Off" state of the thermal transistor corresponds to the situation where the $VO_x$ gate is in the insulating phase, resulting in a lower heat current between the source and the drain, while the "On" state corresponds to the case where the gate is in the metallic phase, which results in a higher heat current between the source and the drain. In Figure 2-3b, we show the On/Off ratio ($R = G_{S-D,on}/G_{S-D,off}$) as a function of $d$. We found that for $d$ = 25 μm the On/Off ratio was ~1.31. As $d$ was reduced, a noticeable increase in the On/Off ratio was observed with the ratio reaching 3.02 right before contact.

In order to directly demonstrate heat current switching, we simultaneously recorded the radiative conductance while rapidly increasing and decreasing the gate temperature. Specifically, we performed an experiment when the temperature difference between the source and the drain was ~4.4 K, with a fixed gap size of $d$ ~1 μm or less (just before contact). Modulation of the gate device temperature was accomplished by applying a bipolar square wave voltage (±4 V for 117 ℃, 0 V for 25 ℃) with a period of 200 seconds (Figure 2-3c, bottom panel). The measured conductance between the source and the drain (Figure 2-3c, top panel) is consistent with the results from Figure 2-2c. The radiative conductance changes by a factor of three, i.e., from ~13 pW/K (insulator phase) to ~39 pW/K (metallic phase). At this smallest gap, we also performed experiments to systematically explore the effect of gate temperature on the heat current between the source and drain. Results from this experiment are shown in Figure 2-3d. As expected, when the gate temperature was below the phase transition temperature (around 68 ℃), the heat flow between the source and drain electrodes was low and remained relatively constant even as the gate temperature increased. However, once the phase transition temperature was surpassed, a sudden

jump in the heat transfer rate was observed. Additionally, we also performed experiments while cooling the gate (Figure 2-3d), which revealed hysteretic behavior in the heat flow that is consistent with the hysteresis of the phase transition properties of $VO_x$[76, 77].

The above experiments reveal that for our thermal transistor, the maximum *R* value is ~3, which is comparable to that demonstrated in past work. For example, Cho *et al.* reported an On/Off ratio of 1.5 with a switching time of 1.5 hours during room temperature operation[74]. A. Sood *et al.* demonstrated an On/Off ratio of approximately 10 with a switching time of 7 minutes under the same operating temperature[14]. Q. Yang *et al.* reported an On/Off ratio of 4 with a switching time of 3 minutes at an operating temperature of 280 °C[63]. L. Castelli *et al.* demonstrated the fastest switching speed in past published work, with a time constant of 1.7 minutes when the device was turned off, and a switching speed of 4.6 minutes when the device was turned on, and reported an On/Off ratio of 109[15]. While the *R* values reported by us are smaller than in some previous works, the switching speed of our devices is orders of magnitude faster as quantified below.

The switching speed of thermal transistors is primarily controlled by the thermal time constant of the source, drain, and gate electrodes of the transistor. To quantify the switching speed for our devices we performed frequency response measurements, where we measured the amplitude of temperature oscillations as a function of the frequency of heat input (see Methods for details). The measured frequency responses of the drain (nominally equivalent to the source) and the gate device are shown in Figure 2-3e. The drain device features a cutoff frequency ($f_c$) of 6.89 Hz, and the gate device has a cutoff frequency of 5.33 Hz, respectively. Therefore, the thermal time constant ($\tau = 1/2\pi f_c$) of the drain is ~23 ms, while that of the gate is ~30 ms. This analysis suggests that the switching time of the photonic thermal transistor is expected to be at least ~30 ms, which is limited by the slower thermal response of the device, gate device. To experimentally

determine the switching speed of our thermal transistor device, we performed an experiment (see Methods) with a significantly shorter lock-in time constant (100 ms). Data corresponding to this experiment is shown in Figure 2-3f and features a switching speed of ~500 ms, which is a much faster response time than that demonstrated to date in thermal transistors. However, this switching speed is still slower than that expected from the frequency response measurements described above and is limited by the lock-in time constant. Reducing the lock-in time constant further (less than 100 ms) was not feasible because of the limited signal-to-noise ratio of the measurements and capacitive voltage spikes generated by the square wave modulation technique. Details of the transient time response measurement procedure are explained in the Methods section.

In order to mechanistically understand the thermal switching phenomena due to the phase transition of $VO_x$, we performed fluctuational electrodynamics-based calculations using SCUFF-EM. We modelled the source-drain device as two coplanar SiN membranes, each measuring 80 μm in length, 60 μm in width, and 250 nm in thickness, with a separation of 20 μm (see Figure 2-8b). The dimensions of the source-drain device used in the theoretical calculation exactly match those employed in the experiment. The gate was modelled as a 10 μm thick, doped silicon membrane encapsulated with a 150 nm-thick $VO_x$ layer. The dimensions of the gate were chosen to be 180 μm length and 60 μm width (see methods for a discussion of the choice of these dimensions). In our calculations, the gap size ($d$) between the source-drain device and the gate is varied from 25 μm to close to contact (a gap size of 1 μm). The radiative conductance is calculated as a function of gap sizes, both when the $VO_x$ is in the insulator and in the metallic phase. The computed results (Figure 2-2d) exhibit a very similar gap size dependence to what was observed experimentally and reveal a lower thermal conductance ($G_{S\text{-}D}$) for both phases, although the absolute magnitude is consistently lower by ~30%. We attribute this discrepancy to the radiative

conductance between the support beams and the mismatch of the dielectric function of materials between models and microfabricated devices, which was also observed in our previous works[36, 38, 39, 78].

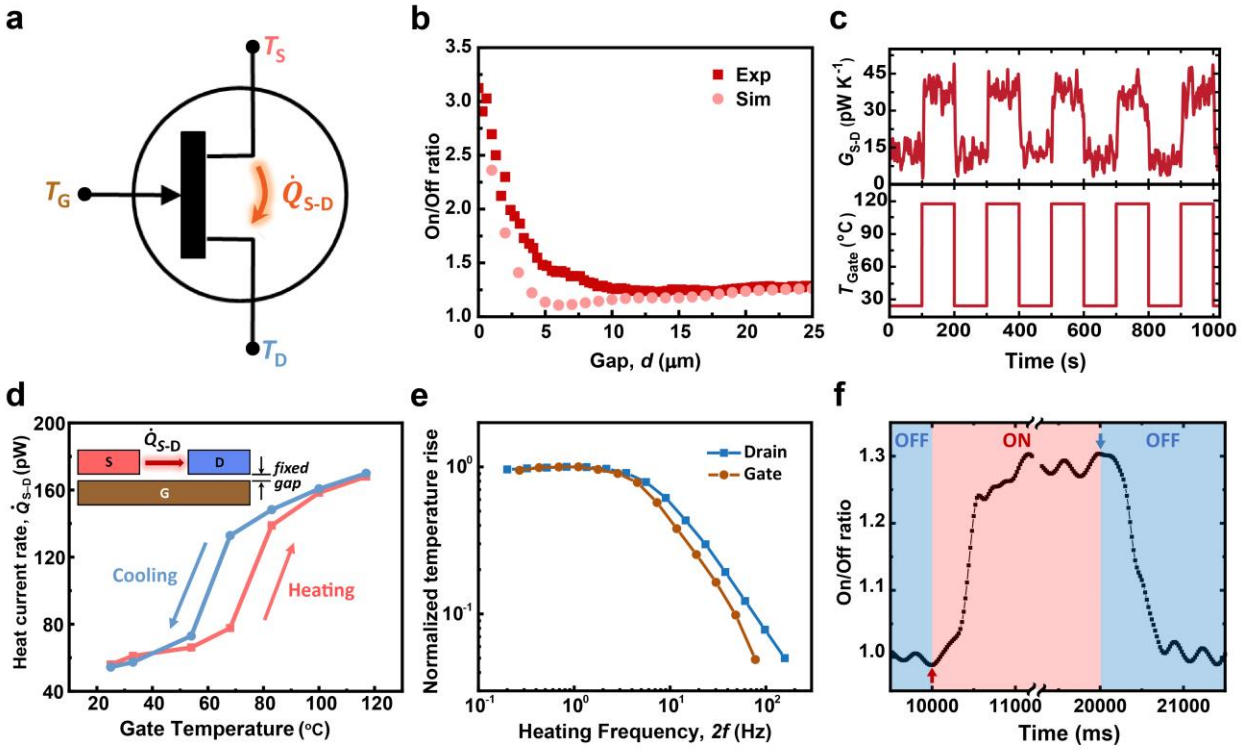


Figure 2-3. Characterization of thermal transistor performance. (a) A symbol representing the designed thermal transistor, illustrating control of the heat current between the source and drain electrodes via the gate temperature. (b) On/Off ratio of the thermal transistor as a function of the gap size, *d*. (c) The measured change in the source-drain conductance (top panel) when the temperature of the gate (bottom panel) periodically changes from 25 °C to 117 °C and back by applying a bipolar voltage from 0 V to ±4 V. In this experiment, the period of the gate temperature variation is 200 s, and the gate is positioned just before the contact (*d* of less than ~1 μm). (d) Heat current rate ($\dot{Q}_{S-D}$) between the source and the drain as a function of the gate temperature just before contact (*d* of less than ~1 μm). The temperature difference between the source and the drain is measured to be ~4.4 K before contact. (e) Measured thermal frequency response of the drain and gate devices. (f) Measured time response with a lock-in time constant of 100 ms. These data show a switching time ($\tau_{Off-On}$) of ~470 ms for the rise and $\tau_{On-Off}$ of ~500 ms for the decay response, respectively.

To gain insight into the physical mechanism underpinning the change in heat flux due to the phase transition of $VO_x$, we calculated the spectral conductance at various gap sizes for both the insulating and metallic phases (Figures 2-4a, b). It can be observed that, as the gap size is

reduced, there is a strong attenuation in the spectral conductance at all frequencies for both insulating and metallic phases, resulting in a reduction of heat transfer in both cases. However, the insulating phase does exhibit a more rapid attenuation as the gap size decreases when compared to the metallic phase.

In order to understand the effect of the gate on $G_{S-D}$, we computed the in-plane Poynting fluxes in the *x*-direction ($P_x$), which is the direction of heat flow from the source to the drain. The Poynting fluxes were calculated at frequencies where the difference in the value of spectral conductance between both phases is largest (i.e., 0.1 eV when $d$ = 25 μm; 0.1286 eV when $d$ = 3 μm), thus making the contrast between the heat flow of different phases more apparent (see arrows in Figures 2-4a, b). When the gate is far away (e.g., $d$ = 25 μm), the Poynting flux appears very similar for both the insulating and metallic phases, with a slight enhancement in the heat flux of the metallic phase due to the higher reflection on the metallic surface (Figures 2-4c, d). However, when $d$ = 3 μm, we observe a noticeable enhancement in the Poynting flux for the case where the gate is metallic, in comparison to the insulating phase (Figures 2-4e, f). This difference in radiative conductance at small gap sizes arises from the fact that, for a metallic layer, there is very poor radiative coupling between the source-drain device and the gate. This, in turn, prevents radiation modes from being absorbed in the bulk of the gate and leads to a relatively higher absorption cross-sectional area between the source and drain membranes.

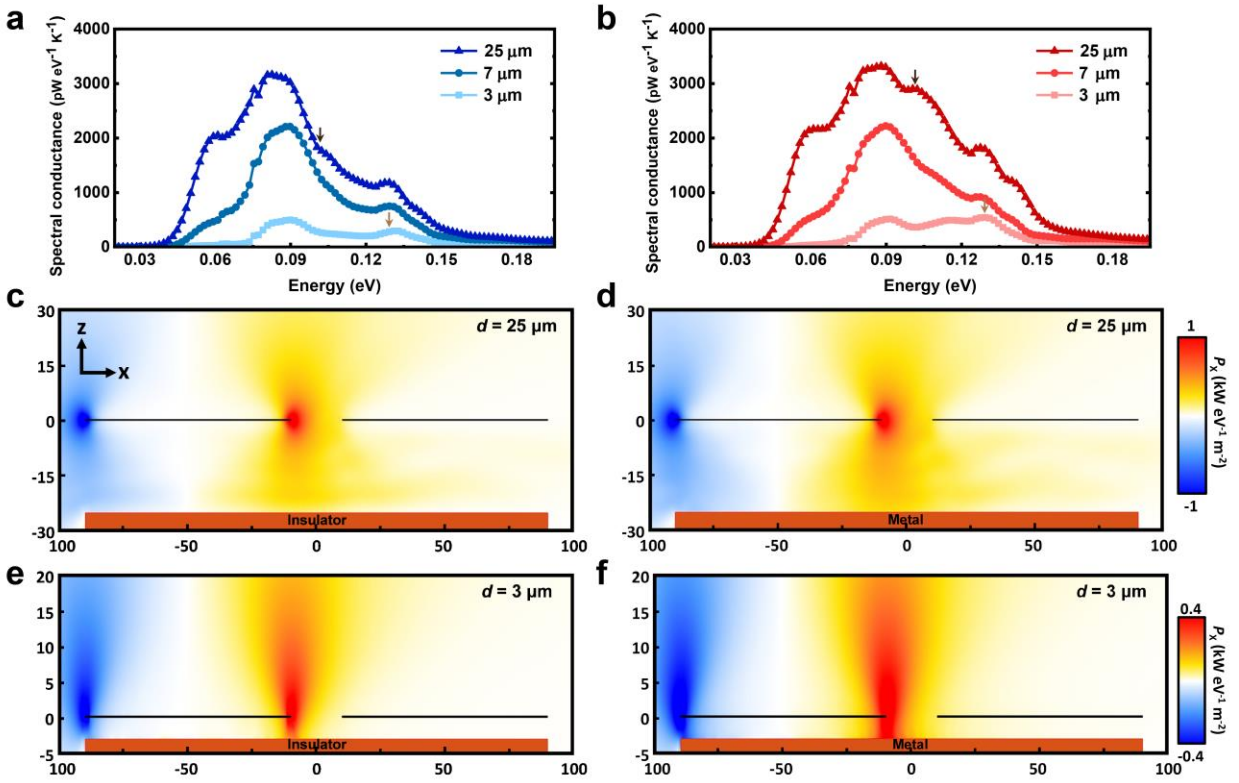


Figure 2-4. Analysis of spectral conductance and Poynting vector in the three-body system. The computed spectral conductance plots for the insulating (a) and metallic (b) phases are shown for a gate at various gap sizes: 25 μm, 7 μm, and 3 μm, respectively. The attenuating effect of the third body becomes clearly visible as it is brought closer to the membranes. The arrows in (a) and (b) indicate the position where Poynting vectors are calculated in Figures 2-4(c–f). Figures 2-4(c) and (d) display the Poynting vector plot on the midplane (a plane cutting through the middle of the system) at the frequency of 0.1 eV with a gap separation of 25 μm away from the source-drain device for the insulating phase gate and the metallic phase gate, respectively. Similarly, Figures 2-4(e) and (f) exhibit the Poynting vector at the frequency of 0.1286 eV with a gap separation of 3 μm away from the source-drain device for the insulating phase gate and the metallic phase gate, respectively. In Figures 2-4(c–f), the black lines indicate the 250 nm SiN layers (left: Source, right: Drain), while the brown block represents the gate coated with 150 nm $VO_x$. The frequency for the Poynting flux calculation is systematically chosen where the difference in spectral conductance between both phases is the largest at each gap.

## 2.5 Conclusion

To summarize, we present a novel nanoscale radiative thermal transistor capable of controlling the heat current between two nanometer-thick membranes. This transistor enables precise manipulation of heat flow via a gate, whose dielectric properties can be tuned by modifying the temperature. Specifically, we demonstrate that the radiative heat transfer between the source

and drain membranes can be modified by up to a factor of three when the gate undergoes a metal-insulator transition. More interestingly, our nanomembrane-based thermal transistor exhibits fast switching times (~500 ms), attributed to the small thermal mass of our devices, which is two orders of magnitude faster than the thermal transistors presented in a recent work[15]. Our experimental findings are complemented by a theory-based model calculation that elucidates the mechanism of thermal modulation. Taken together, these results highlight the potential for fast heat current modulation via nanoscale membranes. These findings have the potential to make a substantial impact on the fields of thermal management and computing, particularly in the areas of heat current control, thermal circuits and logic devices, and thermal energy conversion.

## 2.6 Supplementary Materials

### *Fabrication of the suspended source and drain devices*

The micro-fabrication processes for the source and drain devices are reported in detail elsewhere[39]. Briefly, the fabrication process from the cross-sectional view is illustrated in Figure 2-5. Starting with a 500 μm-thick, double-side polished silicon wafer (Step 1), LPCVD low-stress silicon nitride (SiN) films with a thickness of 250 nm were deposited on both sides of the wafer (Step 2). Then, using liftoff processes (Step 3), 30 nm-thick platinum (Pt) heater-thermometer lines, followed by 100 nm-thick gold (Au) contact pads, were patterned on the top side of the wafer. Next, the SiN layers on the frontside and backside of the wafer were lithographically etched using reactive ion etching (RIE) to form a suspended structure (Step 4). The source and drain membranes were released through a final etching process using KOH (Step 5). The shield used to prevent any heat exchange between beams is not included in this schematic.

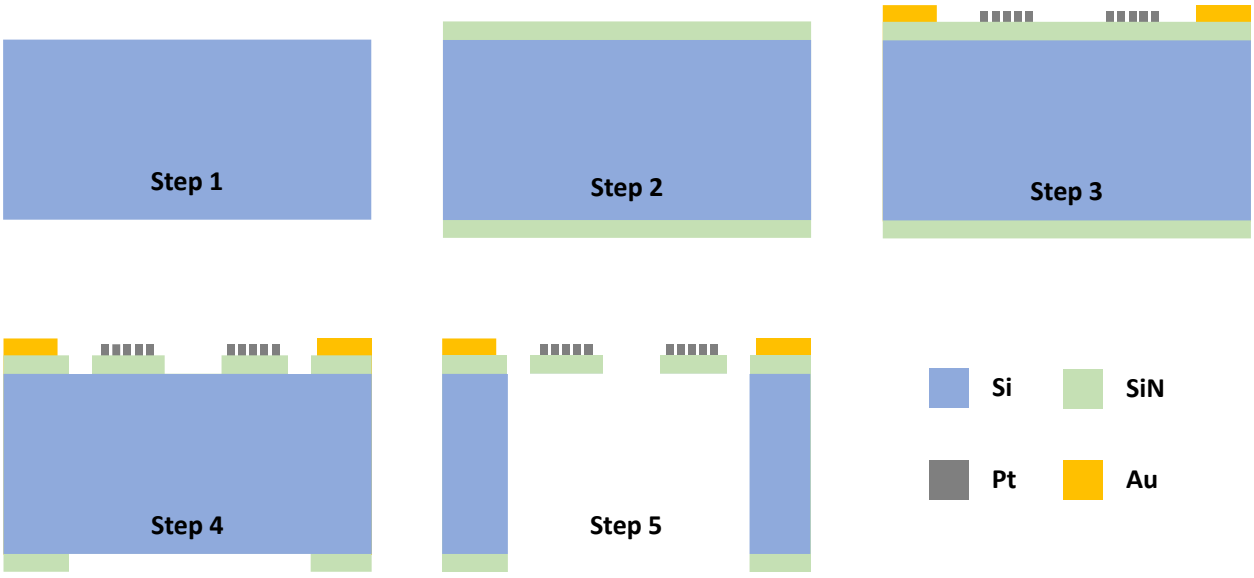


Figure 2-5. Fabrication process for the suspended source and drain devices.

***Fabrication of gate device***

The fabrication process for the gate device is illustrated in Figure 2-6. A p-doped double-bonded silicon-on-insulator SOI wafer (Ultrasil LLC) with a 20 ± 1 μm-thick top layer, 40 ± 1 μm-thick middle layer, 400 ± 5 μm-thick substrate, and two 1 μm-thick buried oxide layers (BOX) is chosen (Step 1). The specified resistivity of both the top and middle layers is < 0.02 Ω cm. BOX layers are used as etch stops to fabricate the suspended gate device. The top device layer is patterned and etched to form a 16 μm-tall mesa using a deep reactive ion etching (DRIE) process (Step 2). The ~4 μm-tall silicon serpentine structure is then patterned using standard lithographic techniques and etched using DRIE (Step 3). Next, a 200 nm-thick gold layer is deposited to form electrical contacts and patterns formed using a lift-off process (step 4). Note that Ti/Pt (10/30 nm) are deposited (not illustrated in step 4) underneath the Au for better contact. The device beams and the structure are patterned and etched from the top using the DRIE process (Step 5). The Si handle

layer, two BOX layers, and Si middle layer are etched away from the back side of the device to release the suspended beam structure using the DRIE processes (Step 6). Subsequently, a layer of $Al_2O_3$ with a thickness of 10 nm was deposited onto the gate device using atomic layer deposition, serving the purpose of creating an electrically insulating layer (Step 7). Finally, a 150 nm-thick $VO_x$ is deposited on the mesa as a phase transition material, followed by annealing at 350 ℃ for 5 min under an $N_2$ atmosphere (Step 8).

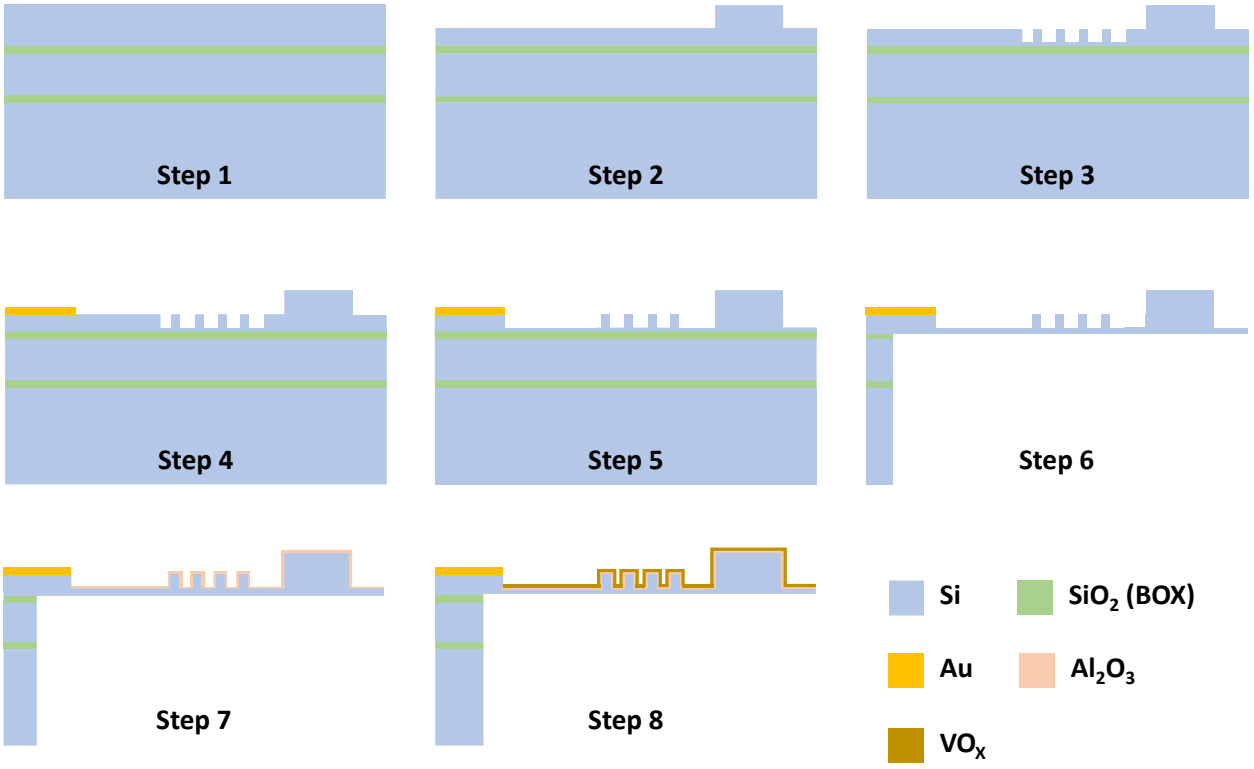


Figure 2-6. Fabrication process for the gate device.

***Deposition of vanadium oxide ($VO_x$) thin film***

In this study, we grew a $VO_x$ thin film on a gate device by physical vapor deposition (PVD) using a DC-pulsed magnetron sputtering process in an LAB18 sputtering system (Kurt J. Lesker Company) using a 99.9% pure vanadium target with a diameter of 3 inches and a thickness of

0.125 inches. The substrate temperature was maintained at room temperature. In the process, the DC power was set to 180 W, and both argon and oxygen were introduced into the chamber at flow rates of 48.5 sccm and 1.5 sccm, respectively. The sputtering rate of the $VO_x$ thin film was determined to be approximately 5 nm/min by measuring the thickness of the as-deposited film. Subsequently, the sputtered $VO_x$ thin film underwent annealing at 350 ℃ for 5 minutes under an $N_2$ ambient using the Jetfirst 150 RTP tool.

To evaluate the resistance of the $VO_x$ thin film, a 150 nm-thick film was deposited on a silicon substrate. The resistance of the $VO_x$ film was measured during the heating and cooling process, and the results are presented in Figure 2-7. The observed hysteresis occurring during the phase transition is attributed to the strain, doping, and lattice defects inside the deposited $VO_x$ thin film[76].

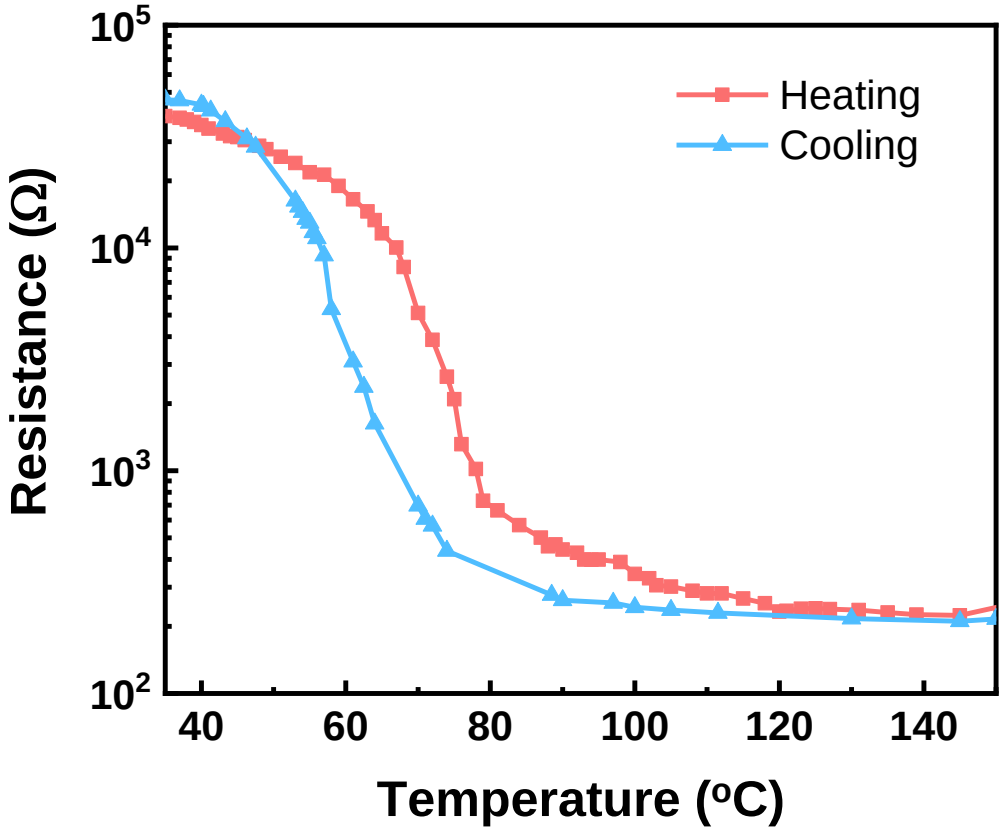


Figure 2-7. Resistance characteristics of a $VO_x$ film deposited on a bare Si as a function of the substrate temperature.

***Effect of Si thickness on gate device in the SCUFF-EM model***

To support the choice of a 10 µm-thick Si gate for the radiative conductance and Poynting flux calculations presented in Figures 2-2d and 2-4, we examined the effect of the gate thickness on our SCUFF-EM calculations. We began by creating models with three different gate thicknesses: 5 µm, 10 µm, and 15 µm, all made from doped Si, while maintaining the source and drain SiN membranes at 80 µm long, 60 µm wide, 250 nm thick, and separated by 20 µm. All three gates were coated with 150 nm of $VO_x$ on all sides. The three cases are schematically shown in Figures 2-8(a–c) below.

We then computed the radiative conductance between the source and drain membranes. The gap of the gate to the source and drain SiN membranes was calculated for gap sizes ($d$) ranging from $d$ = 1 μm to $d$ = 25 μm, with the $VO_x$ layer covering the whole surface of the Si gate. Figures 2-8d, and 2-8e display the results of the gap-dependent radiative conductance at three different gate thicknesses when the $VO_x$ layer is in the insulating and metallic phases, respectively. Results indicate that the radiative conductance is independent of the Si gate thickness, specifically within the range of 5 μm to 15 μm. This implies that the $VO_x$ layer at the bottom of the gate plays little to no role in the heat flow between the source and drain when the Si thickness of the gate is 5-15 μm. Consequently, choosing a 10 μm thick Si gate with $VO_x$ covered on all sides serves as a representative model for our experiments. Note that, in our experiments, only the top surface of the Si gate is covered by the $VO_x$ thin film. We have excluded the consideration of the $VO_x$ film on the sides in this argument, as we believe it plays a negligible role in the heat flow.

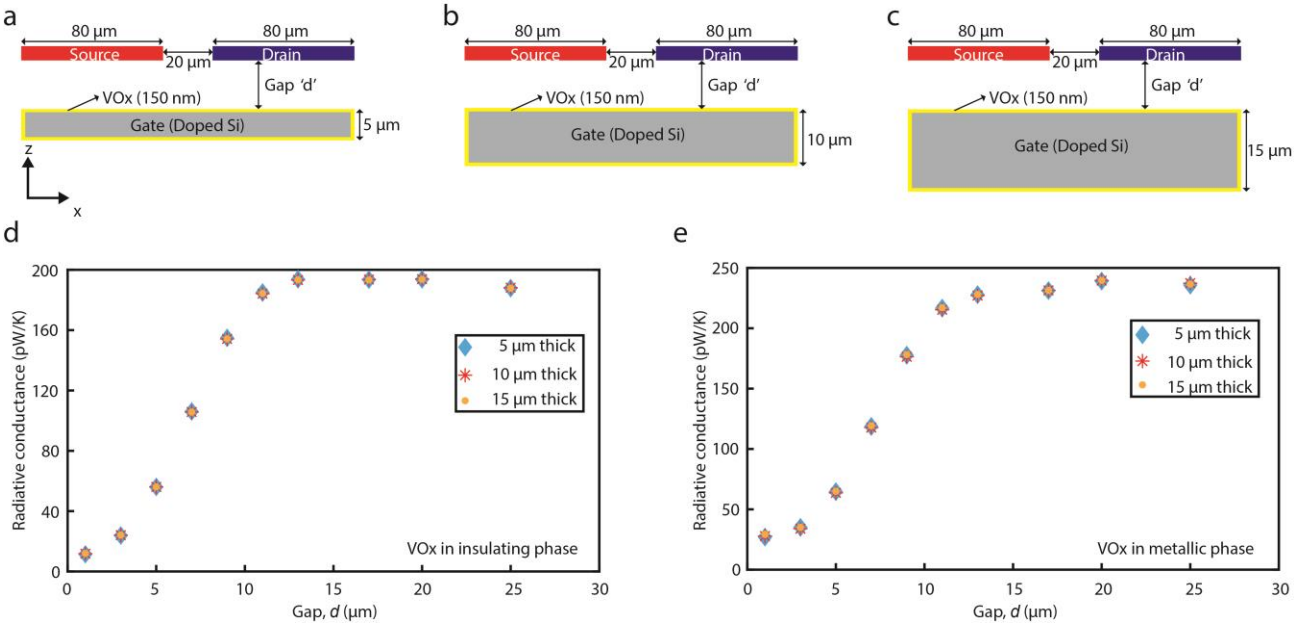


Figure 2-8. Demonstration of gate thickness independence for SCUFF-EM calculations. (a) Schematic of the model used in the calculations. (b) Same as case (a), but with the doped Si gate thickness changed to 10 μm. (c) Same as case a but with the doped Si gate thickness changed to 15 μm. (d) Radiative conductance calculation for cases (a), (b), and (c) with $VO_x$ in the insulating phase. (e) Same as (d), but with $VO_x$ in the metallic phase.

***Electrical characteristics of the source and drain devices***

To characterize the thermal properties of the source and drain devices, we employed two half-Wheatstone bridges, as shown in Figure 2-9a. An alternating current (IAC) was applied to the half-Wheatstone bridge. A potentiometer, $R_{mat}$, was connected in series with the Pt serpentine line integrated into the device ($R_{Pt,\ S}$ for source and $R_{Pt,\ D}$ for drain) to balance the circuit. To characterize the thermal conductance of the source and drain devices, we used two-stage amplification with a gain of 1 for all three instrumentation amplifiers (AD524) to achieve a good common mode rejection. The output of the circuit was continuously monitored during the experiment using a lock-in amplifier (SR 830, Stanford Research System).

We first characterized the electrical properties of the Pt resistance thermometer integrated into the source device. The source was placed on the cold finger of the cryostat (Janis ST-100), whose temperature was controlled by the Lakeshore 335 temperature controller under a vacuum level of less than $10^{-3}$ Torr. At each temperature, the resistance of the Pt serpentine was measured by applying an alternating current ($I_{AC}$ = 1 μA) through the serpentine at a frequency of 101 Hz using a Keithley 6221 current source, ensuring negligible self-heating. At the same frequency (101 Hz), the voltage ($V_f$) across the Pt resistance thermometer (PRT) was measured using a four-probe scheme with an SR830 lock-in amplifier to determine the resistance. The measured resistance within the temperature range of 299 K to 310 K is shown in Figure 2-9b, and the measured slope (dR/dT) was found to be 29.50 ± 0.138 Ω/K with good linearity for small temperature differences. The corresponding TCR was calculated as $1.75\times10^{-3}$ $K^{-1}$ using the expression: $\alpha = (1/R)\times dR/dT$ (measured resistance of the source device is ~16.857 kΩ at 25 ℃).

Next, we measured the beam conductance ($G_{beam}$) of the source device. The thermal conductance of the source ($G_{beam}$) is determined using a 3$\omega$-measurement method by applying a

sinusoidal current with a fixed frequency of 1 Hz to the platinum resistor of the source device. The current amplitude ($I_{AC}$) is adjusted in steps (using Keithley 6221), ranging from 6 μA to 12 μA, to generate a temperature modulation at 2 Hz. To measure the temperature change, the corresponding $V_{3f}$ was measured using an SR830 lock-in amplifier while various $I_{AC}$ were applied. The resulting temperature change is calculated using the following equation: $\Delta T_{2f} = 2\Delta V_{3f}/I_f R\alpha$ as explained above.

Figure 2-9c illustrates the power dissipation at the PRT ($Q_{2f}$=$I_{AC}^2R/2$) as a function of temperature rise ($\Delta T_{2f}$) on the source. A clear linear correlation is observed in the examined temperature range. The slope of this line corresponds to the beam thermal conductance of the source device, which is measured to be 250 ± 3 nW/K. For the drain device, electrical characteristics are almost identical to those of the source device since they were fabricated under the exact same procedure. Using the same method employed for measuring the beam thermal conductance of the source device, the measured beam conductance of the drain is determined to be 249 ± 2 nW/K.

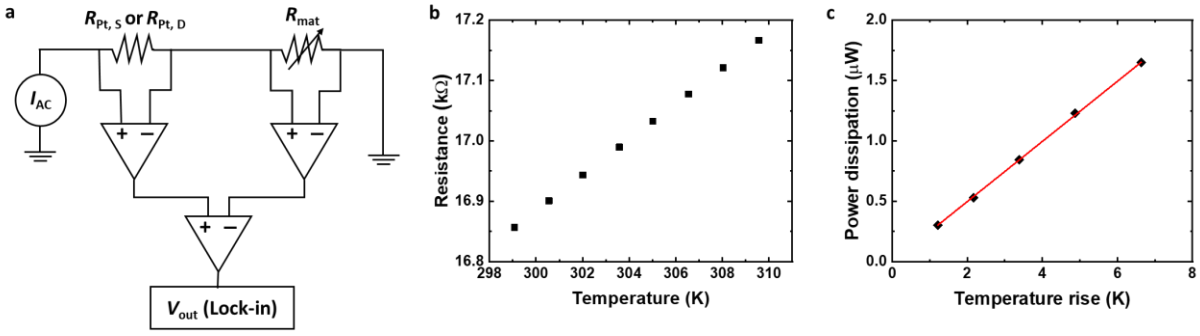


Figure 2-9. Characterization of the electrical and thermal properties of the source device. (a) An electronic circuit is used to measure temperature change by monitoring resistance change. (b) The temperature dependence of the integrated Pt resistance was measured near room temperature. (c) The relationship between temperature rise on the source device and the power dissipation, produced by the Pt heater, is illustrated. The measured beam conductance is represented by the slope, denoted by the red solid line.

***Characterization of a gate device coated with a 150 nm-thick $VO_x$ Layer: Estimate of the gate device temperature and thermal conductance ($G_{Gate}$)***

Due to the significant temperature change of the gate ($\Delta T_g$ ~100 K) in comparison to the source ($\Delta T_s$ ~5 K) during experiments, the linear approximation (where $\alpha\Delta T<<1$) is not applicable, since the resistance does not vary linearly with respect to temperature. To determine the temperature of the gate, the thermal conductance of the gate ($G_{Gate}$) needs to be characterized.

To characterize the thermal conductance of the gate, we estimated the temperature change based on the applied power by considering the resistance change. First, we measured the resistance while varying the temperature, as shown in Figure 2-10a. This was done by applying a low amplitude current (fixed $I_{AC}$ = 10 μA) at high frequency ($f$ = 101 Hz) to eliminate self-heating while the temperature was adjusted inside a cryostat (Janis ST-100) under vacuum conditions (less than $10^{-3}$ Torr). Next, we obtained the resistance change as a function of dissipated power by applying a bipolar voltage (ranging from 0 V to ± 4.0 V with an E3631A power supply) to the gate under vacuum conditions (Figure 2-10b). The resistance was determined from the measured current (using a 34401A digital multimeter) through the application of Ohm's law, as depicted in the inset of Figure 2-10b. From these measurements, by comparing the resistance of the gate shown in Figure 2-10a and 2-10b, we obtained the temperature as a function of the given power (Figure 2-10c). The measured temperature of the gate at various bipolar voltage is as follows: 25 ℃ at 0 V, 33 ℃ at ±1.0 V, 54 ℃ at ±2.0 V, 68 ℃ at ±2.5 V, 83 ℃ at ±3.0 V, 100 ℃ at ±3.5 V, and 117 ℃ at ±4.0 V, respectively, with a temperature uncertainty of < ±1 K for each measurement. The derivative of power (in mW) with respect to temperature (in K), indicates the thermal conductance of the gate ($G_{Gate}$).

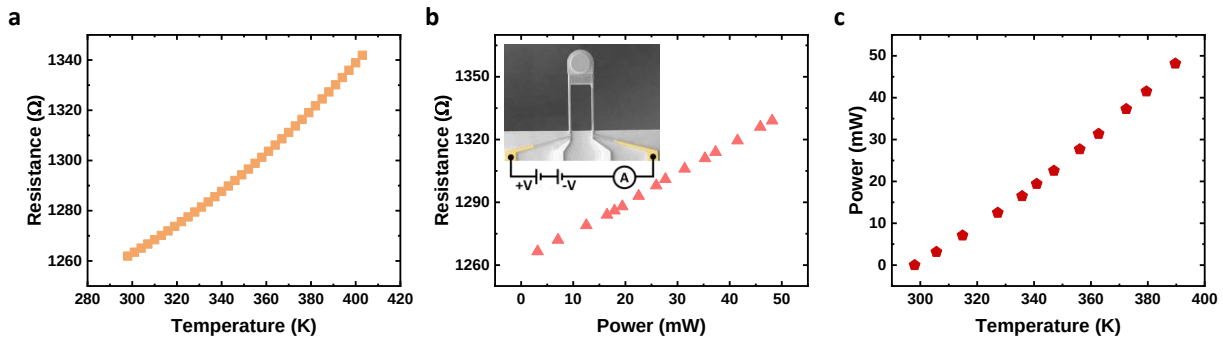


Figure 2-10. (a) Measured resistance of the gate as a function of the temperature. (b) Measured resistance of the gate as a function of the applied power. Inset displays a false-colored SEM image demonstrating electrical connections during the measurement. (c) A relation between the consumed power and temperature change.

***Finite element method (FEM) simulations used for computing radiative conductance in the blackbody limit***

We compare our experimental results, which benefit from the presence of confinement of modes to the blackbody limit by simulating the radiative conductance ($G_{\text{blackbody}}$) between adjacent membranes using the COMSOL Multiphysics platform (AltaSim Technologies). COMSOL is able to model the electrical heating and heat transfer using the geometry and material parameters of the devices, including the platinum resistive thermometer, the beams, and the $VO_x$ gate (see Figure 2-11 for representative images of the COMSOL model). Unless otherwise specified, the default material parameters available in COMSOL were used. In our simulations, the ends of the beams, which are affixed to a silicon substrate in the actual devices, were given a 300 K fixed-temperature boundary condition, as was the underside of the $VO_x$ substrate, which was resting on a heat sink in the experiment. A fixed small voltage was applied to the serpentine heater on the source membrane and two of the support beams, which induced Joule heating. The surfaces of all bodies were assigned an emissivity of 1, since they are assumed to be all blackbodies. Note the thermal

conductivity used for SiN in our simulation was 3 W/(m·K) to be consistent with our measured beam conductance.

To determine the radiative conductance $G_{blackbody}$ at different gap sizes, we first used the COMSOL model (shown in Figure 2-11b, the model is discretized into a trapezoidal mesh of >60000 domain elements) to obtain the temperature rise in the source ($\Delta T_S$) and the drain ($\Delta T_D$) at different gap sizes. Next, we calculated $G_{Th}$ ($G_{Th}$, total thermal conductance of the membrane device) using $G_{Th} = P_{Joule}/\Delta T_S$ at each gap size (see Methods section for details). With these known values, the radiative conductance ($G_{blackbody}$) was computed as $G_{blackbody} = G_{Th}\Delta T_D/(\Delta T_S - \Delta T_D)$. For gap sizes between the source-drain device and the gate device of 0.5, 10, and 24 μm, the radiative conductance ($G_{blackbody}$) is nearly identical (~4 pW/K), regardless of the phase of $VO_x$. Our experimental result and this simulation result are in good agreement with the recent experimental findings that a hundred-fold enhancement in far-field radiative heat transfer over the blackbody limit can be achieved when the dimensions of objects are smaller than subwavelength dimensions[38]. Note that the FEM simulation results (see Figure 2-11d) also exhibit good temperature uniformity (<0.1% temperature difference) on the area of the suspended membranes as well as a linear change of the temperature along the support beams.

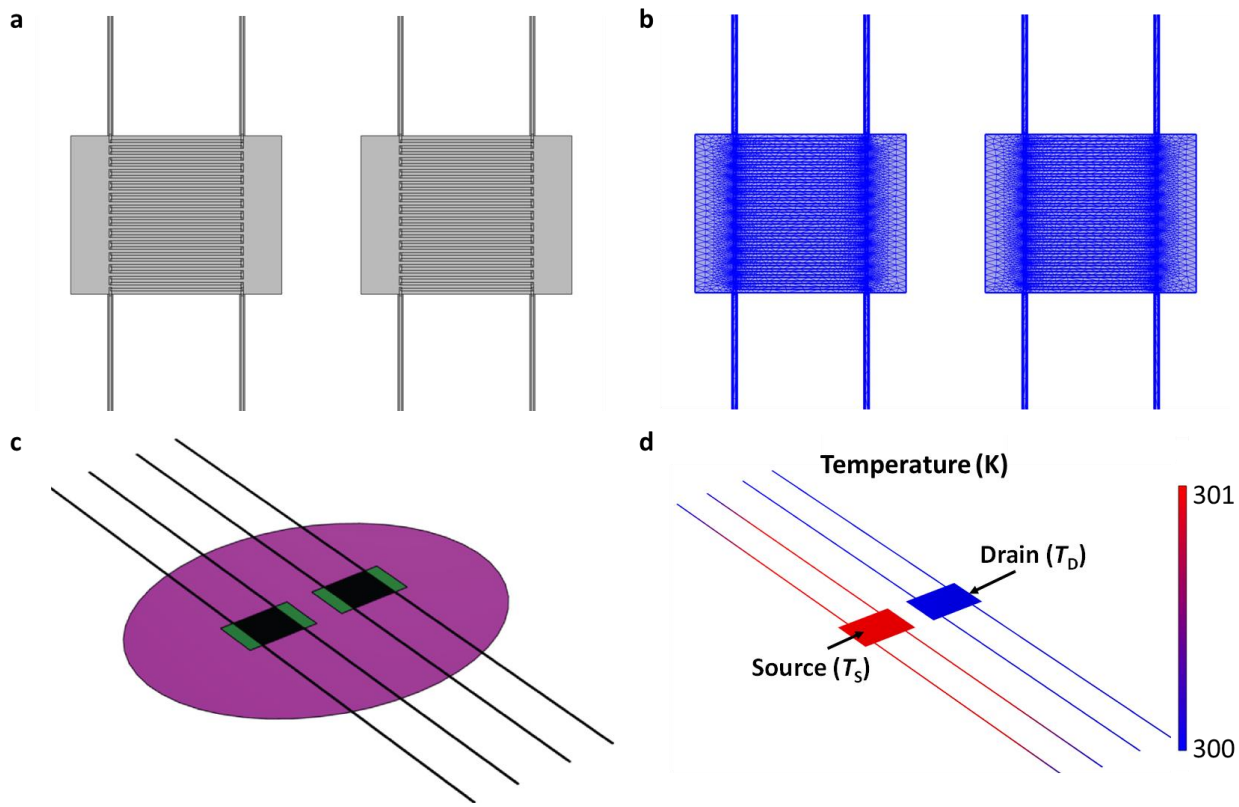


Figure 2-11. Illustrations from FEM simulations were performed to estimate $G_{blackbody}$. (a) Top view of the suspended device geometry as modeled in COMSOL. SiN membrane is dark green, Pt is light gray. (b) Discretization mesh on the suspended membrane structures. (c) The complete geometry used in the simulation, including the $VO_x$-covered substrate of the gate, is shown in purple. (d) Computed surface temperatures of the source membrane and drain membrane.

### *Displacement of the gate device due to temperature change*

To determine the physical displacement of the gate when the gate device transitions into a metallic phase, FEM analysis (COMSOL Multiphysics) was performed. To calculate the maximum displacement under the condition of the highest temperature reached during the measurement, a constant temperature of 380 K was applied to the mesa surface, while one end of the two beams was maintained at room temperature. Figure 2-12 shows the displacement of the gate along the *z*-axis, indicating that the largest displacement is less than 10 nm. This indicates that

the displacement of the gate device is negligible compared to the gap distance (*d*), even when the gate temperature reaches up to 380 K.

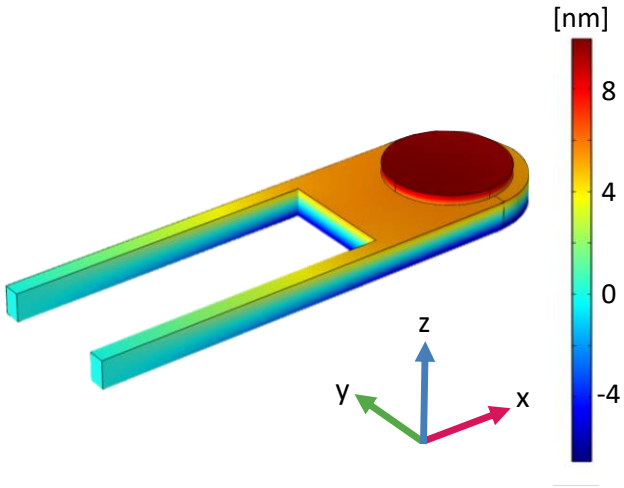


Figure 2-12. Displacement of the gate device along the z-axis when the gate device is heated up to 380 K as modelled with COMSOL.

# Chapter 3 Quantifying the Effect of Nanofilms on Near-Field Radiative Heat Transfer

## 3.1 Abstract

Recent measurements of near-field radiative heat transfer (NFRHT) between objects separated by nanometer-sized vacuum gaps have revealed that thermal radiation at the nanoscale is remarkably distinct from far-field thermal radiation and can exceed the blackbody radiation limit by orders of magnitude. Given the technological relevance of thin films, there remains a significant need to experimentally explore how such films influence NFRHT. Here, we report direct measurements of the thickness-dependence of NFRHT between planar nanofilms of magnesium fluoride (thickness ranging from 20 nm to 500 nm) performed using microfabricated devices and a custom-developed nanopositioner. These results directly demonstrate for the first time that nanofilms can enhance thermal radiation up to 800-fold above the blackbody limit and are as effective as bulk materials when nanoscale gaps have dimensions smaller than the film thickness. Finally, calculations based on fluctuational electrodynamics show good agreement with the measured gap-size dependence of the heat transfer coefficient for films of all thicknesses and provide physical insight into the observed dependence. The experimental techniques and insights reported here pave the way for systematically exploring novel thin films for near-field thermal and energy systems.

## 3.2 Introduction

The classical theory of blackbody radiation and far-field radiative heat transfer was established by Planck and his contemporaries over a century ago[79]. In contrast, research on near-field radiative heat transfer (NFRHT) has only recently begun to gain momentum[31, 80, 81], owing to the rapid advancement of nanoscience and nanotechnology. NFRHT refers to the scenario when the separation (gap) between a hot emitter and a cold receiver is comparable to or smaller than the characteristic thermal wavelength, and holds great potential for a variety of applications such as thermophotovoltaics[5, 8, 51, 82, 83], photonic refrigeration[56, 84], and thermal diodes[65, 85]. Recent experiments have unambiguously demonstrated that thermal radiation at the nanoscale is profoundly different from that in the far field and can achieve heat transfer rates exceeding the blackbody limit by a few orders of magnitude[36, 71, 86-89]. Many studies have also focused on enhancing and manipulating NFRHT with metals and dielectrics[54, 90-92], metamaterials[93, 94], and multilayer thin-film structures[36, 88, 95]. In particular, tuning NFRHT via thin films is critical for performance enhancements in thermal rectification[13, 85, 96], energy conversion[8, 82, 84], and heat-assisted magnetic recording[97]. However, to date, thermal radiation of thin films in nanometer gaps remains largely experimentally unexplored. Therefore, a key question that remains to be addressed is the following: To what extent can thin films influence NFRHT?

Researchers have computationally explored this question by performing fluctuational electrodynamics-based calculations of NFRHT using a plane-plane geometry for materials supporting electromagnetic surface modes, especially surface phonon polaritons (SPhPs), which exist at the surfaces of polar dielectrics (Figure 3-1a) and lead to orders-of-magnitude enhancement of NFRHT at nanoscale gaps[95, 98-100]. What these studies indicate is that thin films can potentially enhance NFRHT as effectively as bulk materials once the gap size becomes comparable to or

smaller than the film thicknesses. Experimental characterization of NFRHT, however, has proven fairly challenging, especially in the plane-plane configuration due to extremely stringent requirements on the surface and alignment quality. In a past study, Song *et al.* [36] probed the radiative thermal conductance between a silica ($SiO_2$) sphere and a silica thin film-coated substrate and inferred that thin films act like a bulk material for gaps smaller than the film thickness. However, given the sphere-plane geometry employed in this past work, only a small region of the curved surface could contribute to NFRHT, making it challenging to directly experimentally demonstrate the potential of thin films in enhancing thermal radiation in the near field. More recently, studies[101, 102] of supported thin metallic films in the plane-plane configuration showed enhanced NFRHT; however, these works explored NFRHT for gap sizes much larger than the film thickness and did not explore the gap size and film thickness dependence of NFRHT that we seek to address in this work.

### 3.3 Experimental Procedures and Methods

To explore NFRHT between thin films, we employed a custom-built nanopositioning platform[70] together with a microfabricated planar emitter device[82] and a flat receiver (see Supplementary Materials for fabrication details). As illustrated in Figure 3-1, in all experiments, NFRHT was probed between a pair of emitter and receiver devices coated with magnesium fluoride ($MgF_2$) films of equal thicknesses ($t$). We chose the polar dielectric $MgF_2$, as we have recently shown[54] that it features dielectric properties that are close to optimal for maximizing NFRHT at room temperature as well as due to the ease of depositing thin films of $MgF_2$ via evaporation techniques. $MgF_2$ supports SPhPs at ~67 meV where the real part of the dielectric function is -1 (see Supplementary Materials for the measured dielectric function).

The nanopositioning platform employed in this work enables parallelization of the emitter and receiver surfaces with ~6 μrad angular resolution and facilitates the formation of gaps smaller than 100 nm (Figure 3-1b). The gap size between the two surfaces is controlled using a piezoelectric actuator with 1.7 nm resolution over an ~8 μm range. To achieve nanoscale gaps, it is critical to prepare devices with flat, smooth, and clean surfaces in addition to the integration of high-resolution heating and sensing mechanisms. To this end, we fabricated the emitter device using a silicon-on-insulator wafer via the process depicted in Figure 3-5. The device features an island suspended by two long and narrow silicon (Si) beams (550 μm in length, 13 μm in width, and 40 μm in thickness) to achieve sufficient thermal isolation from the surroundings. The beam thermal conductance, $G_{dev}$, is characterized to be ~264 μW/K, as shown in Figure 3-6. The emitter also features a thin-film platinum resistor patterned in the suspended region to enable heating and high-resolution thermometry (Figure 3-1c). Further, a 15 μm-tall, 80 μm-diameter circular mesa is formed on the island, the flat top surface of which serves as the planar emitter to be coated with $MgF_2$. The use of a mesa ensures that only its well-defined top surface is in the near field of the receiver, which is essential for comparing experimental data with computational results. The receiver (Figure 3-1d) is simply a large (1 cm × 1 cm) silicon substrate (500 μm thick) coated with a $MgF_2$ film of suitable thickness. The top surface of the emitter consists of a 430 nm thick *p*-doped Si layer (dopant concentration of $2.7 \times 10^{20}$ $cm^{-3}$) followed by a 15 μm thick intrinsic Si layer (details of the multiple layers in the emitter can be found in the Supplementary Materials).

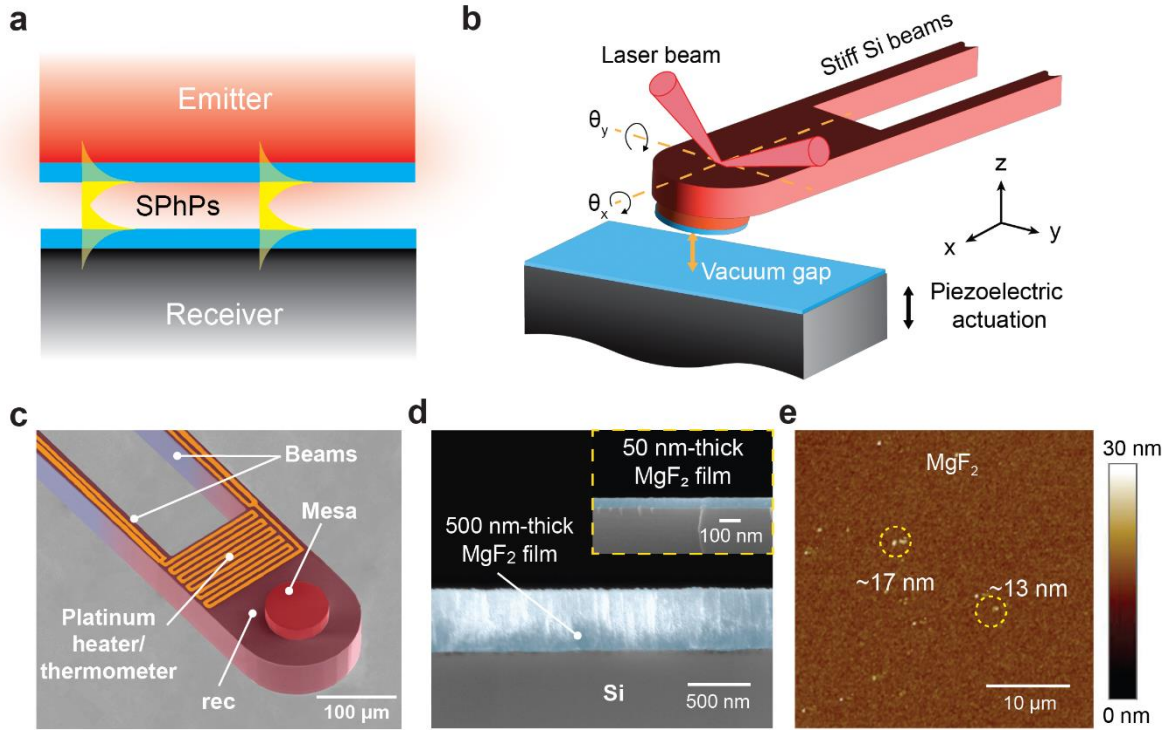


Figure 3-1. Schematics of the experimental configuration and characterization data for the microdevices and nanofilms. (a) Illustration of the coupled surface phonon polariton modes that contribute to the near field radiative heat transfer. The emitter is at a slightly higher temperature than the receiver. (b) Schematic illustration of the emitter device and receiver devices. Their relative orientation and parallelism are controlled via a custom-built nanopositioner. A laser beam reflecting off the backside of the emitter is used to monitor its physical contact with the receiver while a piezoelectric actuator controls the gap size. (c) False-colored SEM image of the emitter device indicating the 80 μm-diameter mesa surface and the platinum heater/thermometer. (d) False-colored cross-sectional SEM image of a 500 nm-thick $MgF_2$ film deposited on a pristine Si substrate. Inset shows another sample with a 50 nm-thick film. (e) AFM image of a device with a 50 nm-thick $MgF_2$ film revealing particles of sizes around 13 – 17 nm.

In this work, we prepared emitter and receiver devices with $MgF_2$ coatings of five thicknesses ($t$ = 20 nm, 50 nm, 85 nm, 176 nm, and 500 nm). Some representative scanning electron microscopy (SEM) images of the $MgF_2$ films are shown in Figure 3-1d. The $MgF_2$ films were deposited via an evaporation technique and characterized using both a Dektak profilometer and an atomic force microscope (AFM). The root-mean-square (RMS) roughness of the various coatings was found to be on the order of 3-5 nm, while the size of particulate contamination inadvertently introduced in the deposition process was found to be approximately 15 nm (Figure 3-1e shows a 35 μm × 35 μm AFM scan of a device coated with 50 nm-thick $MgF_2$). The smallest gap sizes in

different experiments reported in this work were estimated based on the particle sizes on the corresponding samples and the angular misalignment between the nominally parallel surfaces (see Supplementary Materials for more details).

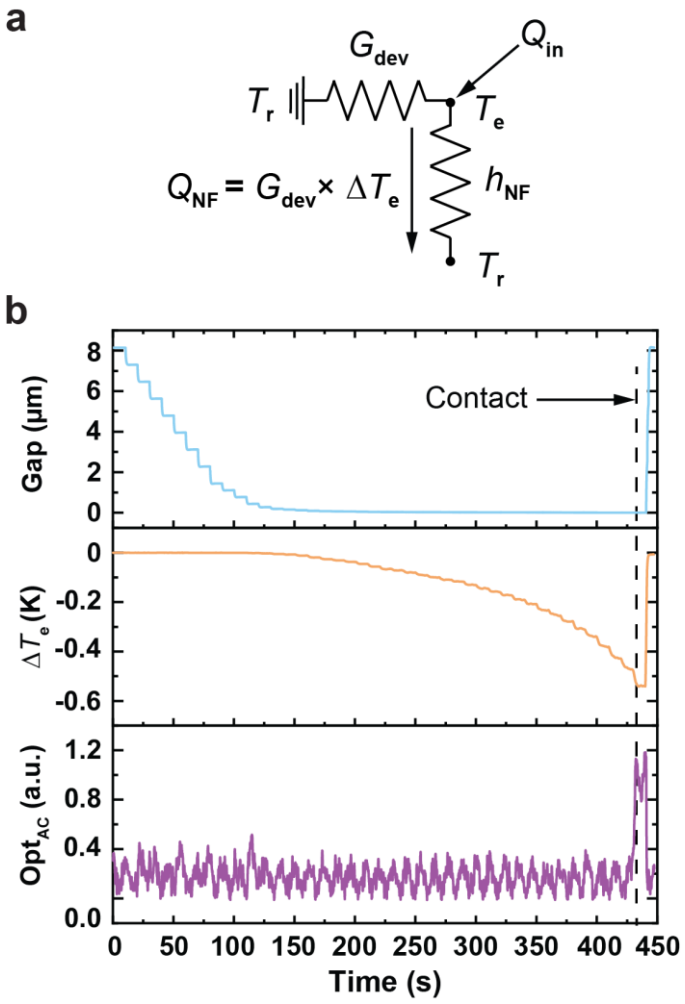


Figure 3-2. Thermal conductance network and representative experimental data. (a) Thermal conductance network describing the major heat transfer channels. The conductor (resistor) labelled $h_{NF}$ represents the near-field heat transfer coefficient and the resistor labelled $G_{dev}$ represents the beam thermal conductance ($G_{dev}^{-1}$ is the thermal resistance of the beams) of the emitter device, $T_r$ is the receiver temperature which is fixed at the ambient level (~295 K), $Q_{in}$ is the Joule heating by the platinum resistor which results in an elevated emitter temperature $T_e$, and $Q_{NF}$ is the near-field radiative heat flow. (b) Gap size between the emitter and receiver devices (top panel), temperature change of the emitter $\Delta T_e$ (middle panel), and the AC optical signal $Opt_{AC}$ (bottom panel) as a function of time, while the gap size is reduced from ~8 μm to physical contact. The continuous change in $\Delta T_e$ is due to near-field enhancement of the radiative conductance, while the sudden and simultaneous change in $Opt_{AC}$ is due to physical contact between the emitter and receiver devices.

To measure the radiative heat flow between the emitter and receiver, we started experiments using devices coated with 50 nm thick $MgF_2$ films. The devices were precisely aligned using the custom-built nanopositioner (detailed procedure can be found in our previous works[54, 87, 103]) and then maintained at a high vacuum of ~1 μTorr to minimize thermal transport via air conduction and convection. The emitter is heated to a temperature $T_e$ above the temperature of the receiver, $T_r$, by passing a DC current through the platinum heater. The gap is then systematically reduced in steps whose size is varied from ~200 nm at large gaps to ~2 nm at the smallest gap size using the piezoelectric actuator. The temperature variation of the emitter, $\Delta T_e$, is continuously monitored by using a sinusoidal AC current (70 μA at 497 Hz) imposed on the DC current. The voltage change resulting from the resistance change of the platinum thermometer is measured using a lock-in amplifier (see Supplementary Materials for details of device characterization). As the gap size is reduced from 8 μm to 1 μm, no significant change in $\Delta T_e$ is observed, as the plates are relatively in the far field (Figure 3-2b shows representative data for devices coated with 50 nm thick films). For gap sizes below ~1 μm, a large change in $\Delta T_e$ is observed as the gap size is reduced due to an increasingly larger near-field enhancement. To establish physical contact between the devices, we shine a low power red laser on the backside of the emitter (Figure 3-1b) and collect the reflected light with a split photodetector. A small sinusoidal voltage is superimposed on the DC voltage applied to the piezoelectric actuator, so that the receiver also oscillates with an amplitude of ~2 nm at a frequency of 3 kHz. The voltage component at 3 kHz ($Opt_{AC}$) in the signal obtained from the photodetector is continuously monitored and remains negligibly small until the emitter comes into contact with the receiver. A sudden change in $Opt_{AC}$ clearly indicates that physical contact is established between the devices (Figure 3-2b). Beyond this point, the heat flow

is dominated by conduction through the emitter-receiver interface instead of thermal radiation and is therefore not of interest in this study.

### 3.4 Results and Analysis

The radiative heat flow across the gap is obtained as $Q_{NF} = G_{dev} \times \Delta T_e$, where $G_{dev}$ is the beam thermal conductance of the emitter device. The near-field radiative heat transfer coefficient (HTC), $h_{NF}$, is then calculated as $Q_{NF}/A_{mesa}$ ($T_e$ - $T_r$), where $A_{mesa}$ is the area of the mesa surface in the near field. To this measured signal, we add a calculated far-field component $h_{FF}$ at a gap size of 8 μm, to obtain the total HTC, $h_{RHT} = h_{NF} + h_{FF}$. The variation of $h_{RHT}$ as a function of gap size from experiments with different thicknesses of $MgF_2$ is presented in Figure 3-3a. In this experiment, we observed an increase in HTC from ~3 W $m^{-2}$ $K^{-1}$ at an 8 μm gap to 2200 W $m^{-2}$ $K^{-1}$ at a gap size of 50 nm. Thus, at a gap size of 50 nm, a 360-fold enhancement in NFRHT is achieved for $MgF_2$ compared to the blackbody limit (black horizontal dashed line in Figure 3-3a).

To address the question of near-field enhancements in thin dielectric films, we repeated the gap-dependent measurements for devices with four other $MgF_2$ film thicknesses (500, 176, 85, and 20 nm). The 500 nm thick coating, which is the largest thickness achieved in this work, was chosen so as to approximate a bulk material[54]. As shown in Figure 3-3a by various colored squares, we observed clear enhancements of NFRHT for all of the film thicknesses. For instance, a 500 nm thick coating on the devices results in a HTC of 2340 W $m^{-2}$ $K^{-1}$ at a gap size of 60 nm, which represents a 380-fold increase compared to the blackbody limit. In fact, even for the thinnest film, we observe an 800-fold enhancement in NFRHT compared to the blackbody limit, at a gap size of 30 nm. It is clear from these data that as the gap size is reduced the HTC values associated with all the films converge to similar values. Specifically, we find that the HTC values for films of thicknesses 85 nm, 176 nm, and 500 nm converge to the same value for gap sizes smaller than 200

nm, while those for the other two thinner films (20 nm and 50 nm) also become relatively large and close to the values of the thick films. These results highlight the effectiveness of thin films in supporting NFRHT in nanoscale gaps.

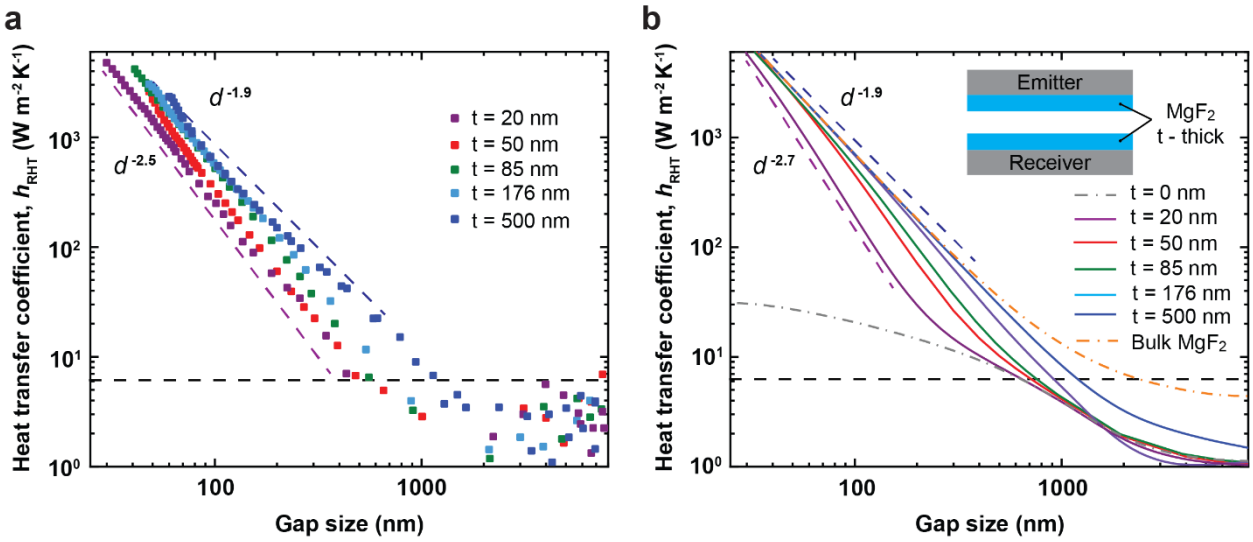


Figure 3-3. Measured and calculated near-field heat transfer coefficients. (a) Experimentally measured HTC as a function of gap size (varied from 8 μm to ~30 nm). Data for different $MgF_2$ film thicknesses is represented by different colors. The dashed lines represent power-law fits to the 500 nm and 20 nm cases. Note that for the 50 nm-film case, the data point at ~8 μm gap lies slightly above the blackbody limit, which likely stems from the small signal-to-noise ratio in the far field or uncertainties in estimating the far-field background for the experimental data. (b) Theoretical calculations based on fluctuational electrodynamics. The inset shows the schematic of the emitter and receiver devices coated with '*t*' nm-thick $MgF_2$ films. Each solid curve corresponds to a different $MgF_2$ thickness. The dashed lines are power-law fits to the 500 nm and 20 nm cases. The gray dash and dot line correspond to devices with no $MgF_2$ coating ($t$ = 0) and the orange dash and dot line correspond to bulk $MgF_2$ devices. The horizontal black line in both figures corresponds to the blackbody limit. The power-law exponents were obtained by fitting the data at gap sizes ranging from 30 nm to 200 nm. All the experiments were performed at room temperature (~300 K) with a ~10 K temperature difference between the emitter and the receiver. For the theoretical calculations, the emitter and receiver were assumed to be at 301 K and 300 K, respectively.

To compare our measurements with theory, we calculated NFRHT for the multilayered structures using fluctuational electrodynamics (FED) [104, 105]. In these calculations, the emitter is treated as a six-layer one-dimensional structure and the receiver is treated as a two-layer one-dimensional structure (see Supplementary Materials for details) and the radiative heat transfer coefficient in the linear regime is calculated as equation (3-1):

$$h(T,d) = \int_0^\infty \frac{d\omega}{4\pi^2} \frac{\partial(\hbar\omega/\exp(\hbar\omega/(k_B T_i - 1)))}{\partial T} \int_0^\infty dk k \left[\tau_s(\omega,k) + \tau_p(\omega,k)\right], \quad (3\text{-}1)$$

where $T$ is the temperature of the system (300 K), $d$ is the gap size, $\omega$ is the angular frequency, $k$ is the wave-vector component parallel to the planar surfaces, $\hbar$ is the reduced Planck constant, and $\tau_s$ and $\tau_p$ are the transmission probabilities of the *s*- and *p*-polarized modes calculated based on the Fresnel reflection coefficients in both devices (see Supplementary Materials for details). The dielectric properties of $MgF_2$ are required as input and were measured by us as reported in a previous work[54]. The dielectric properties of the Si substrate were obtained from ref.[106].

The computed results for HTC shown in Figure 3-3b (solid lines) and are in good agreement with the corresponding measured data in Figure 3-3a. It can be seen that the HTC for thicknesses ranging from 50 nm to 500 nm converge to the HTC value of the 500 nm thick film, as the gap size is reduced from 8 μm to ~50 nm. We also plot the theoretical expectation for both the bulk case (orange dash and dot line), where both the emitter and receiver structures are assumed to be homogeneous, semi-infinite bodies made of $MgF_2$ and the zero-thickness case (gray dash and dot line) where there is no $MgF_2$ coating on the devices. As can be seen from the calculations, the bulk case deviates from the nanofilm cases in the far field, but merge with the thin film cases in the near field (i.e., for gap sizes much smaller than the film thicknesses). We also note that for the uncoated devices the expected HTC is much smaller than that of the coated devices for small gap sizes revealing the impact of thin films on NFRHT.

To understand the dependence of NFRHT on film thickness, we start by noting that for gap sizes ($d$) smaller than the thickness ($t$) of the films and under electrostatic approximation ($|k| \gg \omega/c$, where $c$ is the speed of light in vacuum), it can be shown[36] that dispersion relationship for the cavity SPhPs for all film thicknesses become identical. Moreover, the frequency-dependent

penetration depth, $l(\omega)$, of such cavity SPhPs is also independent of film thickness and can be approximated as (see Supplementary Materials for details) equation (3-2):

$$l(\omega) \approx \frac{d}{2\mathrm{Re}\left[\ln\left(\frac{\varepsilon(\omega)-1}{\varepsilon(\omega)+1}\right)\right]}, \tag{3-2}$$

where $\varepsilon(\omega)$ is the permittivity of the dielectric film ($MgF_2$). Since the denominator is on the order of unity, for gaps smaller than the thickness of the films, the penetration depth scales approximately as the gap size *d*. This implies that the SPhP modes that contribute to heat transfer are completely contained in a shallow region of length *l*. Therefore, they contribute to HTC in the same way for both thin and thick films, due to which the gap-dependent NFRHT for thin films converges to the bulk case when the gap becomes comparable to or smaller than the film thickness.

We note that past theoretical and experimental work[107, 108] has shown that for bulk materials supporting SPhPs, the gap dependence of HTC, for small gaps, scales approximately as $1/d^2$. Our experiments on 500 nm thick $MgF_2$ devices indeed reveal a scaling on the order of $1/d^{1.9}$ (blue dashed line in Figure 3-3a), which is consistent with our calculations (blue dashed line in Figure 3-3b). In contrast to the gap dependence of thick films, we observe that for the thinnest film (20 nm), the gap dependence of the NFRHT in the 30 nm – 200 nm range features a much steeper $1/d^{2.5}$ dependence, which is again consistent with theory. This behavior can be attributed to the fact that modes that are originally contributing to NFRHT in the bulk films also become available for NFRHT in thin films when the penetration depth scales as the gap size.

To provide additional insight into the nature of NFRHT supported by thin films, we computed the spectral radiative flux (Figure 3-4a) and the transmission probabilities of the *p*-polarized modes (Figure 3-4b) for devices coated with 50 nm thick $MgF_2$ films (at various gap sizes). We note that we focus on the *p*-polarized modes, as they make dominant contributions to

NFRHT (see Supplementary Materials for details). In these calculations, we make the simplifying assumption that the $MgF_2$ films are coated on semi-infinite Si substrates (inset of Figure 3-4a). We made this simplification to reduce the computational complexity. This assumption is valid, as the major contribution to NFRHT comes from materials very close to the vacuum gap.

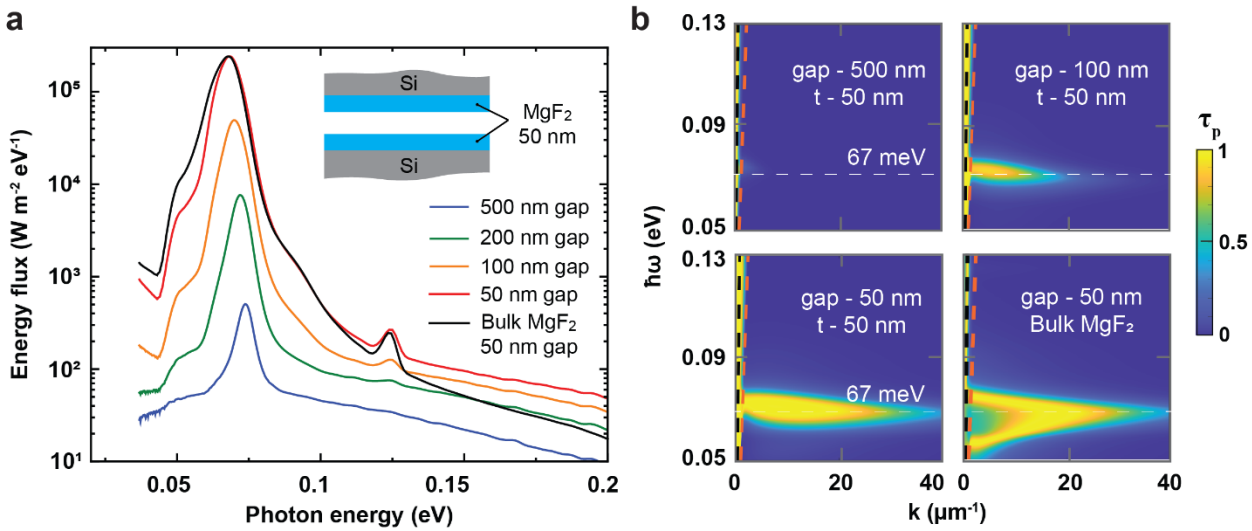


Figure 3-4. Spectral characteristics of NFRHT and transmission probabilities for p-polarized modes. (a) Radiative energy flux as a function of photon energy for 50 nm-thick $MgF_2$ films on Si substrate for gaps ranging from 50 nm to 500 nm. The black curve is the spectral flux for two bulk $MgF_2$ plates at a gap size of 50 nm. The inset describes the simplified geometry being considered. (b) The transmission probabilities for the *p*-polarized modes, plotted as a function of photon energy and the magnitude of the parallel wavevector *k*. The insets in the panels specify the film thickness and gap size. The black dashed line is the light line in vacuum while the orange dashed line is the light line in Si. The white dashed line indicates the frequency at which Re(ε) of $MgF_2$ is around -1, where surface phonon polaritons are supported.

Our calculations (Figure 3-4a) show that for 50 nm thick $MgF_2$ films, for all gap sizes of interest (50 nm to 500 nm), NFRHT peaks at ~67 meV. Further, the computed transmission probabilities (Figure 3-4b) for the same films show that the transmission probability is very small at a gap size of 500 nm, but as the gap size is reduced to 100 nm and then to 50 nm, the transmission probability increases substantially (second and third panels of Figure 3-4b). It can also be seen that, as the gap size reduced, the transmission probability for modes with larger magnitudes of the wavevector ($k$) increases. Further, it can be seen that the transmission probability for the 50 nm

thick films at a gap size of 50 nm (Figure 3-4b bottom left panel) has strong contributions from SPhPs with large *k* vectors, similar to the case for bulk materials (Figure 3-4b bottom right panel). As noted earlier, such large *k* vectors have a shallow penetration depth comparable to or smaller than the film thickness, resulting in similar NFRHT fluxes for both thin and thick films (Figure 3-4a).

We note that the underlying Si also makes some contribution to NFRHT over a broad frequency range due to its frustrated modes that couple across the vacuum gap. This is evident from Figure 3-4b, where evanescent modes between the light lines in vacuum (black dashed line) and in Si (orange dashed line) start getting populated for gap sizes below 500 nm but are missing in the transmission probability plot for the bulk case. Thus, the total HTC in our system has the largest contribution from the SPhP modes around 67 meV and a very small contribution from evanescent waves over the whole spectral range.

### 3.5 Conclusion

To summarize, we report the first experimental studies of NFRHT between nanometer-thick films of polar dielectrics at gaps of tens of nanometers. Our data reveal that as the gap size becomes comparable to or smaller than the film thickness, the heat transfer coefficient between thin films approaches that of the bulk. This is because the penetration depth of the cavity SPhP modes that dominate NFRHT becomes smaller than the film thickness when the gap size becomes very small (i.e., smaller than the film thickness). We also show that at small gap sizes, the heat transfer rate increases much more rapidly for thin films than what would be expected for bulk substrates. Further, our spectral radiative flux and transmission calculations clearly indicate that NFRHT is dominated by energy transfer over a narrow range of frequencies corresponding to large

*k* vectors that have a shallow penetration depth. The insights achieved in this work will enable future developments in near-field energy conversion.

### 3.6 Supplementary Materials

#### *Fabrication of the emitter device and deposition of $MgF_2$ film*

The fabrication process of the emitter device is depicted in Figure 3-5. The process begins with a double silicon-on-insulator (SOI) wafer with a 15 μm-thick top crystalline-Si device layer, 40 μm-thick Si middle layer, 500 μm-thick Si handle layer, and two layers of 1 μm-thick silicon dioxide layers (Step 1). Next, a 430 nm thick layer on the top is doped to $2.7\times10^{20}$ $cm^{-3}$ via phosphorous diffusion at 975° C. Subsequently, the top device layer is patterned and etched using a reactive ion etching (RIE) tool to form the 15 μm-thick mesa structure (Step 3). Two layers of metals: titanium 5 nm/platinum, 30 nm (Step 4) and titanium 5 nm/platinum 100 nm-thick (Step 5), are deposited by evaporation and lift-off techniques to create the heater/thermometer and electrical contacts. The two oxide layers and the 40 μm-thick middle Si layers are etched successively in an RIE process (Step 6) to define the device structure. The device is then released using a through-etch process that involves etching the 500 μm-thick Si until the oxide stop layer (Step 7). Finally, the devices are coated with different thicknesses of $MgF_2$ films using an evaporator (SJ-20 Evaporator).

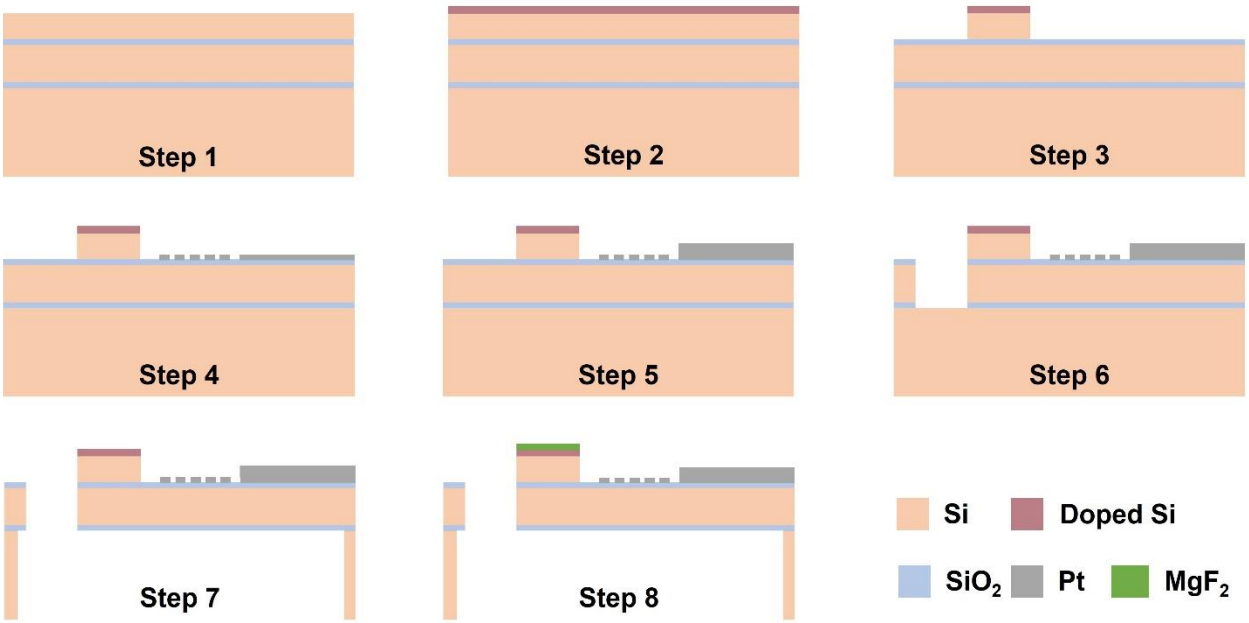


Figure 3-5. Fabrication process for the emitter device.

***Characterization of platinum thermometry***

The temperature coefficient of resistance (TCR) of the thin-film platinum resistor was determined through independent measurements. In this process, the fabricated device was affixed to the cold finger of a Janis ST-100 cryostat the temperature of which was regulated with a Lakeshore 335 controller. A Keithley 6221 current source was used to pass a 1 μA current at a frequency of 497 Hz through the device, while the amplitude of the sinusoidal voltage signal was recorded using an SR830 lock-in amplifier. The changes in the resistance of the device with temperature are illustrated in Figure 3-6a, showing excellent linearity. The slope of the linear fit is $7.15 \pm 0.15\ \Omega\ K^{-1}$, which combined with a room-temperature resistance of about 3860 Ω yields a TCR of $\alpha = 1.86 \pm 0.03 \times 10^{-3}\ K^{-1}$.

***Frequency response of the emitter***

To characterize the frequency response of the emitter, a sinusoidal current was passed through the platinum resistor with an amplitude of $I_{AC}$ = 100 μA and a varying frequency, *f*, from 0.2 Hz to 600 Hz. As a result, the emitter experiences a heat dissipation with a DC component and an AC component at 2*f*, $Q_{2f} = I_{AC}^2 R_0/2$, where $R_0$ is the resistance without heating. This leads to an oscillation in the emitter temperature at *2f*, $\Delta T_{2f}$, which in turn results in a corresponding resistance change at *2f*. The amplitude of the sinusoidal voltage is then measured at the third harmonic, $\Delta V_{3f}$, which yields the temperature modulation as equation (3-3).

$$\Delta T_{2f} = \frac{2\Delta V_{3f}}{I_{AC} R \alpha} \tag{3-3}$$

The plot in Figure 3-6b shows the variation of the modulated temperature as a function of frequency. A flat thermal response is obtained for frequencies below ~3 Hz.

***Thermal conductance of the beam***

Using a 3*f*-measurement technique, we measured the thermal conductance of the beams connecting the suspended device with the substrate ($G_{dev}$). This involves passing a sinusoidal current at a fixed frequency of 1 Hz through the platinum resistor and changing the amplitude from 300 μA to 1.2 mA, thus creating a temperature modulation at 2 Hz. The resulting temperature modulation $\Delta T_{2f}$ due to the heat dissipation, $Q_{2f} = I_{AC}^2 R/2$, is plotted in Figure 3-6c, showing a good linear relation. The slope of the line then yields a device thermal conductance of ~264 ± 1.3 μW $K^{-1}$.

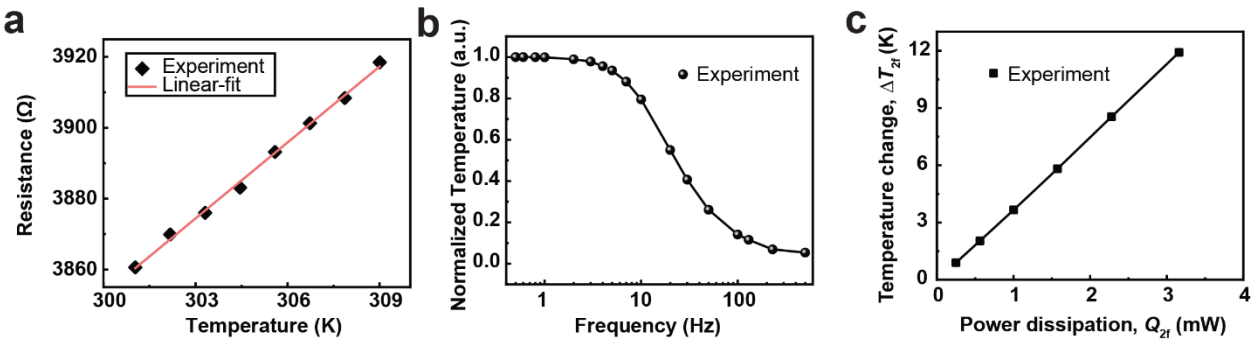


Figure 3-6. Thermal characterization of emitter devices. (a) The resistance change as a function of temperature is plotted for different temperatures. The red line indicates the linear-fit used to obtain the slope of the curve. (b) The temperature change $\Delta T_{2f}$ measured as a function of the frequency of the current excitation in the platinum resistor. (c) The temperature change, $\Delta T_{2f}$, measured as a function of the power dissipated, $\Delta Q_{2f}$, in the device. The slope of a linear fit is used to obtain the thermal conductance of our devices. Solid lines in (b) and (c) are added as guides to the eye.

### *Measured radiative heat transfer coefficient*

As discussed briefly in the main manuscript, we measure the heat flux change $Q_{NF} = G_{dev} \times \Delta T_e$, as a function of the gap size, where $G_{dev}$ is the beam thermal conductance of the emitter device and $\Delta T_e$ is the change in the emitter's temperature as the gap size is reduced. The total heat transfer, $Q_{tot}$ (= $Q_{mesa}$ + $Q_{rec}$), from the emitter to the receiver has contributions from 'mesa' and 'rec' regions of our emitter whose areas are denoted respectively by $A_{mesa}$ and $A_{rec}$. Here, 'mesa' is the 80 µm diameter surface that comes into the near field of the receiver while 'rec' is the recessed region on the emitter that is always in the far field of the receiver. The heat transfer coefficient $h_{RHT}$ is then defined as $Q_{tot} / A_{mesa} (T_e - T_r)$. In the far field (at gap size of ~8 µm), $h_{RHT}$ can be written as $[Q_{mesa} / A_{mesa} (T_e - T_r)] + [Q_{rec} / A_{mesa} (T_e - T_r)]$. The first term here is $h_{mesa}$ which is theoretically estimated as detailed below. For our devices coated with films of different thicknesses, this value is ~1 W m$^{-2}$ K$^{-1}$. Since $A_{rec} = 2A_{mesa}$, the effective $h_{RHT}$ in the far field is ~3 W m$^{-2}$ K$^{-1}$. Thus, we add a far-field component, $h_{FF}$ of 3 W m$^{-2}$ K$^{-1}$ to the measured radiative heat transfer coefficient $h_{NF}$. We note that, at gap sizes over 2 µm, the data is noisy due to the resolution of our measurements but the mean value of all the measurements remains ~3 W m$^{-2}$ K$^{-1}$.

***Theoretical calculations***

To calculate the near-field radiative heat transfer (NFRHT) for the structures used in this study, we employ the theoretical framework of fluctuational electrodynamics. Both the emitter and the receiver are treated as multilayer structures as illustrated in Figure 3-7. The heat transfer coefficient between the emitter and the receiver (as described in the main section as well), both at temperatures close to the room temperature, $T$ = 300 K, is given by equation (3-4):

$$h(T,d) = \int_0^\infty \frac{d\omega}{4\pi^2} \frac{\partial(\hbar\omega/\exp(\hbar\omega/(k_B T-1)))}{\partial T} \int_0^\infty dk k \left[\tau_s(\omega,k) + \tau_p(\omega,k)\right], \quad (3\text{-}4)$$

where $d$ is the gap size, $\omega$ is the angular frequency, $k$ is the magnitude of the parallel component of the wavevector, $k_B$ is the Boltzmann constant, $\tau_{\alpha=s,p}$ are the transmission probabilities of *s*- and *p*-polarized modes across the vacuum interface. The transmission probability is expressed as a function of the Fresnel reflection coefficients $R_\alpha^{e/r}$, where the superscript e represents the emitter and r the receiver. The transmission probabilities are calculated as equation (3-5).

$$\tau_{\alpha=s,p}^{12}(\omega,k) = \begin{cases} \frac{(1-|R_\alpha^e|^2)(1-|R_\alpha^r|^2)}{|D_\alpha|^2}, \text{if } k < \omega/c, \text{ propagating waves} \\ \frac{4\,\mathrm{Im}(R_\alpha^e)\,\mathrm{Im}(R_\alpha^r)e^{-2\,\mathrm{Im}(\gamma_0)d}}{|D_\alpha|^2}, \text{if } k > \omega/c, \text{ evanascent waves} \end{cases}, \quad (3\text{-}5)$$

$$D_\alpha = 1 - R_\alpha^e R_\alpha^r e^{2i\gamma_0 d} \quad (3\text{-}6)$$

Here, $\gamma_i = \sqrt{\varepsilon_i(\omega)\,\omega^2/c^2 - k^2}$ is the perpendicular component of the wavevector in medium $i$, $c$ is the speed of light, $\varepsilon_i(\omega)$ is the frequency-dependent dielectric function of medium $i$, and the index 0 refers to the vacuum layer. The Fresnel coefficients of the multilayer structure are calculated based on standard theory of layered media[109], including multiple reflections, transmissions, and interference effects at each interface, and are given as equation (3-7).

$$R_{\alpha=s,p}^{e/r}(\omega,k) = \frac{r_\alpha^{j,j+1} + R_\alpha^{j+1} e^{2i\gamma_{j+1}t}}{1 + r_\alpha^{j,j+1} R_\alpha^{j+1} e^{2i\gamma_{j+1}t}}. \quad (3\text{-}7)$$

Here, $r_s^{j,j+1} = (\gamma_j - \gamma_{j+1})/(\gamma_j + \gamma_{j+1})$ and $r_p^{j,j+1} = (\varepsilon_{j+1}\gamma_j - \varepsilon_j\gamma_{j+1})/(\varepsilon_{j+1}\gamma_j + \varepsilon_j\gamma_{j+1})$ are the Fresnel coefficients of a single interface between media $j$ and $j$+1 for the *s*- and the *p*-polarization, respectively, $t$ is the thickness of layer $j$+1, and $R_\alpha^{j+1}$ is the coefficient of the structure following the layer $j$+1. Thus, the effective coefficient of a multilayer structure can be calculated recursively, applying equation (3-7) at all the interfaces shown in Figure 3-7.


Figure 3-7. Schematic representation of the different layers considered in the theoretical calculations of near-field radiative heat transfer for the $MgF_2$ coated emitter and receiver devices.

***Contribution of various modes to NFRHT***

As discussed in the previous section and as represented by equations (3-4) and (3-5), the NFRHT has contributions from *s*- and *p*-polarized modes that are propagating and evanescent in nature. For materials that support surface phonon polaritons (SPhPs), for example $MgF_2$, the radiative heat transfer has dominant contributions from *p*-polarized evanescent modes[81] in the near field. To elucidate this, we employ the theory described above to plot the contributions of different modes to NFRHT for the case of devices coated with 50 nm thick $MgF_2$ and for the case of bulk $MgF_2$ half-spaces. In the far field, the RHT is dominated by *s*- and *p*-polarized modes. As the gap

size reduces, the contribution from *s*- and *p*-polarized evanescent modes starts to increase. As the gap size is further reduced to nanoscale dimensions, the RHT is predominantly enhanced by *p*-polarized evanescent modes while the contribution from other modes remains relatively low. Such trends are observed in both cases indicating that in the near field, RHT is dominated by *p*-polarized SPhP modes.

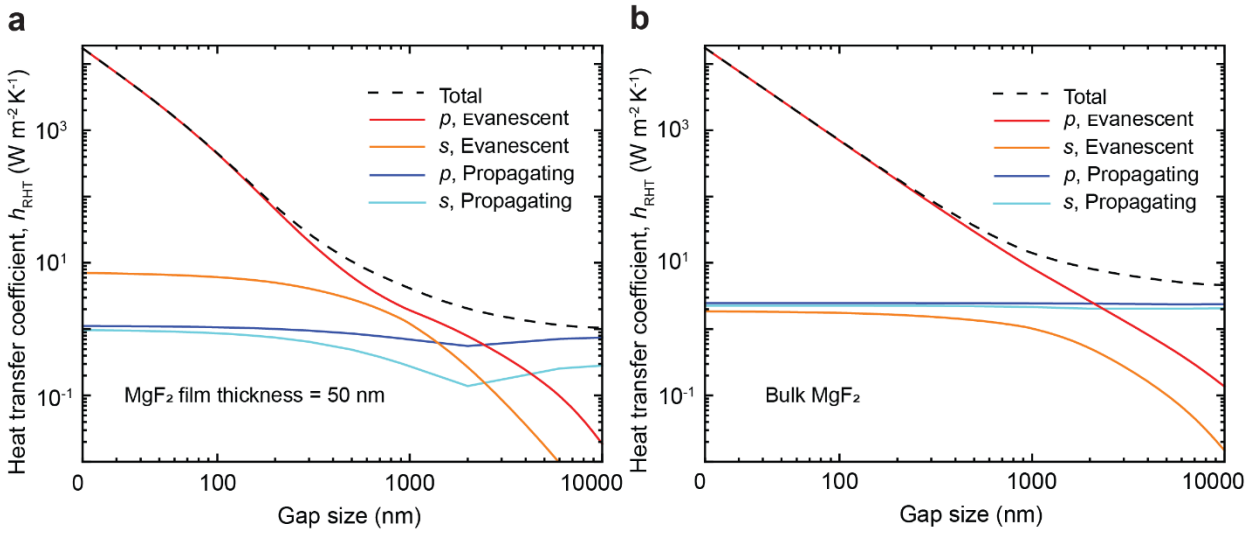


Figure 3-8. Calculation of gap-dependent heat transfer coefficient. The contribution of *s*- and *p*-polarized propagating and evanescent modes to the total heat transfer coefficient in (a) devices coated with $MgF_2$ of thickness 50 nm and (b) semi-infinite half-spaces made of $MgF_2$.

### *Origin of enhancement in thin films*

As discussed in the main text, thin films exhibit NFRHT characteristics very similar to that of bulk materials when the gap sizes are smaller than the thicknesses of the films. A comprehensive description of this is discussed in our previous work[36]. Briefly, for surface phonon-polariton mediated NFRHT, as the gap size reduces, *p*-polarized modes with large *k* vectors start contributing to the total NFRHT. This can be seen in the transmission probability plots for devices coated with 50 nm thick $MgF_2$ (Figure 3-4b), where, as the gap size reduced from 500 nm to 50 nm, increasingly larger *k* vectors contribute to NFRHT. Thus, at smaller gaps, the NFRHT is dominated by large *k* vectors leading to the observed enhancements in the near field. Further, under

the electrostatic assumption (for large $|k| \gg \omega/c$), the equation (3-7) can be approximated as $r_p^{0,1e}$ and is thus independent of the thickness of the film. The dispersion equation (3-6) can then be approximated as $D_p = 1 - r_p^{0,1e} r_p^{0,1r} e^{2i\gamma_0 d} = 0$, where the suffixes e and r are added to the superscripts to represent the emitter and receiver devices, respectively. Under these assumptions, the solution to this problem gives the dispersion relation for cavity SPhP modes as equation (3-8).

$$k_{\mathrm{SPhP}} = \frac{1}{d} \ln\left(\frac{\varepsilon(\omega)-1}{\varepsilon(\omega)+1}\right) \qquad (3\text{-}8)$$

Here, $\varepsilon(\omega)$ is the frequency-dependent dielectric function of $MgF_2$. The thickness dependency of NFRHT can be understood by looking at the penetration depth of these cavity SPhP modes, given by $l(\omega) \approx 1/(2\mathrm{Re}(k_{\mathrm{SPhP}}(\omega)))$. In the limiting case of small gap sizes, equation (3-8) allows us to approximate the penetration depth of the cavity SPhP modes as equation (3-9).

$$l(\omega) \approx \frac{d}{2\mathrm{Re}(\ln((\varepsilon(\omega)-1)/(\varepsilon(\omega)+1)))} \qquad (3\text{-}9)$$

Here, the denominator is on the order of unity and thus, the penetration depth of the modes contributing to NFRHT is on the order of the gap size, *d*. Thus, when the gap sizes are smaller than the thickness of the films, the NFRHT has predominant contributions from a thin layer with a thickness closer to the gap size. In other words, the NFRHT between thin films is the same as between bulk materials for gaps smaller than the film thickness.

***Characterization of the emitter mesa surface***

To achieve nanoscale gaps between the emitter and the receiver, it is essential that the mesa surface of the emitter device is flat, smooth, and clean. The microfabricated devices are smooth with an RMS roughness of < 1 nm. However, the deposition of $MgF_2$ on these devices results in contamination with varying particle sizes (up to 30 nm) depending on the film thickness. Since near-field radiative heat transfer can be limited not only by cantilever snap-in but also by particles

on the mesa surface, we characterized the particle sizes of all our samples using atomic force microscopy (AFM, Figure 3-9). For the 20 nm $MgF_2$ film, the mesa surface is extremely smooth (RMS roughness < 0.6 nm) with no particles. However, as the $MgF_2$ film thickness increases, a few particles that may have originated during deposition were observed. In the case of the 176 nm and 500 nm $MgF_2$ films, the roughness is < 2 nm with particle sizes of ~20 nm and ~30 nm respectively. Based on the particle sizes and the snap-in distance, we estimated the minimum gap sizes for each film in our measurements as ~30 nm, 50 nm, 40 nm, 50 nm, and 60 nm for film thicknesses of 20 nm, 50 nm, 85 nm, 176 nm, and 500 nm, respectively.

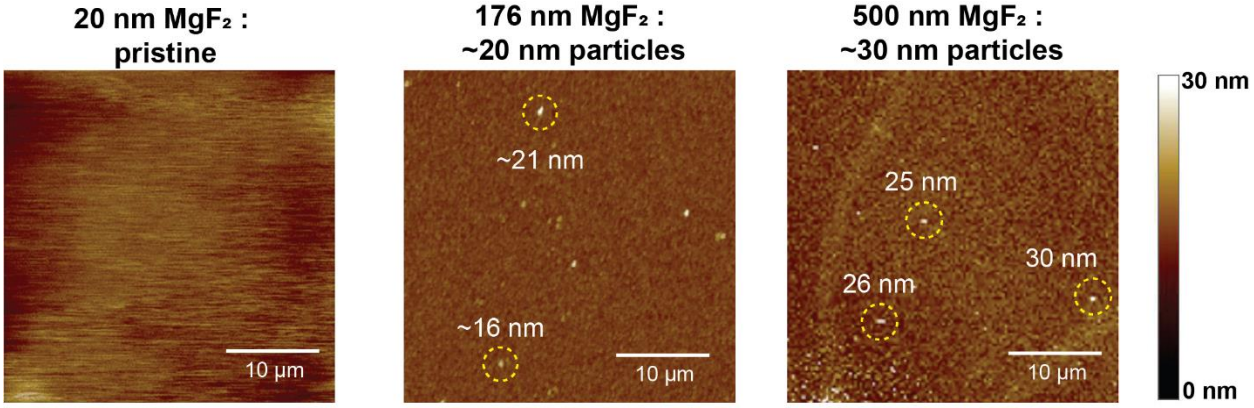


Figure 3-9. Atomic force microscopy scans of a 35×35 µm scan area on the mesa surfaces of devices coated with 20 nm, 176 nm, and 500 nm thick $MgF_2$ films. No particles were observed on the 20 nm-thick film, while particles of sizes ranging from 15 nm to 30 nm were found on thicker films.

***Dielectric functions employed in the calculation***

The dielectric functions of $SiO_2$, intrinsic Si, and doped Si utilized in the calculations were obtained from previous studies[109, 110]. However, as the dielectric function of the $MgF_2$ film has a significant impact on our calculations, we directly measured its optical constants using a spectroscopic ellipsometer (IR-VASE Mark II). The optical properties of the $MgF_2$ film on a Si substrate were examined in the wavelength range of 1.7 to 33 µm (Figure 3-10a). Both $MgF_2$-coated Si samples and a bare Si sample (as a reference) were measured at incident angles of 55º

and 65°. The acquired optical properties of $MgF_2$ were then used in our theoretical calculations of $h_{RHT}$.

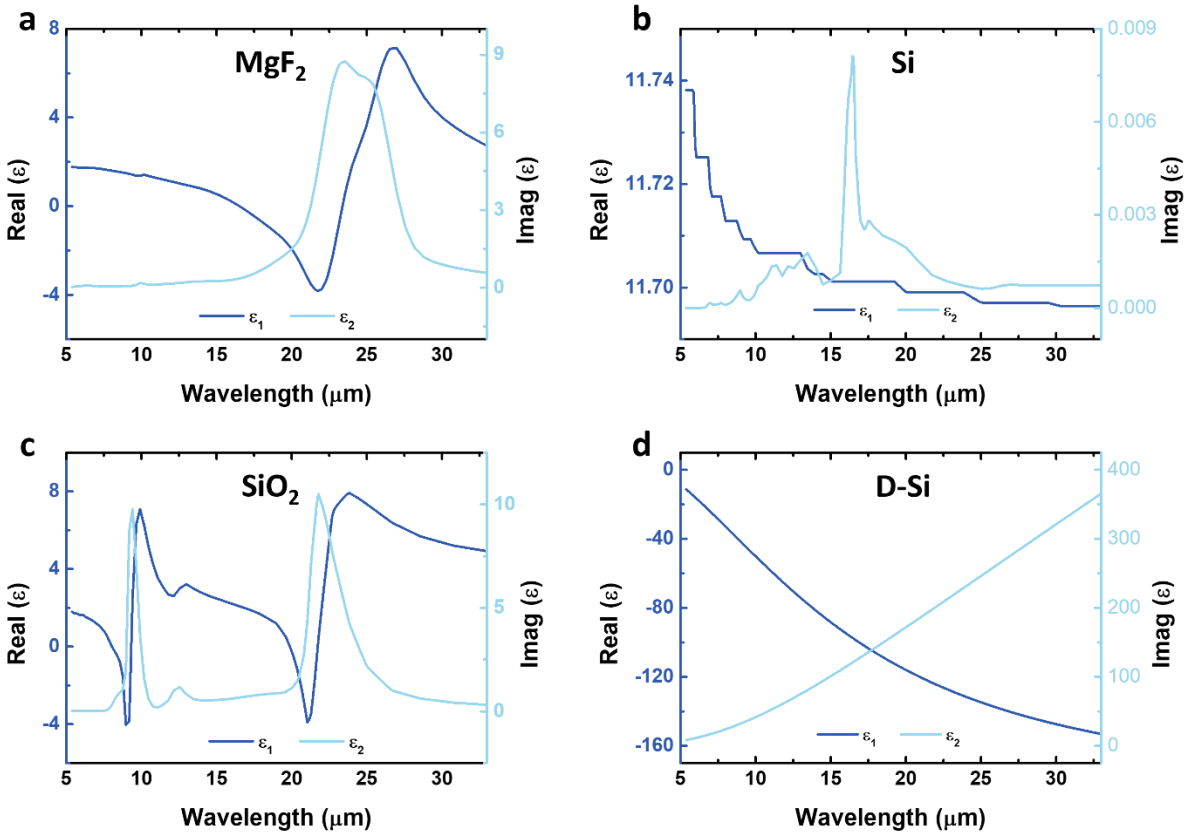


Figure 3-10. Dielectric properties of the films used for our calculations. (a) $MgF_2$, (b) intrinsic Si, (c) $SiO_2$, and (d) doped Si.

### *Analysis of NFRHT between unsupported dielectric films*

To better understand the influence of the Si substrate on which the $MgF_2$ films were deposited, we calculated NFRHT between unsupported thin films separated by vacuum gaps. In Figure 3-11, we plot the spectral energy transfer between suspended 50 nm-thick $MgF_2$ films. The solid lines correspond to gap sizes ranging from 50 nm to 500 nm. It is known that in suspended polar dielectric thin films, the SPhPs can split into antisymmetric and symmetric modes due to the coupling of modes at the two film surfaces[95, 98]. This is observed in our spectral calculations where

two peaks appear for gap sizes larger than the film thickness. For very small gaps, the spectra are similar to that of the bulk case due to the gap-dependent penetration depth. This is also seen in the transmission probability plots for different gap sizes in Figure 3-11b. At larger gap sizes, two separate modes are noticed that asymptotically approach the bulk case as the gap size becomes comparable to and smaller than the film thickness. Note that such feature of split modes is not observed in our calculations of supported films (Figure 3-4) potentially due to the presence of the underlying Si substrate.

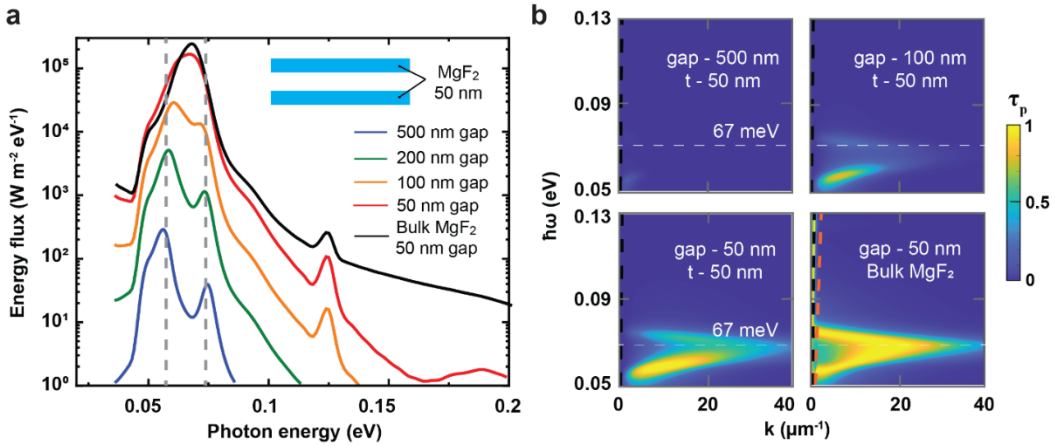


Figure 3-11. Spectral characteristics and transmission probabilities of *p*-polarized modes for suspended thin films. (a) Radiative energy flux as a function of photon energy for 50 nm-thick $MgF_2$ films for gaps ranging from 50 nm to 500 nm. The black curve represents the bulk case at a 50 nm gap. The inset illustrates the geometry. (b) Transmission probabilities for different film thicknesses and gap sizes. The black dashed line is the light line in vacuum. The white dashed line indicates the frequency at which Re($\varepsilon$) of $MgF_2$ is around -1, where SPhPs are strongly supported.

Note: This work is reproduced with permission from *ACS Photonics*. See reference [37]

Rohith Mittapally[†,*], ***Ju Won Lim***[†], Edgar Meyhofer*, Pramod Reddy*, and Bai Song*

(†These authors contributed equally to this paper)

# Chapter 4 Microwatt-Resolution Calorimeter for Studying the Reaction Thermodynamics of Nanomaterials at High Temperature and Pressure

## 4.1 Abstract

Calorimetry of reactions involving nanomaterials is of great current interest, but requires high-resolution heat flow measurements and long-term thermal stability. Such studies are especially challenging at elevated reaction pressures and temperatures. Here, we present an instrument for measuring the enthalpy of reactions between gas-phase reactants and milligram scale nanomaterial samples. This instrument can resolve the net change in the amount of gas-phase reactants due to surface reactions in an operating range from room temperature to 300 °C and reaction pressures of 10 mbar to 30 bar. The calorimetric resolution is shown to be <3 μW/√Hz, with a long-term stability <4 μW/hour. The performance of the instrument is demonstrated via a set of experiments involving $H_2$ absorption on Pd nanoparticles at various pressures and temperatures. For this specific reaction, we obtained a mass balance resolution of 0.1 μmol/√Hz. Results from these experiments are in good agreement with past studies establishing the feasibility of performing high resolution calorimetry on milligram scale nanomaterials, which can be employed in future studies probing catalysis, phase transformations, and thermochemical energy storage.

## 4.2 Introduction

Knowledge of the thermodynamics of surface reactions and phase transformations in nanomaterials is of crucial importance to heterogeneous catalysis, sustainable production of fuels and chemicals[111, 112], as well as hydrogen storage and fuel cell applications[113]. In particular, nanomaterials, such as noble metal nanoparticles, are excellent candidates for these applications, as they provide a high surface to volume ratio and low resistance to reactant mass diffusion[114]. Further, in the context of hydrogen storage for renewable energy and transportation applications, metal hydride nanoparticles are considered to be a promising platform, as they enable storage of large amounts of hydrogen in the interstitial sites of crystal lattices and feature rapid kinetics at room temperature[113].

Calorimetric reactors enable direct measurement of reaction thermodynamics and kinetics, and past work[115-119] has developed sensitive calorimeters to study surface reactions and catalysis. In Table 4-1, we summarize data from five representative studies, listing their operating range and main figures of merit. The instruments employ various temperature sensors, such as RTDs[115], thermocouples[116, 117], and pyroelectric heat detectors[118]. In addition, they use several techniques for quantifying the mass of gas-phase reactants, such as pressure–concentration measurements[115, 116], molecular beams with known fluxes of reactants[118], and gravimetric measurements using a microbalance[119]. Additionally, the specifications of two relevant, commercially available instruments are listed in Table 4-1. An important criterion for calorimetric measurements of chemical reactions is the amount of sample required for measurements. The amount and type of catalyst samples differ across previous studies: some use powdered samples, typically on the gram-scale[115-117], while others use either thin-film single crystals or dispersed samples[118, 119]. While the former group can achieve high temperature and pressure reaction conditions, the latter group is

limited to low pressures and operates close to room temperature, largely due to use of microfabricated devices, sensors incompatible with high pressure or temperature, or the need for operation under vacuum environment. In addition, the high temperature and pressure operation of the calorimeters utilizing powdered samples is impeded by poor long-term temperature stability and low heat flow resolution due to high effective thermal conductance of the calorimeter. Moreover, given that lab synthesis of novel catalysts and nanoparticles on the gram scale is often challenging, it is highly beneficial to develop calorimeter tools capable of accurate heat of reaction measurements with milligram scale samples, at high temperature and pressure conditions. Here, we present an instrument that addresses this need by enabling high heat flow resolution (<3 $\mu W/\sqrt{Hz}$) as well as long-term stability (<4 μW/hour) at temperature from 25 to 300 °C and reaction pressures of 10 mbar to 30 bar to resolve reaction energetics with high signal-to-noise ratio over a duration of several hours. This instrument has been tested over a duration of several days at up to 280 °C, and for durations of several hours at 300 °C.

Table 4-1. Comparison to relevant previously developed calorimetry instruments for the study of surface and catalytic reactions

| Study case | Typical sample size | P range | T range | Thermal time constant | T resolution | Power resolution | Long-term stability | Mass balance ability | Mass balance resolution |
|---|---|---|---|---|---|---|---|---|---|
| Ref.[115] | ~ 4 g | 0.1–200 bar | 100–600 °C | 90 s | $10^{-3}$ K/√Hz | $10^{-3}$ W/√Hz | <0.5 W/h | Yes | NA |
| Ref.[116] | ~ 1 g | 1–33 bar | RT–1300 °C | ~1800 s | <0.1 K/√Hz | 0.44 W/√Hz | <0.75 W/h | Yes | 0.02 mol |
| Ref.[117] | 0.4 g | 1–1.3 bar | RT | ~ 60 s | NA | NA | 0.007 K/hour | Yes | NA |
| Ref.[118] | 1µm films | $10^{-6}$ – $10^{-3}$ bar | -173 – +27 °C | 0.15 s | NA | ~$10^{-7}$ W | 1 mK/h | Yes | $8\times10^{-12}$ mol/cm$^2$ of sample |
| Ref.[119] | 10 µg | Vacuum –1 bar | RT–45 °C | NA | $10^{-4}$ K/√Hz | $10^{-6}$ W/√Hz | $10^{-6}$ W/h | Yes | 0.01 mol |
| TA Instruments Nano ITC | Volume 1.0 mL | NA | 2–80 °C | 13 s | NA | $10^{-7}$ W | <2 × $10^{-8}$ W/h | No | NA |
| Setaram C80 | Volume 12.5 mL | up to 1000 bar | Ambient to 300 °C | ~320 s* | 0.1 K/√Hz | $10^{-6}$ W | NA | Yes | NA |
| Current instrument | 1–5 mg | 10 mbar –30 bar | 22–300 °C | <75s @25°C, <30s @300°C | <$10^{-3}$ K/√Hz | < $3\times10^{-6}$ W/√Hz | <$4\times10^{-6}$ W/h | Yes | 0.1 µmol/√Hz |

* Calculated from heat release data in ref [120].

## 4.3 Experimental Procedures and Methods

### *Calorimeter Design*

The design of the calorimeter developed in this work is illustrated schematically in Figure 4-1. It consists of two thermal shields to minimize temperature fluctuations that were machined from copper and aluminum. A borosilicate glass capillary (inner diameter (ID) = 2 mm, outer diameter (OD) = 3 mm) is encapsulated by the shields. The capillary has an inward notch at the center of the capillary to hold a borosilicate sample holder (capsule) (see Figure 4-1b) where the reaction occurs. The volume enclosed by the outer shield is under a high vacuum (<7 μTorr), and its temperature is stabilized, via a feedback control loop, above room temperature (typically set to a temperature in the range of 23–36 °C) using two planar film heaters (see Figure 4-11). The outer shield is placed on four ceramic balls (see Figure 4-1a) to thermally isolate it from the environment and gas handling unit.

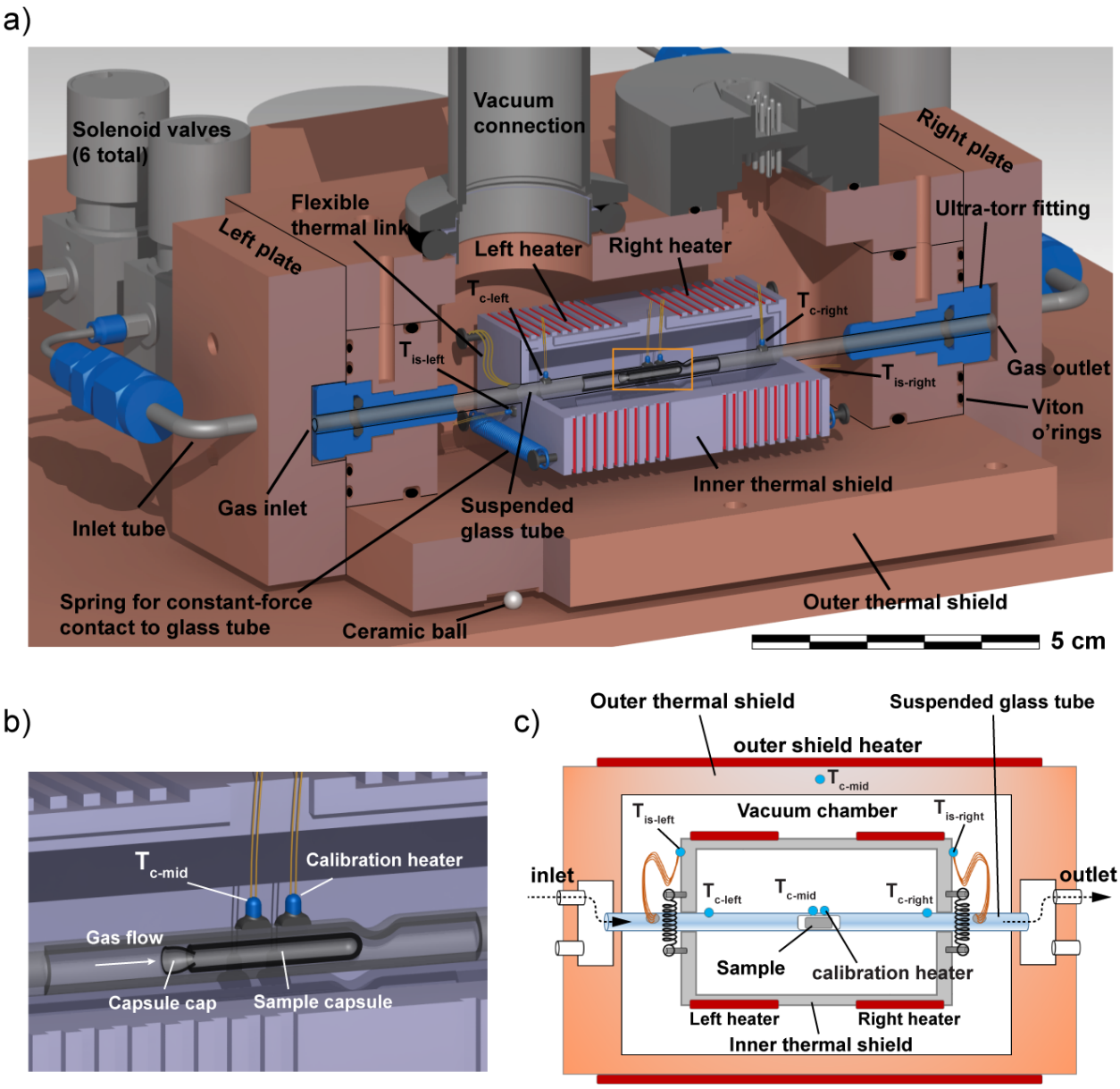


Figure 4-1. (a) Detailed cross-sectional view of the calorimeter showing the internal components along with a scale bar. The outer copper shield and the inner aluminum shield are shown. The suspended glass tube extends along the length of the calorimeter. The location of thermistors for temperature measurements are shown as small blue circles. Although not apparent from the drawing, the inlet tube and gas inlet are internally connected. (b) Zoomed-in view of the center of the glass tube and sample holder capsule assembly. (c) Schematic view of the calorimeter (not to scale).

The inner shield (shown in Figures 4-1a, c) covers the central part of the capillary tube, which is heated to the target reaction temperature (25–300 °C) using two resistive heaters made of NiChrome wire (AWG 38) (shown by red lines in Figure 4-1a), which cover the circumference of

the shield and uniformly heat the inner shield. A thin (50–100 μm) layer of a ceramic adhesive (Ted Pella, 16026) is applied underneath the NiChrome wire to provide electrical insulation from the aluminum inner shield. The inner shield is split in the middle and held together via two springs to compensate for the mismatch of radial thermal expansion between aluminum and the borosilicate tube at high temperatures.

The line contact between the inner shield halves and the tube surface results in a weak thermal link (i.e., low thermal conductance); therefore, fluctuations in the thermal conductance of this weak link have a relatively small impact on the temperature of the capillary tube. Nevertheless, a stable strong thermal link between the inner shield and the capillary tube is required to enable efficient heating of the central part of the capillary tube. This strong thermal link is achieved via flexible copper wires (fifteen AWG38 wires with a length of 20 mm were used on each side of the inner shield), which on one end are connected mechanically to the inner shield and on the other end soldered ultrasonically directly on the capillary tube as shown in Figure 4-1a. This method of thermal connection via flexible wires is robust and insensitive to thermal expansion; therefore, it provides high long-term thermal stability over a large number of operating cycles. During the development of this apparatus, we found that other thermal contacts, such as high-temperature ceramic epoxy (Ted Pella, 16026) and leaf springs inserted in the clearance between the inner shield and capillary tube, were not suitable. Their thermal conductance drifted excessively over time due to the mismatch in thermal expansion between the aluminum inner shield and the glass capillary tube.

The calorimeter temperature is monitored at six points using glass-encapsulated thermistors that are read out with Wheatstone bridges as described below. The temperature of the outer shield ($T_{os}$) is measured by a thermistor located 6 mm inside the bulk of the outer shield

(see Figure 4-11). The temperatures at the left ($T_{is\_left}$) and the right ($T_{is\_right}$) side of the inner shield are measured close to the contact points of the copper wires with the capillary tube (see Figures 4-1a, c). The temperature of the capillary tube is monitored at three different locations; left, right, and center of the capillary tube and are labeled $T_{c\text{-}left}$, $T_{c\text{-}right}$, and $T_{c\text{-}mid}$, respectively. The glass-encapsulated thermistors were connected to the capillary tube using ultrasonic glass soldering to minimize long-term changes in contact thermal conductance. At the center of the tube, an additional thermistor was installed to act as a dedicated heater (by Joule heating) and employed for calibration of the calorimeter as described below. The heat conduction via thermistor leads is minimized by using thin electrical connection wires (AWG 42 to AWG 50) that are >30 mm in length.

***Temperature Sensing Scheme***

Temperature sensing is performed using 1 MOhm glass-encapsulated thermistors (US Sensor GP105 V8J), which are read out as reported previously[121, 122]. In this scheme, the thermistor's resistance is measured via a full Wheatstone bridge (see Figure 4-2) driven by an AC voltage of 100 mV peak amplitude at 199 Hz sourced by an Agilent 33120 function generator. The output voltage of the bridge ($V_g$) is first amplified (40 dB) by an instrumentation amplifier (Analog Devices AD524ADZ), and then low pass filtered at a cutoff frequency of 220 Hz using a fourth-order Butterworth filter (Krohn-Hite 3384) and amplified by 10 dB, and is recorded using an analogue input DAQ channel (NI PCI-6014) at 19.9 kHz sampling rate. The signal amplitude and phase with respect to the excitation are synchronously measured, at the excitation frequency, using a LabView lock-in program. In addition, the effect of thermal drift is minimized by using electronic

components featuring very low temperature coefficients of resistance, such as Vishay's ultra-high-precision Z-foil resistors (Y145310K0000V9L).

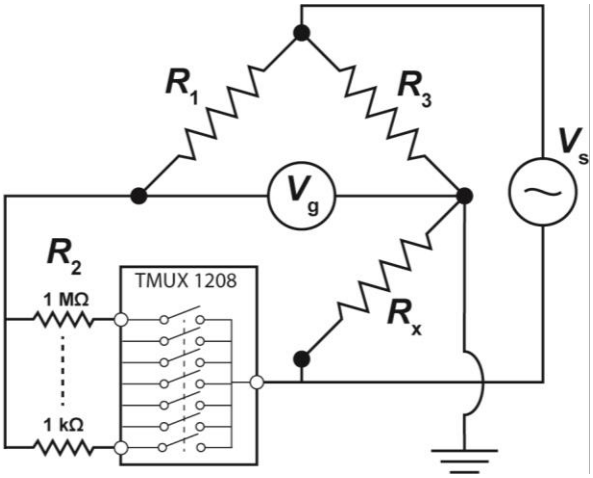


Figure 4-2. Wheatstone bridge circuit with switching balance resistor for readout of the thermistor resistance $R_x$. The bridge is driven via an AC voltage with amplitude of 100 mV at 199 Hz, and $V_g$ is recorded using a lock-in technique. The balance resistor $R_2$ is switched automatically using a look-up table at discrete values of resistance ranging from 1 MΩ to 1 kΩ to keep the bridge in range as the thermistor value $R_x$ changes in the operating temperature range of 25 to 300 °C. $R_1$ and $R_3$ have a constant value of 10 kΩ.

Since the measurement range for the capillary and inner shield thermistors spans from 25 to 300 °C, their electrical resistance changes accordingly from 1 MΩ to 0.5 kΩ (at 300 °C). This large variation of resistance significantly reduces the Wheatstone bridge sensitivity. Therefore, to achieve the desired sub-mK sensitivity in the entire operating range, the balance resistor ($R_2$) of the Wheatstone bridge (Figure 4-2) is actively varied using a resistor bank and a multiplexer (TMUX 1208) with eight resistors with values ranging from 1 MΩ to 1 kΩ so as to balance the Wheatstone bridge at all desired temperatures of operations. The upper resistors in the bridge, $R_1$ and $R_3$, have a constant value of 10 kΩ.

***Gas Handling Unit and Mass Balance Measurement Scheme***

The gas handling unit and the flow path for the gases into the calorimeter are shown in Figure 4-3. The gas handling unit consists of a prechamber, a capillary tube, and six miniature fast switching solenoid valves (Parker Hannifin, Series 99). In order to quantify the mass of the introduced gas, a pressure measurement scheme is used as described below.

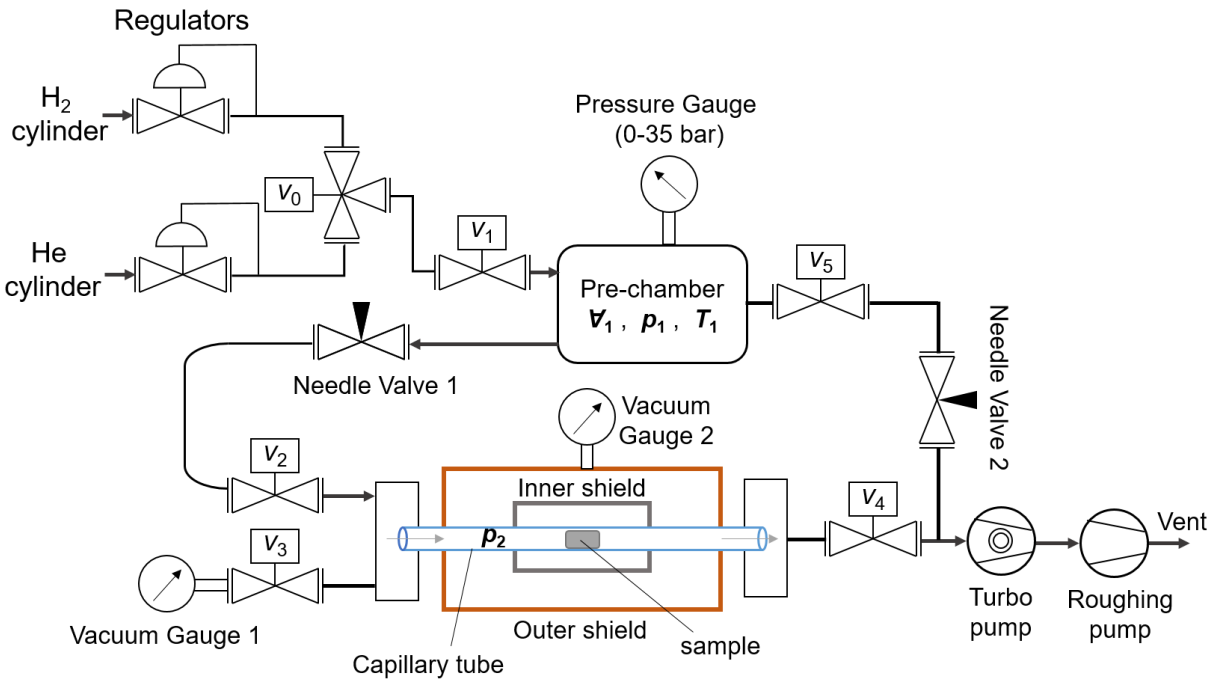


Figure 4-3. Gas handling unit and flow path of the calorimetric reactor. The valves $V_0$ to $V_5$ are miniature solenoid valves. During a hydrogen absorption experiment, the prechamber is loaded with the reactant gas to a desired pressure $p_1$; then this known amount of gas is introduced to the reaction tube while pressure recording provides a means for resolving the mass of absorbed gas on the sample.

Initially, the prechamber and capillary tube are pumped down to a low vacuum level (<10 mTorr) via a turbomolecular pump by opening valves 4 and 2 and keeping all other valves closed. The vacuum level can be measured using vacuum gauge 1 (MKS 925 Micro Pirani) when valve 3 is open. Prior to gas introduction, valve 3 is closed to isolate the large parasitic volume of this vacuum gauge from the rest of the calorimeter and prevent damage to the gauge at high pressures. Then, all other valves are closed for a short duration of a few seconds to prevent unwanted gas

introduction to the vacuum system when valve 1 is opened. When valve 1 is opened, a known volume (3.80 mL) of reactant gas, at the pressure set by the gas cylinder regulator, is first introduced into the prechamber. Then, the gas pressure in the prechamber is measured using a high accuracy pressure transducer (Omega PXM409–035BA10 V) with a range of 35 bar and is adjusted to the required set point by bleeding off excess pressure using valve 5. After the pressure and temperature are stabilized in the prechamber, the gas is expanded into the capillary by opening valve 2, during which the pressure $p_1$ (of the prechamber) is continuously recorded at a 20 Hz sampling rate. The needle metering valve (Swagelok SS-SS1), shown as the needle valve 1 in Figure 4-3, is incorporated to adjust the rate of gas introduction to the chamber, and is kept at a constant position during a set of experiments.

By knowing the exact gas volume, pressure, temperature, and composition before and after expansion, it is possible to calculate the amount of gas absorption ($\Delta n_{\text{absorbed}}$ [μmol]) based on the mass balance of a closed system using equation (4-1), where $\forall_1$ is the volume of prechamber, and $\forall_2$ is the sum of volumes of capillary tube, connection tubes, and parasitic volume of valves. In other words, $\forall_1$ is the volume of gas prior to expansion, and $\forall_1 + \forall_2$ is the volume of gas after expansion. Similarly, $\overline{\rho_1}$ and $\overline{\rho_2}$, the volume-averaged molar densities of gas before and after expansion, were obtained from the measured temperature and pressure of the gas and by linearly interpolation of the density data obtained from NIST thermophysical properties[123]. Calculation of $\overline{\rho_2}$ involves consideration of local densities due to the difference of temperature at various locations in the reaction tube calculated as $\overline{\rho_2} = \sum_i \rho_i V_i / \sum_i V_i$. We estimated the local gas temperature along the length of the capillary tube by linearly interpolating between the measured temperatures at the three sensors and calculated the gas absorption from

$$\Delta n_{absorbed} = n_1 - n_2 = \forall_1 \bar{\rho}_1 - (\forall_1 + \forall_2)\bar{\rho}_2 \quad (4\text{-}1)$$

The prechamber volume ($\forall_1$) was determined separately to be 3.80 mL by measuring the amount of water required to fill the prechamber. For accurate quantification of $\forall_2$, we used a baseline measurement using an empty sample capsule, where $\forall_2$ is calculated by setting $\Delta n_{absorbed} = 0$ in equation (4-1), and was found to be 2.79 ± 0.03 mL. The pressure sensing resolution is estimated to be 40 Pa/√Hz (approximated from a pressure measurement of a pressurized closed chamber under equilibrium) leading to a mass balance resolution better than 0.1 μmol in the entire operating range of the instrument. Figure 4-4 shows the pressure measurements during $H_2$ absorption in a baseline experiment for quantification of $\Delta n_{absorbed}$. The three steps in which the chamber is evacuated, gas is loaded into the prechamber, and reactant is introduced into capillary tube (labeled Vacuum, Prechamber loading, and Reactant introduction, respectively) are shown in Figure 4-4. We also showed in the inset (red vertical line) the drop in the equilibrium $H_2$ pressure with respect to the baseline after the introduction of $H_2$. This drop in pressure is due to absorption of $H_2$ on the sample and can be used to quantify $\Delta n_{absorbed}$.

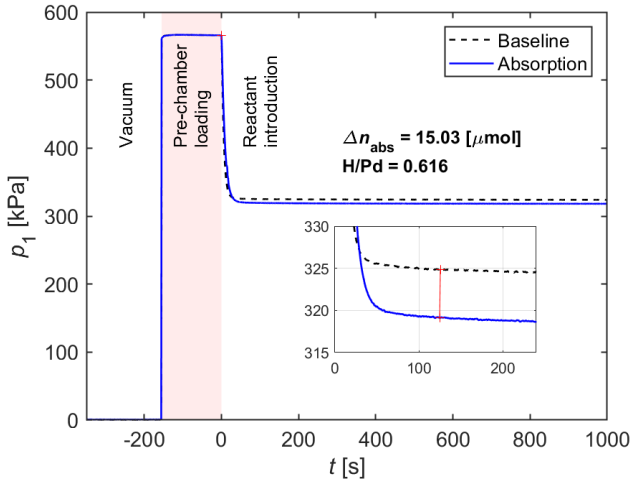


Figure 4-4. Measured prechamber pressure during gas introduction from the prechamber to the capillary for resolving the amount of absorbed gas, $\Delta n_{absorbed}$, and equilibrium H/Pd ratio. The dashed line shows a baseline experiment performed using an inert sample capsule with no material. The blue line shows a subsequent experiment with a Pd

nanopowder sample of mass 5.19 mg. The red line in the inset indicates the drop in the pressure trace due to absorption of gas on the solid sample.

## 4.4 Results and Analysis

### *Thermal model and characterization of the calorimeter*

A lumped thermal capacity heat transfer model[124] was developed to understand and predict the thermal response of the calorimeter. The physical parameters of the model, including thermal resistances and capacitances, were identified via calibration runs.

### *Lumped thermal capacity model*

In order to accurately interpret the results of experiments and convert the recorded values, such as temperature, pressure, and heating power, to quantities of interest (heat output in reactions), a lumped thermal capacity model of the system was developed. The equivalent thermal circuit of the lumped thermal capacity model is shown in Figure 4-5, where the central part of the capillary tube that includes the sample capsule as well as the two central thermistors (shown in Figure 4-1c) is abstracted as a node with lumped heat capacity $C_{\text{c-mid}}$, whereas $R_{\text{cl}}$ and $R_{\text{cr}}$ represent the thermal resistances from the aforementioned center node of the capillary to the left and right nodes and capture the effects of heat conduction through the borosilicate tube as well as the gas inside the tube. $R_{\text{os}}$ is the thermal resistance through the $T_{\text{c-mid}}$ thermistor and calibration heater lead wires to the outer shield. In addition, $R_{\text{isl}}$ and $R_{\text{isr}}$ are the thermal resistances between the $T_{\text{c-mid}}$ node and the left and right nodes of the inner shield, respectively. Since the space inside the outer and inner shields is kept at a high vacuum (<7 μTorr), $R_{\text{isl}}$ and $R_{\text{isr}}$ capture the effects of heat transfer via thermal radiation and become especially important at high temperatures. Finally, $\dot{q}_{\text{mid}}$ is the sum of all heat flows to the center node, which includes the heat

of reaction, heat transfer via the reactant gas, and heating by the calibration thermistor. Note that the heating by the measurement thermistor is negligible and was ignored. The transient behavior of this model can be described by a first-order ordinary differential equation, where the heat release rate at the center node ($\dot{q}_{\text{mid}}$) can be calculated using equation (4-2). Here, the first term indicates the heat flow due to conduction from multiple parallel paths with thermal resistances $R_{\text{i}}$ (as shown in Figure 4-5), and the second term indicates the transient heat flow due to variation in stored thermal energy in the central node.

$$\dot{q}_{\text{mid}} = \sum_{i} (T_{\text{c-mid}} - T_i)/R_i + C_{\text{c-mid}} \, {}^{dT_{\text{c-mid}}}/_{dt} \qquad (4\text{-}2)$$

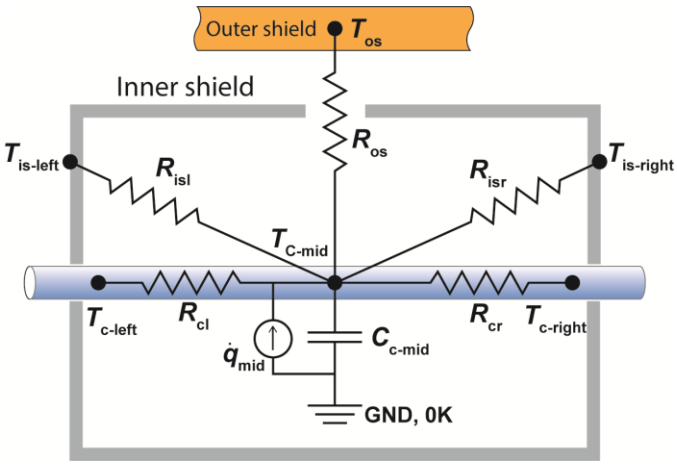


Figure 4-5. Lumped thermal capacity model. The center part of the capillary tube including the sample capsule and the sample, as well as the two thermistors mounted on this region, are lumped as a single thermal capacity of $C_{\text{c-mid}}$. Five thermal resistances are included which connect the center node to the capillary left/right, inner shield left/right, and outer shield.

### *Identification of thermal parameters and calibration runs*

The values of thermal resistances ($R$) and thermal capacitance ($C$) associated with the central node of the calorimeter are estimated by considering the material properties using simple heat conductance and capacitance relations shown in equations (4-3) and (4-4).

$$R = \frac{1}{G} = \frac{L}{A_{cross}\, k} \tag{4-3}$$

$$C = \sum_i m_i\, c_i \tag{4-4}$$

Here, $G$ is the thermal conductance, $L$, $A_{\text{cross}}$, and $k$ are the length, cross-sectional area, and thermal conductivity of a heat conduction path, respectively, and $m_i$ and $c_i$ are the mass and specific heat capacity (per mass) of the $i$th component of the lumped material in a thermal node. Temperature-dependent thermal conductivity data for borosilicate glass[125] and copper[126] were used to model the capillary's thermal conductance ($G_{\text{cl}}$ and $G_{\text{cr}}$) and the thermal conductance of copper wires connecting the central thermistors to the outer shield, respectively. The thermal conductance of gas in the glass tube was estimated using the pressure and temperature-dependent thermal conductivity of hydrogen[127]. The thermal conductance from the center node to the inner shield ($G_{\text{isl}}$ and $G_{\text{isr}}$) via radiation is estimated from equation (4-5):

$$G_{\text{radiation}} = 4\varepsilon\sigma A_1 F_{1\to 2} T_{c-mid}^3, \tag{4-5}$$

where $A_1$, ε, and $T_{\text{c-mid}}$ are the surface area, emissivity, and temperature of the center node, respectively, and σ is the Stefan–Boltzmann constant. In these calculations, a surface-averaged emissivity of 0.92 is assumed for borosilicate glass[128], and 0.1 for the solder[129] covering the glass surface along with a view factor ($F_{1\to 2}$) of unity, since the inner shield completely encloses the central part of capillary. The heat capacity of the central node was estimated from data for the heat capacity of borosilicate glass[130, 131]. The calculated parameters are shown as a function of the inner shield temperature in Figure 4-6. To confirm the validity of these estimates, we ran a set of calibration experiments and compared the measured total thermal conductance and thermal time constant with those predicted by our thermal model (Figure 4-5). The details of the calibration runs

are described in the next section. Finally, the aforementioned thermal parameters as well as the time series measurements of various temperatures $T_i$ are used in equation (4-2) to calculate the heat release rate from the central node ($\dot{q}_{mid}$).

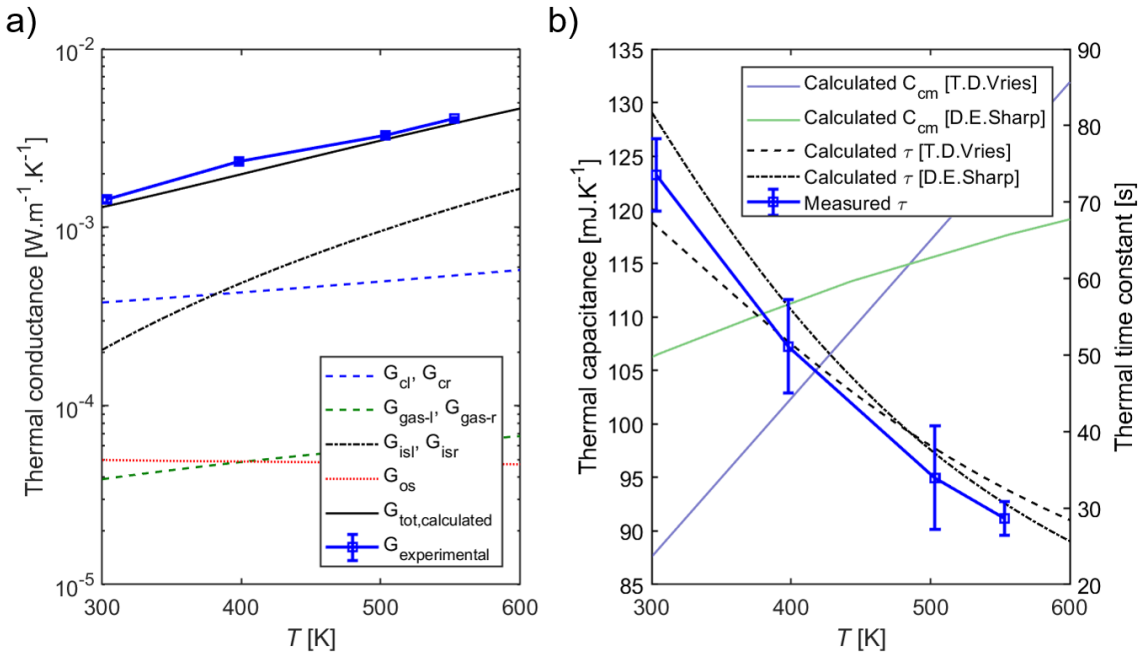


Figure 4-6. (a) Modeled thermal conductance values ($G_{cl}$, $G_{cr}$, $G_{isl}$, $G_{isr}$, and $G_{os}$ are the conductance values corresponding to Figure 4-5, $G_{gas-l}$ and $G_{gas-r}$ are the gas conductance of the left and right part of capillary, $G_{tot,calculated}$ is the sum of all the above conductances) and the measured total effective thermal conductance of the calorimeter ($G_{experimental}$). (b) Modeled thermal capacitance ($C_{cm}$) and the thermal time constant ($\tau$) along with the measured thermal time constant of the calorimeter. The modeled capacitance is calculated using two different relations for heat capacity of borosilicate glass obtained from refs[130, 131].

***Temperature stability and calorimeter resolution***

The outer shield temperature was feedback-controlled using a PID controller with a bandwidth of 1 Hz, which was sufficient to maintain, depending on operating conditions, a target temperature of 23–36 °C with <5 mK RMS temperature variation during the entire experiment. The inner shield temperature is controlled via two feedback loops for the left and right parts of the inner shield running at 10 Hz (see details of controller tuning and temperature stability in Figure 4-12). The measured temperature stability of the capillary located inside the inner shield is shown

in Figure 4-7, where, during the first hour of the experiment, the capillary tube is under vacuum and has a temperature stability of better than 1 mK. At time $t$ = 1 h, the reactant gas ($H_2$) is introduced into the capillary tube leading to perturbation of $T_{c\text{-left}}$ and $T_{c\text{-right}}$, which settle back to mK stability within 15 min of reactant introduction.

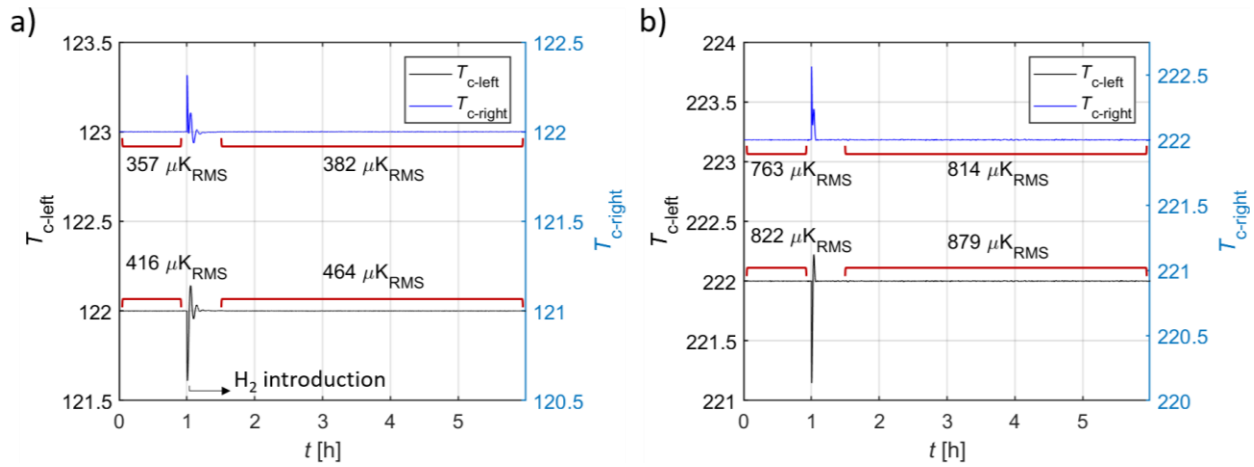


Figure 4-7. Stability of the inner shield temperature controller during the introduction of reactants to the capillary tube at set points of (a) 122 °C and (b) 222 °C. The reactant gas ($H_2$ here) is introduced at $t$ = 1 h, perturbing $T_{c\text{-left}}$ and $T_{c\text{-right}}$ temperatures. The temperatures settle back to mK stability within 15 min after introduction. The RMS temperature variation in a 1 Hz bandwidth is shown for two-time intervals before and after gas introduction (0–0.9 h and 1.5–6 h).

To characterize the calorimeter resolution, as well as the effective calorimeter conductance, the temperatures of the outer and inner shields are feedback-controlled at constant values, and pulses of heat of increasing amplitude are deposited at the center node ($T_{c\text{-mid}}$) of the calorimeter using the calibration thermistor as a Joule heater. This test was repeated at different temperatures with the capillary tube being either under vacuum or filled with $H_2$ at different pressure levels. Figure 4-8 shows the results of calorimeter characterization experiments at $T_{c\text{-mid}}$ values of 30 and 230 °C. The transient response of the calorimeter to heat flow pulses (shown in Figure 4-8a, c) is used to extract the thermal time constant (i.e., the rise time to a temperature equal to $(1 - e^{-1}) \times \Delta T_{steady}$)[124]. In addition, the total conductance of the center node ($T_{c\text{-mid}}$) to the surrounding

nodes is obtained by a linear fit to the temperature rise as a function of power input (see Figure 4-8b, d). For instance, in Figure 4-8b, total thermal conductance of 1.485 and 1.523 mW/K are obtained under vacuum conditions and when filled with $H_2$ under 7.0 bar of pressure, respectively, at 30 °C. The slight increase in thermal conductance in the latter case is due to the contribution arising from $H_2$. In addition, a heat flow resolution of 0.51 and 2.41 μW/√Hz is observed at 30 and 230 °C, respectively. The decrease in calorimetric resolution at higher temperatures is due to (i) a decrease in inner shield temperature stability and (ii) a decrease in thermistor resistance leading to a lower signal-to-noise ratio as discussed in more detail below.

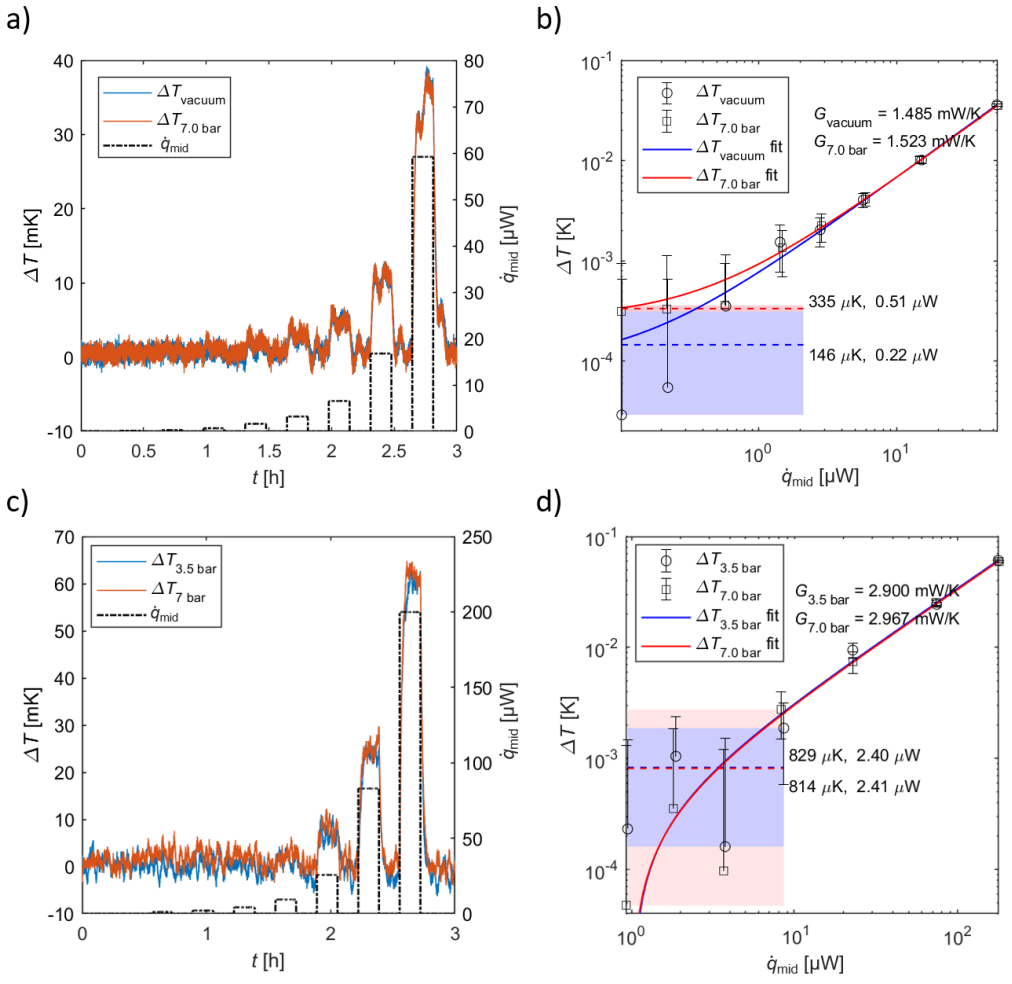


Figure 4-8. Characterization of calorimeter at two different temperatures ($T_{c\text{-}mid}$) with values of (a,b) 30 °C and (c,d) 230 °C, respectively. Each experiment is repeated at two different $H_2$ pressures. Panels (a) and (c) show the transient response of the calorimeter to step inputs to heat flow ($\dot{q}_{mid}$) with ~1 Hz sampling frequency. Panels (b) and (d) show

the steady temperature rise as a function of heat flow input, where the effective thermal conductance and the heat flow resolution of the calorimeter are obtained.

### *Characterization of hydrogenation of Pd nanoparticles*

In order to demonstrate the utility of our calorimeter, we probed the hydrogenation of palladium (Pd) nanoparticles. In this reaction, hydrogen gas is absorbed on Pd particles, and it is expected[132] that depending on the concentration of H in the Pd lattice either a low concentration α-phase, a high concentration β-phase, or a supercritical palladium hydride ($PdH_x$) is formed. The sample in our experiments was composed of commercially available Pd nanoparticles with a mean diameter of 15 nm (US Research Nanomaterials Inc., Pd 99.95%; see Figure 4-13 for sample characterization). Experiments at two pressure levels, 3 and 7 bar-absolute, and three temperature levels of 30, 125, and 230 °C were conducted.

The experiments were performed on seven different samples of identical Pd nanoparticles. As some of the samples were tested multiple times, it is important to consider the issue of hysteresis in hydrogen absorption/desorption. To minimize the effect of hysteresis, prior to each absorption experiment, the sample was pretreated under vacuum (<10 mTorr) and at high temperature (>150 °C) for a duration of at least 2 h. Based on past work[132, 133] on hydrogenation of Pd nanoparticles, at such low pressures and high temperatures, it is expected that absorbed hydrogen is mostly desorbed and the absorption and desorption curves overlap. In addition, based on past work[120, 134], the aforementioned preheating step is required for removing a substantial portion of absorbed oxygen and water from the samples. For full oxygen removal from the Pd nanoparticles, the samples need to be reduced under a hydrogen environment; however, we have avoided this reduction step during the sample pretreatment in order to be able to conduct a measurement on the enthalpy of the reaction during the first exposure of the sample to $H_2$, as well as subsequent

exposures to $H_2$ during the repeats of the measurement. The detailed experimental conditions for these measurements are summarized in Table 4-2.

Table 4-2. Experimental steps employed for the measurement of the hydrogenation enthalpy of Pd nanoparticles

| | **Experimental Step** | **Duration** |
|---|---|---|
| 1 | Temperature ramp from 30 °C to 150 °C | 65 min |
| 2 | Pretreatment under vacuum | 120 min |
| 3 | Ramp to target temperature | - |
| 4 | Stabilize inner & outer shield temperatures | 120 - 240 min |
| 5 | Pre-chamber gas introduction | 30 s |
| 6 | Stabilize pre-chamber pressure | 2 min |
| 7 | Gas introduction to the capillary tube | ~ 20 s |
| 8 | Measurement of thermal response | 300 min |
| 9 | Calibration run: heat flow step input sequence to capillary center | 160 min |
| 10 | Vacuum | 60 min |

***Baseline measurement for reaction calorimetry***

Along with the introduction of gas-phase reactants into the calorimeter, a number of effects need to be considered to prevent artifacts in the measurement of the heat of reaction. These effects include

(a) Cooling of reaction tube due to introduction of reactant gases at a lower temperature, as well as the Joule-Thomson effect due to expansion of the gas from the prechamber to the reactor capillary.

(b) The aforementioned cooling of the reaction tube imposes an additional transient thermal load on the heaters, which can disturb the closed-loop temperature controller of the inner shield and temporarily perturb the temperature of different parts of the inner shield as shown in Figure 4-7.

(c) Introduction of gas into the capillary tube results in a change of its conductance which in turn leads to variations of the thermal resistance network and changes the steady-state temperature of the capillary center ($T_{\text{c-mid}}$), despite all other inner/outer shield temperatures maintained at constant values.

In order to eliminate the effects of the aforementioned artifacts, a baseline experiment was performed prior to each reaction experiment with operating conditions identical to those of the actual reaction experiment, i.e., identical sequence and timing of valve operation, gas introduction, and temperature set points. The baseline experiment can in principle be done using one of the following two approaches

1. Using an empty sample capsule or using a non-reacting and non-absorbing sample.

2. Using an inert gas with similar thermal properties as the main reactant.

Below, we describe the results obtained using the first approach.

***Enthalpy of hydrogenation of Pd nanoparticles***

To evaluate the performance of the calorimeter, we performed a series of experiments and characterized the hydrogenation of small samples of Pd nanoparticles (mass ranging from 3.77 to 5.28 mg). Some examples of the absorption measurements at a hydrogen pressure of 7 bar are shown in Figure 4-9 (results at 3 bar are shown in Figure 4-14). As stated above, for all experiments, we first conducted a baseline measurement using an empty sample holder. In all these figures, a time span of 6 h is shown, where initially the reaction capillary tube is under vacuum in the temperature stabilization step (step 4 in Table 4-2). Then, the chamber is pressurized (steps 5 and 6 in Table 4-2) and the reactant ($H_2$) at a specified pressure is introduced into the reaction tube at $t$ = 1 h (step 7 in Table 4-2). Although the heat output associated with the hydrogenation reaction returns to undetectably low levels 10 to 20 min after the start of the reaction, the experiments were continued for 5 h in order to establish the long-term thermal stability of the calorimeter. Panels (a), (c), and (e) in Figure 4-9 show the temperature rise ($\Delta T$) of the capillary center obtained by subtracting from the measured midpoint temperature ($T_{\text{c-mid}}$), the expected temperature of the midpoint ($T_{\text{c-mid, expected}}$) in the absence of heat generation in the capillary tube. The resistance network shown in Figure 4-2 can be employed to obtain the expression shown in equation (4-6) for evaluating $T_{\text{c-mid,expected}}$.

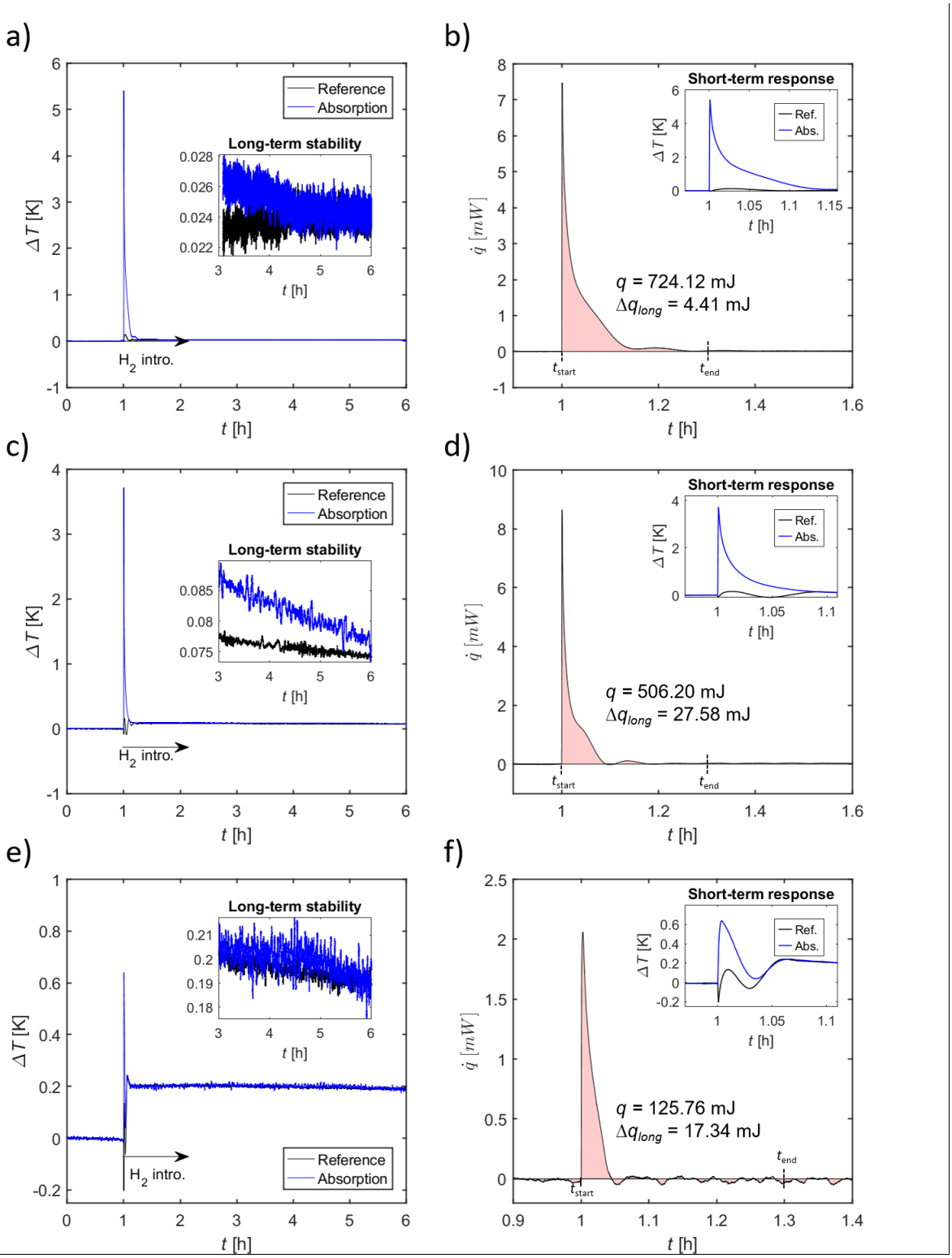


Figure 4-9. Experimental measurements of the temperature rise and heat release rate associated with absorption of $H_2$ on Pd samples. Data were obtained following the protocol described in Table 4-2 at an absolute pressure of 7 bar at various temperatures of 30 °C for (a) and (b), 125 °C for (c) and (d), and 230 °C for (e) and (f). Panels (a), (c), and (e) show the recorded $\Delta T$ of the baseline experiment with an empty sample holder, as well as the absorption experiment using the Pd sample. The capillary reaction tube is initially under vacuum, and at time $t$ = 1 h, hydrogen is introduced to the reaction tube, resulting in an exothermic reaction and a transient heat output signal shown in panels (b), (d), and

(f). The heat of reaction, $q$, was obtained by integrating the heat flow between $t$ = 1 and 1.3 h. $\Delta q_{long}$ is a measure of the long-term stability, which is the maximum cumulative heat release from $t$ = 5 to 6 h. The insets in (a), (c), and (e) show the long-term response, and the insets in (b), (d), and (f) show the short-term response. The mass of the Pd sample was 5.10 mg, 3.89 mg, and 3.77 mg for the reaction a 30, 125, and 230 °C, respectively.

$$\Delta T = T_{\mathrm{c-mid}} - T_{\mathrm{c-mid,expected}}, \text{ where}$$

$$T_{\mathrm{c-mid,expected}} = R_{\mathrm{tot}} \sum_i {T_i}/{R_i}\ , \text{ and } \quad R_{\mathrm{tot}} = \left( \sum_i {R_i}^{-1} \right)^{-1} \tag{4-6}$$

It can be seen that $\Delta T$ is steady for the entire 1 h (offset to zero in the plot) prior to the addition of hydrogen. Following the addition of hydrogen, the reaction is rapidly initiated and a transient reaction lasting for ~0.3 h is observed. Following this initial hydrogen absorption reaction, the calorimetric heat signatures settle to a new steady-state value. This offset relative to the pre-hydrogen incubation level (~25 mK at 30 °C, up to ~200 mK at 230 °C) is due to a change in thermal conductance of the capillary tube, which effectively changes the steady-state value of $T_{c\text{-}mid}$ at thermal equilibrium and is discussed in the previous section. This offset is well captured by the baseline experiment, eliminating a possible misinterpretation of "continuous" heat generation. Other transient artifacts which could occur in the first few minutes after reactant introduction, due to heat transfer to the reactant gas and temperature controller disturbance (as described in the previous section), are also eliminated by the baseline experiment.

In order to obtain the heat generation rate at the capillary center due to chemical reactions, we subtract the net heat release rate (estimated using equation 4-2) of the baseline from the absorption experiment ($\dot{q}_{rnx} = \dot{q}_{absorption} - \dot{q}_{baseline}$), as shown in panels (b), (d), and (f) of Figure 4-9. Inspection of the heat release plots reveals up to three features, depending on the reaction temperature. (i) All heat release plots show a sharp positive peak following the introduction of hydrogen ($t$ = 1 h) with a full width (duration) at half-maximum of less than 1 min at all

temperatures, which is limited by the calorimeter's response time. This sharp peak is attributable to the initial step of hydrogenation, which is the dissociative chemisorption of $H_2$ molecules on the surface of Pd and is highly exothermic. Because of the low activation energy[120] of hydrogenation, the initial heat generation does not show a large temperature dependence and occurs faster than the thermal response of the calorimeter at all reaction temperatures. (ii) Following the initial saturation of chemisorbed hydrogen on the surface, the net heat release curves show a small shoulder (i.e., a significantly smaller secondary peak), which we attribute to two possible processes: Hydrogen uptake by a subsurface layer of Pd[135] and subsequent diffusion to bulk Pd for forming α-phase hydride[120]. Both these steps are moderately exothermic and based on previous reports have activation energies of (∼29 and 25 kJ/mol-$H_2$)[135, 136] due to which they exhibit temperature-dependent rates. The duration of this step is about 6 min at 30 °C, decreasing to 2 min at 230 °C. (iii) An additional broad feature after 1.15 to 1.2 h is seen in the recordings at 30 and 125 °C, which requires further studies to elucidate its origin, but can possibly be related to further bulk diffusion of hydrogen or to the formation of β-phase of Pd-hydride, which is expected to occur on comparable time scales based on past work on α → β phase transformation kinetics[137].

It should be noted that, upon successfully incorporating the effect of the offset in $\Delta T$ via the baseline experiment, the heat release rate is seen to be close to zero ∼0.3 h after $H_2$ introduction in all experiments. Therefore, we use the integral of heat release rate from $t_{start}$ = 1 h (start of reaction) to $t_{end}$ = 1.3 h to obtain the heat of reaction ($q$) listed in panels (b), (d), and (f) of Figure 4-9. To obtain a bound on the long-term thermal stability of the instrument, we calculated the maximum deviation of cumulative heat release rate from zero in the period from $t$ = 5 h to $t$ = 6 h, which is listed as $\Delta q_{long}$ in the plots. As can be seen, the long-term uncertainty values are small

compared to the heat of hydrogenation during a 5-hour-long experiment, indicating that the instrument can readily resolve the heat of reaction over several hours.

The results from these experiments, along with some repeats, are listed in Table 4-3. The second column shows the sample label for the experiments. The samples are all taken from a single batch of Pd nanoparticles; therefore, on average their properties are expected to be identical. The third and fourth columns list the mean reaction temperature during measurement and equilibrium hydrogen pressure after its introduction into the capillary tube, respectively. The main results are the changes in internal energy ($\Delta U$) and enthalpy ($\Delta H$) of hydrogenation calculated using equations (4-7) and (4-8), and the equilibrium atomic ratio of hydrogen to palladium (H/Pd). In equation 4-8, the $V\Delta p$ term is the heat of compression, where $V = \forall_1 + \forall_2 = 6.59$ mL is the total volume of the gas after introduction to the capillary, and $\Delta p$ is the pressure change as a result of reaction. The contribution of $V\Delta p$ is relatively small in our system, e.g., at 30 °C and 7 bar, $V\Delta p$ = 6.59 mL × (−7.52 kPa) = −49.58 mJ compared to the heat of reaction of $q$ = 724.12 mJ. The measurements at 30 °C and 3 bar are repeated twice, with and without preheating a fresh sample at 150 °C. The experiment with a fresh sample without preheating shows a much larger enthalpy of hydrogenation, which we believe is due to oxidation of hydrogen by the residual oxygen on the sample. Based on past work[120, 134], preheating a fresh sample under vacuum is necessary to desorb residual oxygen and water and obtain metallic Pd prior to hydrogen introduction.

Table 4-3. Summary of the measurements of the reaction calorimetry on hydrogenation of Pd nanoparticles. To estimate the error on enthalpy ($\Delta H$), the maximum error of heat of reaction ($q$) is normalized by the amount of absorbed reactant (mol-$H_2$)

| Test | Sample label | $T_{rxn}$ | $p_{rxn}$ | $m_{pd}$ | $q$ | max $q$ error | H/Pd | $\Delta H$ | Max $\Delta H$ error | comment |
|---|---|---|---|---|---|---|---|---|---|---|
| # | - | °C | bar | mg | mJ | mJ | - | kJ/mol-$H_2$ | kJ/mol-$H_2$ | |
| 1 | A | 30.27 | 3.12 | 5.28 | 707.58 | 2.74 | 0.752 | -36.07 | 0.15 | 1st absorption |
| 2 | A | 30.23 | 3.12 | 5.28 | 535.49 | 6.47 | 0.725 | -27.30 | 0.36 | 2nd absorption |
| 3 | B | 30.29 | 3.11 | 5.45 | 2075.62 | 31.67 | 0.881 | -89.51 | 1.40 | no pre-heating |
| 4 | C | 30.23 | 7.06 | 5.10 | 724.12 | 4.41 | 0.830 | -33.93 | 0.22 | 1st absorption |
| 5 | D | 124.94 | 3.27 | 4.77 | 779.79 | 24.92 | 0.683 | -47.21 | 1.51 | 1st absorption |
| 6 | E | 125.00 | 3.22 | 5.61 | 727.57 | 37.72 | 0.725 | -44.75 | 2.32 | 1st absorption |
| 7 | F | 125.43 | 3.57 | 3.89 | 610.14 | 22.63 | 0.681 | -46.54 | 1.82 | 1st absorption |
| 8 | F | 125.36 | 6.90 | 3.89 | 506.20 | 27.58 | 0.747 | -34.59 | 2.02 | 2nd absorption |
| 9 | F | 125.34 | 6.88 | 3.89 | 504.73 | 26.52 | 0.763 | -33.69 | 1.90 | 3rd absorption |
| 10 | F | 125.32 | 3.27 | 3.89 | 477.24 | 20.61 | 0.662 | -36.96 | 1.70 | 4th absorption |
| 11 | G | 230.10 | 6.85 | 3.77 | 125.76 | 17.34 | 0.229 | -28.48 | 4.27 | 2nd absorption |
| 12 | G | 230.09 | 6.86 | 3.77 | 130.59 | 12.59 | 0.231 | -29.43 | 3.08 | 3rd absorption |
| 13 | G | 230.11 | 7.09 | 3.77 | 95.19 | 22.39 | 0.179 | -27.44 | 7.04 | 4th absorption |
| 14 | G | 230.12 | 3.31 | 3.77 | 42.73 | 30.87 | 0.068 | -33.11 | 25.73 | 5th absorption |
| 15 | G | 230.17 | 3.27 | 3.77 | 54.95 | 7.05 | 0.100 | -28.55 | 3.98 | 6th absorption |

In order to check the accuracy of the instrument and analysis procedure, we repeated the experiment at 125 °C and 3 bar three times on different Pd samples (tests 5–7 listed in Table 4-3). The results indicate closely clustered enthalpies of hydrogenation for the three repeats with a standard deviation of 2.75%. This relatively small variation observed may be attributed to sample-to-sample variation of the equilibrium H:Pd ratio[132] and variation in the equilibrium $H_2$ pressure.

$$\Delta U = q = \frac{1}{\Delta n_{absorbed}} \int_{t_{start}}^{t_{end}} \left(\dot{q}_{absorption} - \dot{q}_{baseline}\right) dt \quad (4\text{-}7)$$

$$\Delta H = \frac{1}{\Delta n_{absorbed}} \left( \int_{t_{start}}^{t_{end}} \left(\dot{q}_{absorption} - \dot{q}_{baseline}\right) dt + V\Delta p \right) \quad (4\text{-}8)$$

Figure 4-10a shows the internal energy of hydrogenation of Pd nanoparticles, per unit mass of Pd as a function of the equilibrium H/Pd ratio. It can be seen that these data show a linear pattern, and are in good agreement with previous measurements on bulk Pd[138]. Figure 4-10b shows the enthalpy of hydrogenation per mole of adsorbed $H_2$, which spans a range from −33.44 to −41.94 kJ/mol-$H_2$. This value is also in agreement with previous studies that mostly rely upon indirect measurement of the enthalpy of hydrogenation using an isotherm method and Van't Hoff's relation, clustered within −28 to −40 kJ/mol-$H_2$ depending on Pd particle size and measurement technique[132, 133, 139, 140]. The results are also in agreement with past calorimetric measurements, which report a wide range for the enthalpy of hydrogenation of Pd (−32 to ∼−60 kJ/mol-$H_2$)[117, 120, 141]. In Figure 4-10b, the enthalpy of hydrogenation shows no significant trend as a function of temperature; however, a decrease in the absolute value of enthalpy of hydrogenation with the reaction pressure is observed. This effect can be explained based on the variation of equilibrium H/Pd ratio as a function of reaction pressure, where some previous studies have reported that the enthalpy of hydrogenation is higher at lower H/Pd ratios as a result of highly exothermic dissociative chemisorption of $H_2$ molecules on the Pd surface[120, 138].

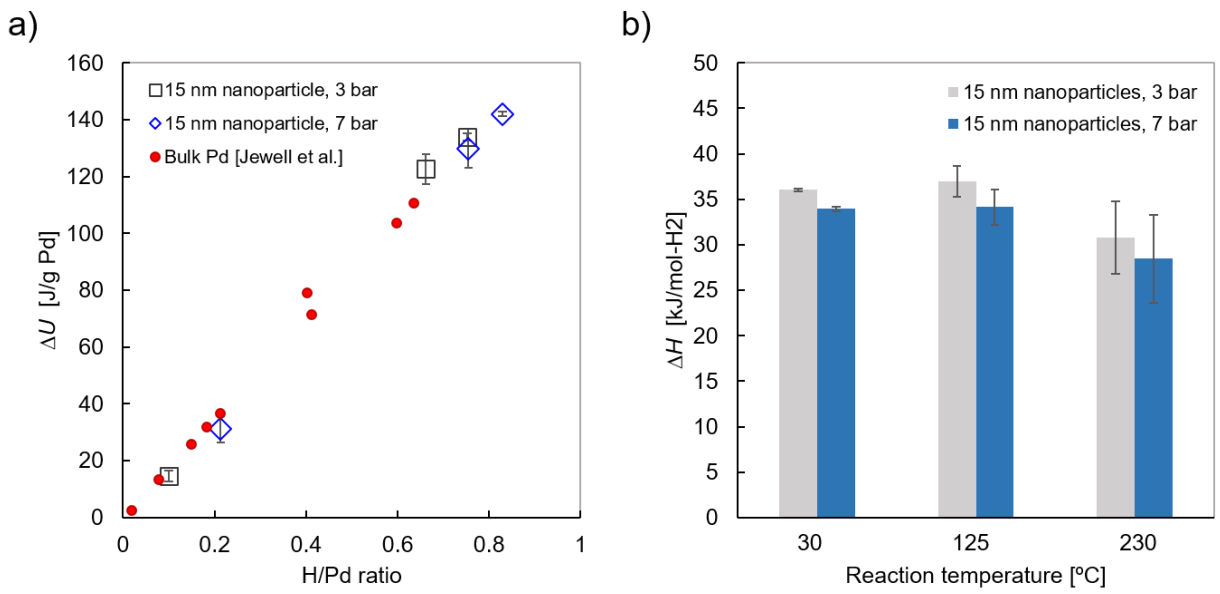


Figure 4-10. Internal energy and enthalpy of hydrogen absorption in Pd nanomaterials. (a) Internal energy change per unit mass of Pd samples. Red dots show previous measurements on bulk Pd adapted with permission from ref[138]. Copyright 2006 Elsevier. (b) Enthalpy of reaction per mole of absorbed $H_2$ at three reaction temperatures and two pressure levels. Error bars are estimated from the maximum long-term stability.

In terms of the equilibrium phase of the Pd hydride, it can be seen that all the measurements at 230 °C (503 K) demonstrate a low equilibrium hydrogen concentration of H/Pd < 0.23 after the reaction. Based on previous calculations and measurements on Pd nanoparticles, this low concentration indicates either an α-phase or a supercritical palladium hydride phase[132, 142]. On the other hand, measurements at 30 and 125 °C show a higher hydrogen concentration of H/Pd > 0.66 which indicates a $\beta$-phase of palladium hydride (see the phase diagram of $PdH_x$ nanoparticles in Figure 4-15).

## 4.5 Conclusion

We present a calorimetric reactor for measuring the heat of chemical reactions between a gas-phase reactant and milligram-scale solid-phase samples. The instrument can also be used to quantify the amount of absorbed reactants on the sample using a pressure–concentration

measurement technique with a resolution of 0.1 μmol/√Hz. The instrument is particularly useful for studying nanomaterial samples, given that typical laboratory synthesis of nanomaterials yields milligram-scale samples. The operating range of this instrument is from room temperature to 300 °C, and 10 mbar to 30 bar. In order to accurately interpret the results of the calorimetry, a one-state lumped-thermal capacity heat transfer model was developed with pressure and temperature-dependent thermal conductance and temperature-dependent heat capacitance. The instrument parameters such as total thermal conductance and thermal capacitance are calibrated using an electrical heater installed at the sample location. The heat flow resolution was demonstrated to be better than 3 μW/√Hz in the entire operating range, which was validated via a set of $H_2$ absorption experiments on Pd nanoparticles with a sample mass in the 3–5 mg range and performed at two pressure levels (3, 7 bar), and three temperatures (30, 125, and 230 °C). The results agree with previously reported values of the enthalpy of hydrogenation of Pd and the equilibrium H/Pd ratio. The advances presented here enable high-resolution calorimetry for the measurement of thermodynamics and kinetics of chemical processes on nanomaterials, including catalytic reactions, phase transformations, and thermochemical energy storage using metal hydrides.

## 4.6 Supplementary Materials

### *Temperature control of outer and inner shields*

To achieve high calorimetric resolution the temperature of the thermal shields must be maintained at a steady value. To achieve this, the outer shield temperature was measured using a glass-encapsulated thermistor located 6 mm inside the bulk of the side wall of the outer shield as shown in Figure 4-11, and heated using two planar film heaters (Omega Polyimide Film insulated heaters, 1" by 5", power = 2.5 W/in$^2$). This temperature was feedback-controlled using a PID controller (1 Hz bandwidth) with gains tuned using the Ziegler-Nichols method[143]. This controller

was sufficient to maintain the temperature at a target of 23-36 °C (depending on operating conditions) with better than 5 $mK_{RMS}$ stability. As an example, the stability of $T_{os}$ during an $H_2$ absorption experiment is shown in Figure 4-12 at a setpoint of 23.2 °C.

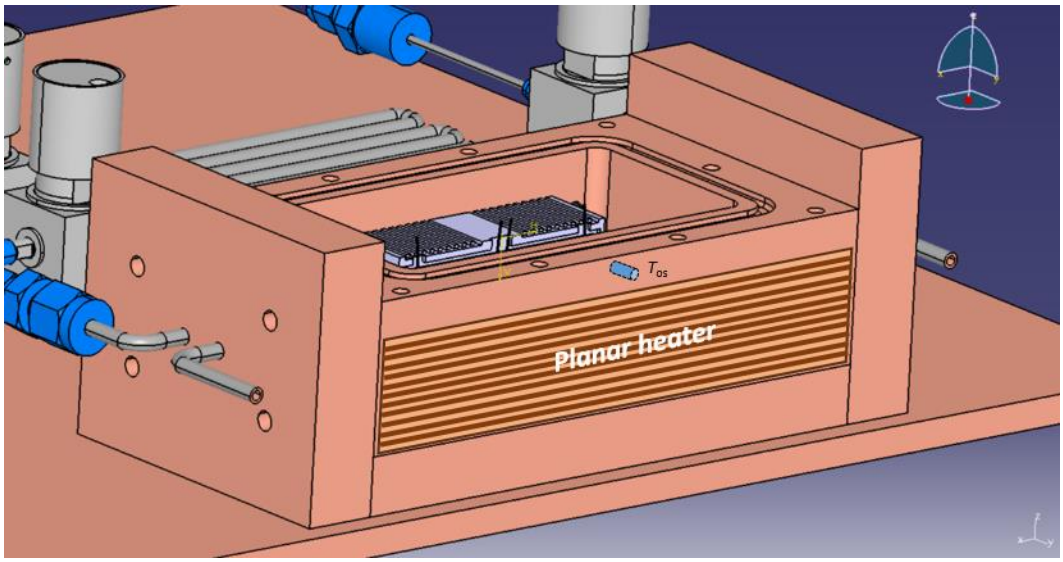


Figure 4-11. Location of the $T_{os}$ thermistor and a planar film heater on the outer shield.

The control of the inner shield temperature is more challenging specifically at higher temperature setpoints due to increased thermal coupling of the inner and outer shield, which increases the disturbance on the inner shield. In addition, the thermal time constant of the inner shield is ~600 s which is significantly smaller than that of the outer shield. The combination of these effects required a relatively high controller bandwidth of 10 Hz to reduce the temperature error band to the desired sub-mK level[144]. In addition, the significant variation in thermal conductance and thermal time constant of the inner shield as a function of temperature makes the thermal system a non-linear plant, which was controlled using a gain-scheduled PID controller where the gains vary as a function of reaction temperature[145]. The stability of the capillary left and

right ($T_{c\text{-left}}$ and $T_{c\text{-right}}$) temperatures during an $H_2$ absorption experiment are shown in Figure 4-12.

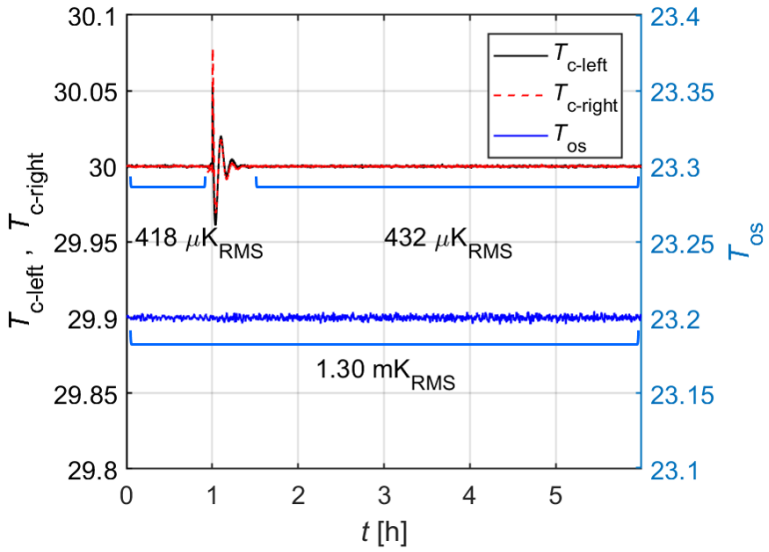


Figure 4-12. Stability of the capillary left ($T_{c\text{-left}}$), capillary right ($T_{c\text{-right}}$), and outer shield ($T_{os}$) temperatures during the introduction of reactants to the capillary tube at a setpoint of 30°C. The reactant gas ($H_2$ here) is introduced at $t$ = 1 h, perturbing $T_{c\text{-left}}$ and $T_{c\text{-right}}$ temperatures. The temperatures settle back to millikelvin stability within 15 minutes after introduction. The outer shield temperature is not affected by the introduction of reactants and remains steady. The RMS temperature variation in a 1 Hz bandwidth is shown in the intervals indicated by blue brackets.

### *Characterization of Pd nanoparticles*

The Pd nanoparticle samples used in this study are commercially available from US Research Nanomaterial Inc., with a mean diameter of 15 nm. Figure 4-13a shows a scanning electron microscope (SEM) image of the sample as purchased, showing a larger mean diameter of ~57 nm. After dispersion of the sample by five minutes of sonication in DI water, the image in Figure 4-13b is obtained which matches the specification mean diameter of ~15 nm. Figure 4-13c shows the energy-dispersive X-ray spectroscopy (EDX) spectrum of the sample, indicating the Pd and carbon (C) peaks. The elemental analysis shows 99.47 Wt% of Pd and 0.53 Wt% of C, the small carbon content may be due to sample contamination by carrying it in atmospheric condition.

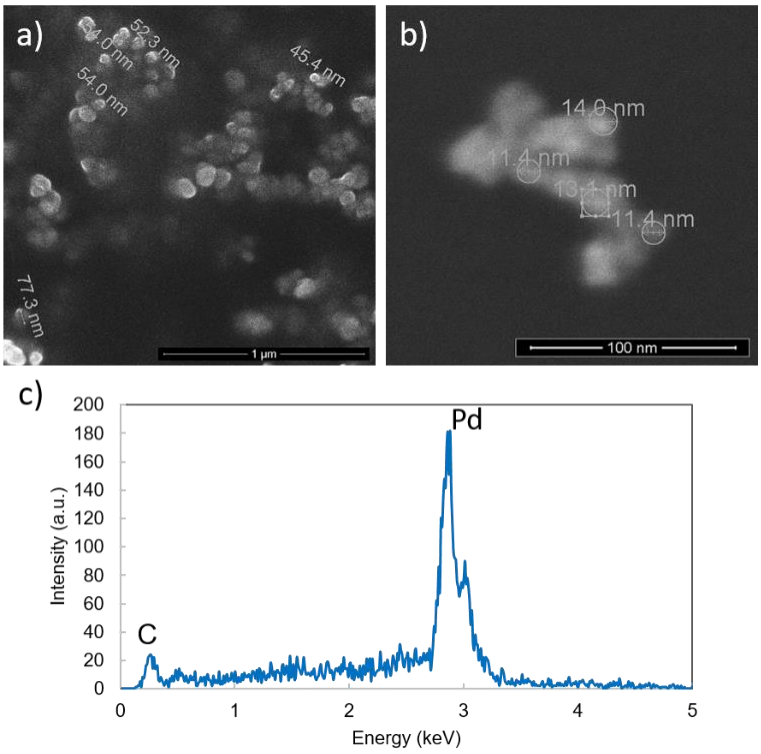


Figure 4-13. Characterization of commercial Pd nanomaterials used in $H_2$ reaction. SEM micrographs of (a) unprepared commercial Pd nanoparticle samples, (b) dispersed sample by sonication in DI water, (c) EDX spectrum of the sample showing peaks of Pd and carbon.

### *Enthalpy of hydrogenation of Pd nanoparticles*

Figure 4-14 shows some examples of the measurement of heat of hydrogenation of Pd nanoparticles at a hydrogen pressure of 3 bar. The heat release curves are of similar shape to the experiments at 7 bar (see Figure 4-9). However, they produce a smaller heat output as a result of less hydrogen absorption. The temperature offset after reactant introduction is also slightly different compared to the case of 7 bar which is due to the pressure-dependent conductance of the capillary tube, this effect is well captured and eliminated by measurement of baseline at the same reaction pressure of 3 bar. Therefore, at all reaction pressures tested here, the heat release goes to a value close to zero ~0.3 hours after reactant introduction.

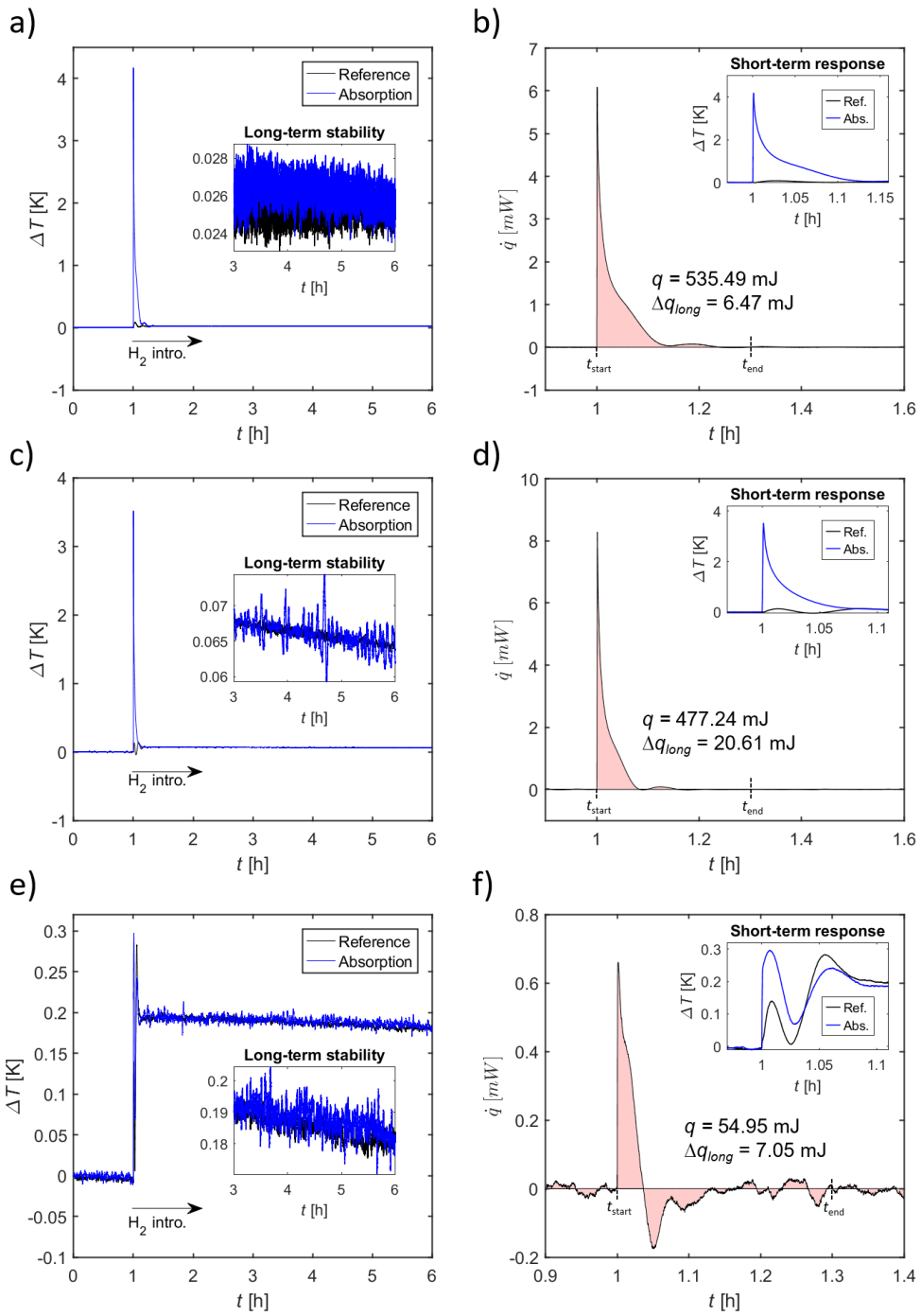


Figure 4-14. Experimental data of temperature rise and heat release rate associated with adsorption of $H_2$ on Pd samples obtained following the protocol described in Table 2 at an absolute pressure of 3 bar and at various temperatures (30 °C (a, b), 125 °C (c, d), and 230 °C (e, f). Panels (a), (c), and (e) show the $\Delta T$ recorded during the empty sample holder baseline experiment, as well as the absorption experiment using the Pd sample. The capillary reaction tube is under vacuum during the first hour of the experiment, at time $t$ = 1h hydrogen is introduced to the reaction tube resulting in an exothermic reaction and a transient heat output signal shown in panels (b), (d), and (f). The heat of reaction (q), shown by the shaded area in the right-hand graphs, is obtained by integrating the heat flow between $t$ = 1 to 1.3 h. The bounds on q show the long-term stability from $t$ = 5 to 6 h. The mass of the Pd sample was (a, b) 5.28 mg, (c, d) 3.89 mg, (e, f) 3.77 mg.

***Equilibrium hydrogen concentration on Pd nanoparticles***

To compare the results with the literature, the equilibrium H/Pd ratio is plotted on the phase diagram of H-Pd system for 32 nm Pd nanocubes in Figure 4-15. The solid lines indicate the results of a statistical mechanics Ising model (adapted from Griessen *et al.*[132]) and filled circles are experimental results using luminescent based sensing of H-content measured by Bardhan *et al.*[142]. However, since the photo-luminescent based approach does not provide an absolute value of H-content and only provides relative values, it is scaled by Griessen *et al.*[132] to fit their model. We have used the scaled values in this plot as well. It can be seen that all the measurements at 230 ºC (503 K) are either in the low concentration $\alpha$- phase or in the supercritical phase. On the other hand, measurements at 30 and 125 ºC are in the $\beta$- phase.

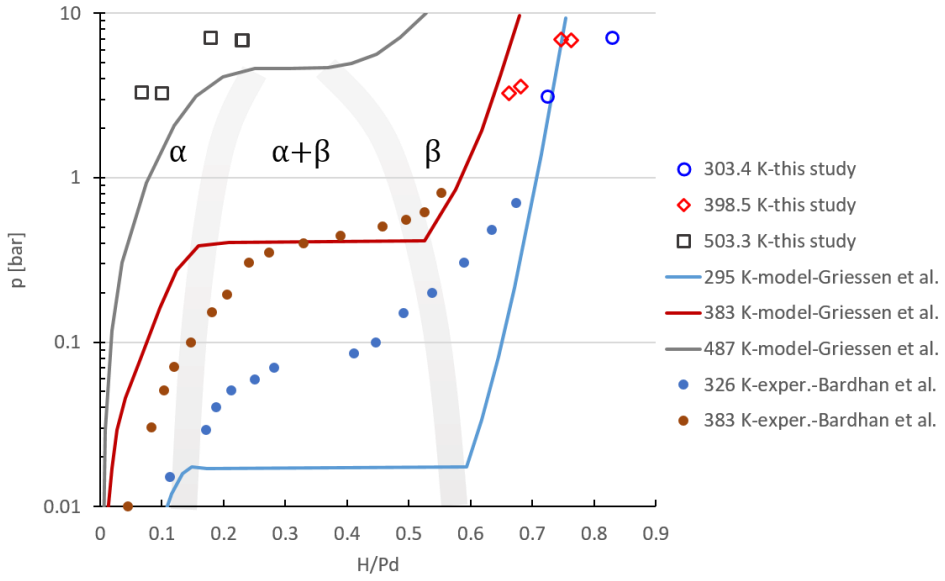


Figure 4-15. Equilibrium H/Pd ratio of 15 nm Pd nanoparticles obtained from the current instrument plotted on the phase diagram of H-Pd system of 32 nm Pd nanocubes. Solid lines show the results of a statistical mechanics Ising model (adapted with permission from Griessen *et al.*[132]. Copyright 2013 Springer Nature) and filled circles are experimental results using luminescent based sensing of H-content (adapted with permission from Griessen et al. which are scaled results measured by Bardhan *et al.*[142]).

Note: This work is reproduced with permission from *ACS Sensors*. See reference [20]

Amin Reihan, ***Ju Won Lim***, David K. Fork, Edgar Meyhofer*, and Pramod Reddy*

# Chapter 5 Summary and Future Work

## 5.1 Summary

Throughout my doctoral studies, my research has primarily focused on the development of calorimetric systems to explore radiative thermal transport and the thermodynamics of hydrogen ($H_2$) reactions for energy utilization. This field of study is closely connected to the growing demand for control of heat flow and thermal energy utilization. In the first chapter, I presented an overview of my research work, including the fundamental background and motivations behind it.

Chapter 2 illustrated the method of controlling the flow of thermal energy by developing a nanoscale photonic thermal transistor. In this work, source and drain electrodes were positioned close to a vanadium oxide gate electrode with adjustable dielectric properties achieved by temperature variation. We showed that when the gate is positioned within ~1 μm of the source-drain device and experiences a metal-insulator transition, the radiative heat transfer between the source and drain could be altered by a factor of three. Comprehensive calculations supported these experiments and elucidated the process of thermal modulation. Notably, unlike previous thermal transistors, this nanomembrane-based thermal transistor exhibited a significantly faster switching time (~500 ms compared to minutes) due to the small thermal mass of our nanoscale devices. These advancements are anticipated to open new possibilities for designing thermal logic circuits or devices for thermal management.

In Chapter 3, I presented direct measurements of the thickness-dependent near-field radiative heat transfer (NFRHT) between planar nanofilms of $MgF_2$ (thickness ranging from 20 nm to 500 nm). These measurements were conducted using microfabricated devices and a custom-developed nanopositioner. The results demonstrated, for the first time, that nanofilms can enhance thermal radiation up to 800-fold above the blackbody limit and are as effective as bulk materials when nanoscale gaps have dimensions smaller than the film thickness. Calculations based on fluctuational electrodynamics aligned well with the measured gap-size dependence of the heat transfer coefficient for films of all thicknesses, providing insights into the observed dependence. The experimental techniques and insights reported in this chapter lay the groundwork for systematically exploring novel thin films for near-field thermal and energy systems.

In Chapter 4, I presented an instrument designed for measuring the enthalpy of reactions involving gas-phase reactants (*e.g.*, $H_2$) on nanomaterial samples (*e.g.*, Pd). This instrument can accurately determine the net change in the amount of gas-phase reactants due to surface reactions over a temperature range from room temperature to 300 °C and reaction pressures of 10 mbar to 30 bar. The calorimetric resolution was demonstrated to be <3 μW/√Hz, with a long-term stability <4 μW/hour. The instrument's performance was showcased through experiments involving $H_2$ absorption on Pd nanoparticles at various pressures and temperatures. For this specific reaction, a mass balance resolution of 0.1 μmol/√Hz was achieved. The results from these experiments agree well with past studies, affirming the feasibility of conducting high-resolution calorimetry on milligram-scale nanomaterials for future studies in catalysis, phase transformations, and thermochemical energy storage.

In addition to the investigations outlined in this dissertation, I collaborated on several research projects as a co-author. I contributed to the development of a system that combines

photovoltaic (PV) cells with high-temperature emitter sources to capture and convert waste heat energy into electrical power (see ref.[5]). We achieved record power densities of ~5 kW/m$^2$ through a novel process involving the precise positioning of the emitter source with PV cells in the near-field (<100 nm) using a custom-built nanopositioner. This innovative process not only converts waste heat into useful energy but also contributes to environmental preservation. As an extension of this study, various heat sources, such as waste heat emitted from domestic gas furnaces, industrial factories, or power plants, can be harnessed to generate energy combined with PV cells.

Next, I participated in another project that explores the limits of near-field heat transfer enhancements in phonon-polaritonic materials (see ref.[54]). In this project, we theoretically demonstrated that surface phonon-polariton (SPhP)-mediated near-field radiative heat transfer (NFRHT) at room temperature can be 5-fold larger than that of $SiO_2$ for materials supporting SPhPs closer to an optimal frequency of 67 meV. We then experimentally demonstrated that materials like $MgF_2$ and $Al_2O_3$ closely approach this limit. Specifically, we showed that the near-field thermal conductance between $MgF_2$ plates separated by 50 nm approaches nearly 50% of the global SPhP bound. These findings lay the foundation for exploring the limits of radiative heat transfer rates at the nanoscale.

I also played a role in a project centered around near-field radiative heat transfer at cryogenic temperatures mediated by surface phonon polaritons (see ref.[78]). In this study, we explored thermal transport in nanoscale gaps between a silica sphere and a planar silica surface across a temperature range of 77–300 K. Our experiments revealed that cryogenic NFRHT has strong contributions from SPhPs and does not follow the $T^3$ temperature ($T$) dependence of far-field thermal radiation. Our modeling, based on fluctuational electrodynamics, showed that the temperature dependence of NFRHT can be related to the confinement of heat transfer to two

narrow frequency ranges and is well accounted for by a simple analytical model. These advances enable detailed NFRHT studies at cryogenic temperatures relevant to thermal management and solid-state cooling applications. These additional projects, aligned with my dissertation, provided valuable insights and in-depth knowledge in the fields of thermal radiation management, energy conversion, calorimetric systems, and related areas.

## 5.2 Future Work

### *5.2.1 Logic Gates Using Photonic Thermal Transistors*

Building upon the investigations mentioned in this dissertation, it is possible to explore other applications based on photonic thermal transistors. Future work can explore the development of photonic thermal logic gates that can be employed to perform logical operations, opening up new possibilities for integrated photonic thermal logic circuits and computing systems. Logic gates, including AND, OR, NOT, XOR, and NOR gates, can be realized by appropriately configuring and combining these photonic thermal transistors. Figure 5-1a schematically illustrates a photonic thermal logic gate where three-terminal devices are coated with $VO_x$. The phase of $VO_x$ can change to either an insulator or metal, depending on the temperature. This two-phase $VO_x$ layer serves as two variable inputs (*e.g.*, insulator: input is 0, metal: input is 1) in a logic gate, contingent on the temperature. According to SCUFF-EM simulations presented in Figure 5-1b, the thermal conductance between the source and the drain varies with the phase of $VO_x$ as well as the gap size. For instance, when both the source and gate are insulators (*i.e.*, Input (S) = 0, Input (G) = 0) at a gap size of 0 μm, the heat current between the source and the drain ($\dot{Q}_{S\text{-}D}$) is large (Output (D) = 1) compared to the others, resulting in a high-temperature output on the drain device ($T_D > T_{ref}$). (Note that the proper reference temperature ($T_{ref}$) should be set in this

measurement.) This suggests that by properly setting the reference temperature, the device can function as a NOR logic device when the gap $d$ = 0 μm. Furthermore, this $VO_x$-coated device can function as other logic devices (*e.g.*, NOT, NAND), depending on the gap size.

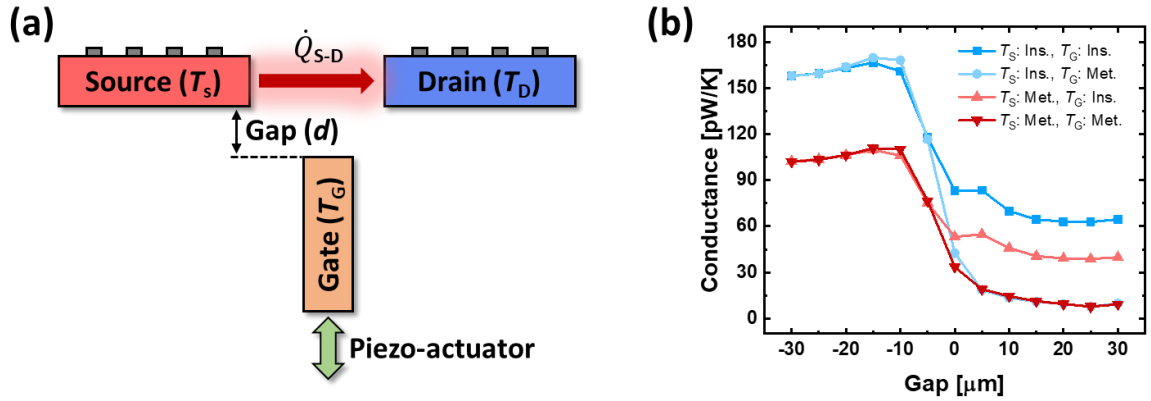


Figure 5-1. A concept of a photonic thermal transistor and simulation results. (a) A schematic of a photonic thermal transistor where the heat current between the source and the drain changes with the position of the gate device. (b) The computed conductance between the source and the drain as a function of the gap size, $d$, through SCUFF-EM simulations.

Advancing the development of photonic thermal transistors and logic gates likely will enable the creation of computing systems. Computing systems, which have attracted significant attention in the fields of photonics and thermal technology, offer a promising avenue for creating calculation systems by manipulating heat currents through the use of photon signals[50]. With further studies, the interplay between thermal properties and photons could be one of the options for the advancement of quantum information processing systems which have the potential to significantly surpass current traditional computing systems in terms of computational power and speed[146, 147]. As research in this field progresses in the future, there will likely be groundbreaking developments that reshape the landscape of computing systems and propel us into a new era of technological possibilities.

### *5.2.2 Hydrogen ($H_2$) Storage System for Fuel Cell and Electric Vehicles*

One of my projects, as explained in Chapter 4, involved the development of a hydrogen storage system resulting from a chemical reaction when the metal transforms into metal hydrides. To analyze size-dependent hydrogen storage capacity, thermodynamics, and kinetics, I have synthesized various sizes of Pd nanoparticles (Figure 5-2).

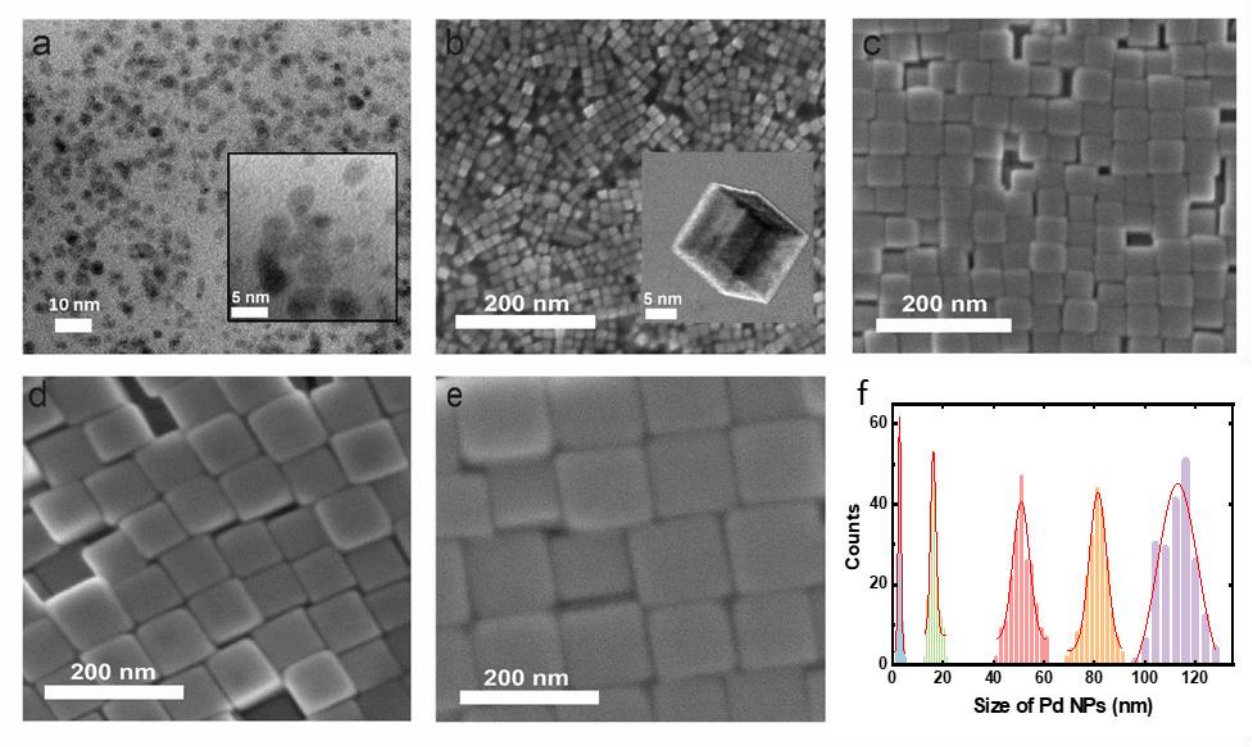


Figure 5-2. SEM images of the synthesized Pd nanoparticles with various sizes. The measured average sizes are as follows: (a) 3 nm, (b) 15 nm, (c) 50 nm, (d) 81 nm, and (e) 113 nm, respectively. (f) The frequency distribution of the synthesized Pd nanoparticles, with a total of 200 counts for each type, includes a Gaussian fitting result shown as a red curve to obtain the average size of the Pd NPs.

Pd-based hydrides are well-known for retaining a high hydrogen storage capacity due to their ability to chemically react with hydrogen, forming stable compounds[148, 149]. A chemical bonding in the Pd hydrides allows them to store a significant amount of hydrogen, making them promising candidates for efficient and compact hydrogen storage systems. Related techniques can be utilized in various hydrogen-based renewable energy applications such as hydrogen fuel cells or vehicles, providing a valuable method suitable for the development of sustainable energy

sources[47]. I plan to advance the development of a hydrogen storage system by utilizing metal hydride nanomaterials, including metal nanoparticles, alloy structures, and metal-organic framework structures to improve hydrogen storage capacity[43].

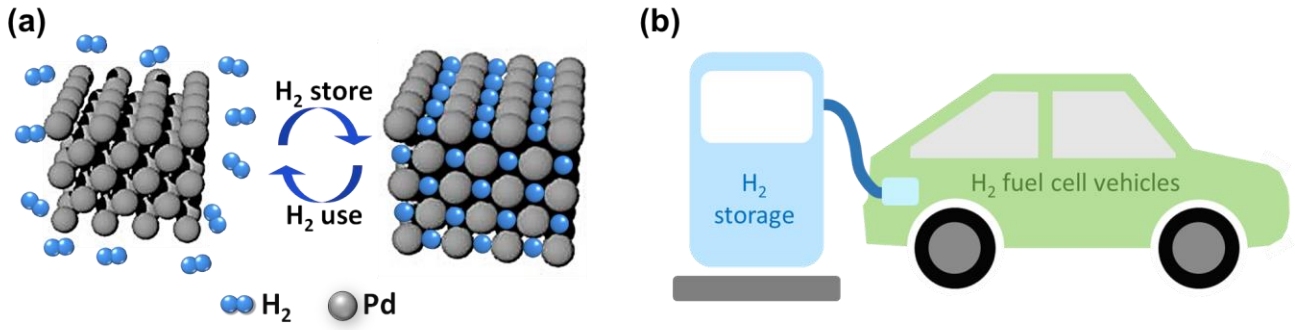


Figure 5-3. Hydride-based $H_2$ storage system. (a) Demonstration of an $H_2$ storage system utilizing Pd nanoparticles for storing and releasing $H_2$. (b) Concept of hydrogen fuel cell electric vehicles driven by $H_2$.

Pd hydride-based $H_2$ storage systems allow transportation and handling of hydrogen more manageable compared to conventional $H_2$ tank. Moreover, in contrast to storage methods involving high-pressure gas or cryogenic liquid hydrogen, metal hydride-based storage systems ensure enhanced safety as they do not necessitate high temperature or pressure[150]. As depicted in Figure 5-3a, a metal hydride-based $H_2$ storage system allows repeatable storage and retrieval of stored hydrogen. One of the applications of $H_2$ storage systems is particularly prominent in the automotive industry, where $H_2$ serves as a clean and sustainable energy source for $H_2$ fuel cell vehicles (Figure 5-3b), which represents a promising avenue for clean and sustainable transportation[151]. Hydrogen fuel cell vehicles utilize this technology to propel electric motors, offering a zero-emission alternative to traditional internal combustion engine vehicles. The environmental benefits of hydrogen fuel cell vehicles lie in their ability to produce electricity without emitting pollutants. The only byproduct of the electrochemical reaction in a hydrogen fuel cell is water vapor, making these vehicles a compelling solution for reducing greenhouse gas

emissions and addressing air quality concerns. As advancements in hydrogen production, storage, and fuel cell technologies continue, hydrogen fuel cell vehicles hold the potential to play a crucial role in the transition toward sustainable and low-carbon transportation solutions.

## Bibliography


1. Song, C. Global challenges and strategies for control, conversion and utilization of $CO_2$ for sustainable development involving energy, catalysis, adsorption and chemical processing. *Catalysis Today* **115**, 2-32 (2006).
2. Doğan, B., Driha, O.M., Balsalobre Lorente, D. & Shahzad, U. The mitigating effects of economic complexity and renewable energy on carbon emissions in developed countries. *Journal of Sustainable Development* **29**, 1-12 (2021).
3. Kumar, K.R., Chaitanya, N.K. & Kumar, N.S. Solar thermal energy technologies and its applications for process heating and power generation–A review. *Journal of Cleaner Production* **282**, 125296 (2021).
4. Raihan, A. *et al.* Nexus between carbon emissions, economic growth, renewable energy use, urbanization, industrialization, technological innovation, and forest area towards achieving environmental sustainability in Bangladesh. *Energy and Climate Change* **3**, 100080 (2022).
5. Mittapally, R. *et al.* Near-field thermophotovoltaics for efficient heat to electricity conversion at high power density. *Nature Communications* **12**, 4364 (2021).
6. Wong, M., Tso, C., Ho, T. & Lee, H. A review of state of the art thermal diodes and their potential applications. *International Journal of Heat Mass Transfer* **164**, 120607 (2021).
7. Lee, J. *et al.* Enhanced pyroelectric conversion of thermal radiation energy: Energy harvesting and non-contact proximity sensor. *Nano Energy* **97**, 107178 (2022).
8. Basu, S., Chen, Y.B. & Zhang, Z. Microscale radiation in thermophotovoltaic devices—a review. *International Journal of Energy Research* **31**, 689-716 (2007).
9. Casati, G. Controlling the heat flow: Now it is possible. *Chaos: An Interdisciplinary Journal of Nonlinear Science* **15** (2005).
10. Li, Y. *et al.* Transforming heat transfer with thermal metamaterials and devices. *Nature Reviews Materials* **6**, 488-507 (2021).
11. Latella, I., Marconot, O., Sylvestre, J., Fréchette, L.G. & Ben-Abdallah, P. Dynamical response of a radiative thermal transistor based on suspended insulator-metal-transition membranes. *Physical Review Applied* **11**, 024004 (2019).
12. Joulain, K., Ezzahri, Y., Drevillon, J. & Ben-Abdallah, P. Modulation and amplification of radiative far field heat transfer: Towards a simple radiative thermal transistor. *Applied Physics Letters* **106** (2015).
13. Yang, X. *et al.* Thermal Rectifier and Thermal Transistor of 1T/2H MoS2 for Heat Flow Management. *ACS Applied Materials & Interfaces* **14**, 4434-4442 (2022).

14. Sood, A. *et al.* An electrochemical thermal transistor. *Nature Communications* **9**, 4510 (2018).

15. Castelli, L., Zhu, Q., Shimokusu, T.J. & Wehmeyer, G. A three-terminal magnetic thermal transistor. *Nature Communications* **14**, 393 (2023).

16. Glotz, G., Knoechel, D.J., Podmore, P., Gruber-Woelfler, H. & Kappe, C.O. Reaction Calorimetry in Microreactor Environments—Measuring Heat of Reaction by Isothermal Heat Flux Calorimetry. *Organic Process Research & Development* **21**, 763-770 (2017).

17. Kumpinsky, E. A method to determine heat-transfer coefficients in a heat-flow reaction calorimeter. *Thermochimica Acta* **289**, 351-366 (1996).

18. Cheng, T.-Y., Brunschwig, B.S. & Bullock, R.M. Hydride transfer reactions of transition metal hydrides: Kinetic hydricity of metal carbonyl hydrides. *Journal of the American Chemical Society* **120**, 13121-13137 (1998).

19. Dornheim, M. Thermodynamics of metal hydrides: tailoring reaction enthalpies of hydrogen storage materials, in *Thermodynamics-Interaction Studies-Solids, Liquids and Gases* (IntechOpen, 2011).

20. Reihani, A., Lim, J.W., Fork, D.K., Meyhofer, E. & Reddy, P. Microwatt-resolution calorimeter for studying the reaction thermodynamics of nanomaterials at high temperature and pressure. *ACS Sensors* **6**, 387-398 (2020).

21. Su, J. & Chen, J.-S. Synthetic porous materials applied in hydrogenation reactions. *Microporous Mesoporous Materials* **237**, 246-259 (2017).

22. Michaelsen, C., Barmak, K. & Weihs, T. Investigating the thermodynamics and kinetics of thin film reactions by differential scanning calorimetry. *Journal of Physics D: Applied Physics* **30**, 3167 (1997).

23. Zogg, A., Stoessel, F., Fischer, U. & Hungerbühler, K. Isothermal reaction calorimetry as a tool for kinetic analysis. *Thermochimica Acta* **419**, 1-17 (2004).

24. Halkos, G.E. & Gkampoura, E.-C. Reviewing usage, potentials, and limitations of renewable energy sources. *Energies* **13**, 2906 (2020).

25. Qazi, A. *et al.* Towards sustainable energy: a systematic review of renewable energy sources, technologies, and public opinions. *IEEE Access* **7**, 63837-63851 (2019).

26. Alva, G., Lin, Y. & Fang, G. An overview of thermal energy storage systems. *Energy* **144**, 341-378 (2018).

27. Roskilly, A. & Yan, J. Sustainable thermal energy management. *Applied Energy* **186**, 249-250 (2017).

28. Erickson, G. & Tiberghien, A. Heat and temperature. *Children's ideas in science*, 52-84 (1985).

29. Nellis, G. & Klein, S. *Heat transfer*. (Cambridge university press, 2008).

30. Howell, J.R., Mengüç, M.P., Daun, K. & Siegel, R. *Thermal radiation heat transfer*. (CRC press, 2020).

31. Cuevas, J.C. & García-Vidal, F.J. Radiative heat transfer. *ACS Photonics* **5**, 3896-3915 (2018).

32. Incropera, F., DeWitt, D., Bergman, T. & Lavine, A. (2007).

33. Riddle, J.L., Furukawa, G.T. & Plumb, H.H. *Platinum resistance thermometry*, Vol. 126. (National Bureau of Standards, 1973).

34. Atherton, A. & Fitton, D. Temperature definition and measurement using platinum resistance thermometers. *Transactions of the Institute of Measurement and Control* **11**, 15-24 (1989).

35. Wellons, M. The Stefan-Boltzmann Law. *Physics Department, The College of Wooster, Wooster, Ohio* **44691**, 25 (2007).

36. Song, B. *et al.* Enhancement of near-field radiative heat transfer using polar dielectric thin films. *Nature Nanotechnology* **10**, 253-258 (2015).

37. Mittapally, R., Lim, J.W., Meyhofer, E., Reddy, P. & Song, B. Quantifying the Effect of Nanofilms on Near-Field Radiative Heat Transfer. *ACS Photonics* **10**, 2474-2480 (2023).

38. Thompson, D. *et al.* Hundred-fold enhancement in far-field radiative heat transfer over the blackbody limit. *Nature* **561**, 216-221 (2018).

39. Thompson, D., Zhu, L., Meyhofer, E. & Reddy, P. Nanoscale radiative thermal switching via multi-body effects. *Nature Nanotechnology* **15**, 99-104 (2020).

40. Zheng, J. *et al.* Current research trends and perspectives on solid-state nanomaterials in hydrogen storage. *Research* (2021).

41. Mukherjee, B., Gupta, V. & Agnihotri, S. Nanostructures for Hydrogen Storage. *Nanochemistry: Synthesis, Characterization and Applications*, 361 (2023).

42. Niemann, M.U. *et al.* Nanomaterials for hydrogen storage applications: a review. *Journal of Nanomaterials* **2008** (2008).

43. Dekura, S., Kobayashi, H., Kusada, K. & Kitagawa, H. Hydrogen in Palladium and Storage Properties of Related Nanomaterials: Size, Shape, Alloying, and Metal-Organic Framework Coating Effects. *ChemPhysChem* **20**, 1158-1176 (2019).

44. Srinivasan, S. *et al.* Reversible hydrogen storage using nanocomposites. *Applied Sciences* **10**, 4618 (2020).

45. Veluswamy, H.P., Kumar, R. & Linga, P. Hydrogen storage in clathrate hydrates: Current state of the art and future directions. *Applied Energy* **122**, 112-132 (2014).

46. Adelhelm, P. & De Jongh, P.E. The impact of carbon materials on the hydrogen storage properties of light metal hydrides. *Journal of Materials Chemistry* **21**, 2417-2427 (2011).

47. Srinivasan, S.S. & Demirocak, D.E. Metal hydrides used for hydrogen storage. *Nanostructured materials for next-generation energy storage and conversion: hydrogen production, storage, utilization*, 225-255 (2017).

48. Wang, L. & Li, B. Thermal logic gates: computation with phonons. *Physical Review Letters* **99**, 177208 (2007).

49. Ben-Abdallah, P. & Biehs, S.-A. Near-field thermal transistor. *Physical Review Letters* **112**, 044301 (2014).

50. Hamed, A., Elzouka, M. & Ndao, S. Thermal calculator. *International Journal of Heat and Mass Transfer* **134**, 359-365 (2019).

51. Bhatt, G.R. *et al.* Integrated near-field thermo-photovoltaics for heat recycling. *Nature Communications* **11**, 2545 (2020).

52. Messina, R. & Ben-Abdallah, P. Graphene-based photovoltaic cells for near-field thermal energy conversion. *Scientific Reports* **3**, 1383 (2013).

53. Marconot, O., Juneau-Fecteau, A. & Fréchette, L.G. Toward applications of near-field radiative heat transfer with micro-hotplates. *Scientific Reports* **11**, 14347 (2021).

54. Mittapally, R. *et al.* Probing the limits to near-field heat transfer enhancements in phonon-polaritonic materials. *Nano Letters* **23**, 2187-2194 (2023).

55. DeSutter, J., Tang, L. & Francoeur, M. A near-field radiative heat transfer device. *Nature Nanotechnology* **14**, 751-755 (2019).

56. Zhu, L. *et al.* Near-field photonic cooling through control of the chemical potential of photons. *Nature* **566**, 239-244 (2019).

57. Raman, A.P., Anoma, M.A., Zhu, L., Rephaeli, E. & Fan, S. Passive radiative cooling below ambient air temperature under direct sunlight. *Nature* **515**, 540-544 (2014).

58. Prod'Homme, H., Ordonez-Miranda, J., Ezzahri, Y., Drevillon, J. & Joulain, K. Optimized thermal amplification in a radiative transistor. *Journal of Applied Physics* **119** (2016).

59. Chen, F., Liu, X., Tian, Y., Wang, D. & Zheng, Y. Non-contact thermal transistor effects modulated by nanoscale mechanical deformation. *Journal of Quantitative Spectroscopy and Radiative Transfer* **259**, 107414 (2021).

60. Ordonez-Miranda, J., Ezzahri, Y., Drevillon, J. & Joulain, K. Dynamical heat transport amplification in a far-field thermal transistor of VO2 excited with a laser of modulated intensity. *Journal of Applied Physics* **119** (2016).

61. Nishizawa, J.-i., Terasaki, T. & Shibata, J. Field-effect transistor versus analog transistor (static induction transistor). *IEEE Transactions on Electron Devices* **22**, 185-197 (1975).

62. Ma, J., Cho, H.J., Heo, J., Kim, S. & Yoo, G. Asymmetric Double-Gate β-Ga2O3 Nanomembrane Field-Effect Transistor for Energy-Efficient Power Devices. *Advanced Electronic Materials* **5**, 1800938 (2019).

63. Yang, Q. *et al.* Solid-state electrochemical thermal transistors. *Advanced Functional Materials*, 2214939 (2023).

64. Li, Y. *et al.* Radiative Thermal Transistor. *Physical Review Applied* **20**, 024061 (2023).

65. Fiorino, A. *et al.* A thermal diode based on nanoscale thermal radiation. *ACS Nano* **12**, 5774-5779 (2018).

66. Yang, H.W. *et al.* Unusual M2-mediated metal-insulator transition in epitaxial VO2 thin films on GaN substrates. *Europhysics Letters* **109**, 27004 (2015).

67. Kumar, C.V.S., Maury, F. & Bahlawane, N. Vanadium Oxide as a Key Constituent in Reconfigurable Metamaterials, in *Metamaterials and Metasurfaces* (IntechOpen, 2018).

68. Li, N. *et al.* Colloquium: Phononics: Manipulating heat flow with electronic analogs and beyond. *Reviews of Modern Physics* **84**, 1045 (2012).

69. Wang, L. & Li, B. Thermal memory: a storage of phononic information. *Physical Review Letters* **101**, 267203 (2008).

70. Ganjeh, Y. *et al.* A platform to parallelize planar surfaces and control their spatial separation with nanometer resolution. *Review of Scientific Instruments* **83** (2012).

71. Song, B. *et al.* Radiative heat conductances between dielectric and metallic parallel plates with nanoscale gaps. *Nature Nanotechnology* **11**, 509-514 (2016).

72. Paik, T. *et al.* Solution-processed phase-change VO2 metamaterials from colloidal vanadium oxide (VO x) nanocrystals. *ACS Nano* **8**, 797-806 (2014).

73. Majumder, A., Thompson, D., Mittapally, R., Reddy, P. & Meyhofer, E. Quantifying the Spatial Distribution of Radiative Heat Transfer in Subwavelength Planar Nanostructures. *ACS Photonics* **10**, 1144-1149 (2023).

74. Cho, J. *et al.* Electrochemically tunable thermal conductivity of lithium cobalt oxide. *Nature Communications* **5**, 4035 (2014).

75. Liu, X., Wang, L. & Zhang, Z.M. Near-field thermal radiation: recent progress and outlook. *Nanoscale and Microscale Thermophysical Engineering* **19**, 98-126 (2015).

76. Zhang, Y., Xiong, W., Chen, W. & Zheng, Y. Recent progress on vanadium dioxide nanostructures and devices: Fabrication, properties, applications and perspectives. *Nanomaterials* **11**, 338 (2021).

77. Morsy, A.M. *et al.* Experimental demonstration of dynamic thermal regulation using vanadium dioxide thin films. *Scientific Reports* **10**, 13964 (2020).

78. Yan, S. *et al.* Surface Phonon Polariton-Mediated Near-Field Radiative Heat Transfer at Cryogenic Temperatures. *Physical Review Letters* **131**, 196302 (2023).

79. Planck, M. *The theory of heat radiation*. (Blakiston, 1914).

80. Song, B., Fiorino, A., Meyhofer, E. & Reddy, P. Near-field radiative thermal transport: From theory to experiment. *AIP Advances* **5** (2015).

81. Biehs, S.-A. *et al.* Near-field radiative heat transfer in many-body systems. *Reviews of Modern Physics* **93**, 025009 (2021).

82. Fiorino, A. *et al.* Nanogap near-field thermophotovoltaics. *Nature Nanotechnology* **13**, 806-811 (2018).

83. Lucchesi, C. *et al.* Near-field thermophotovoltaic conversion with high electrical power density and cell efficiency above 14%. *Nano Letters* **21**, 4524-4529 (2021).

84. Chen, K., Santhanam, P., Sandhu, S., Zhu, L. & Fan, S. Heat-flux control and solid-state cooling by regulating chemical potential of photons in near-field electromagnetic heat transfer. *Physical Review B* **91**, 134301 (2015).

85. Li, Q., He, H., Chen, Q. & Song, B. Thin-film radiative thermal diode with large rectification. *Physical Review Applied* **16**, 014069 (2021).

86. Kim, K. *et al.* Radiative heat transfer in the extreme near field. *Nature* **528**, 387-391 (2015).

87. Fiorino, A. *et al.* Giant enhancement in radiative heat transfer in sub-30 nm gaps of plane parallel surfaces. *Nano Letters* **18**, 3711-3715 (2018).

88. Lim, M., Song, J., Lee, S.S. & Lee, B.J. Tailoring near-field thermal radiation between metallo-dielectric multilayers using coupled surface plasmon polaritons. *Nature Communications* **9**, 4302 (2018).

89. Salihoglu, H. *et al.* Near-field thermal radiation between two plates with sub-10 nm vacuum separation. *Nano Letters* **20**, 6091-6096 (2020).

90. Wang, X., Basu, S. & Zhang, Z. Parametric optimization of dielectric functions for maximizing nanoscale radiative transfer. *Journal of Physics D: Applied Physics* **42**, 245403 (2009).

91. Nefzaoui, E., Ezzahri, Y., Drévillon, J. & Joulain, K. Maximal near-field radiative heat transfer between two plates. *The European Physical Journal-Applied Physics* **63**, 30902 (2013).

92. Zhang, L. & Miller, O.D. Optimal materials for maximum large-area near-field radiative heat transfer. *ACS Photonics* **7**, 3116-3129 (2020).

93. Biehs, S.-A., Tschikin, M. & Ben-Abdallah, P. Hyperbolic metamaterials as an analog of a blackbody in the near field. *Physical Review Letters* **109**, 104301 (2012).

94. Fernández-Hurtado, V., García-Vidal, F.J., Fan, S. & Cuevas, J.C. Enhancing near-field radiative heat transfer with Si-based metasurfaces. *Physical Review Letters* **118**, 203901 (2017).

95. Francoeur, M., Mengüç, M.P. & Vaillon, R. Near-field radiative heat transfer enhancement via surface phonon polaritons coupling in thin films. *Applied Physics Letters* **93** (2008).

96. Li, Q., Chen, Q. & Song, B. Fundamental limit to the rectification of near-field heat flow: The potential of intrinsic semiconductor films. *Physical Review B* **106**, 075408 (2022).

97. Challener, W. *et al.* Heat-assisted magnetic recording by a near-field transducer with efficient optical energy transfer. *Nature Photonics* **3**, 220-224 (2009).

98. Ben-Abdallah, P., Joulain, K., Drevillon, J. & Domingues, G. Near-field heat transfer mediated by surface wave hybridization between two films. *Journal of Applied Physics* **106** (2009).

99. Biehs, S.-A. Thermal heat radiation, near-field energy density and near-field radiative heat transfer of coated materials. *The European Physical Journal B* **58**, 423-431 (2007).

100. Basu, S. & Zhang, Z. Ultrasmall penetration depth in nanoscale thermal radiation. *Applied Physics Letters* **95** (2009).

101. Sabbaghi, P. *et al.* Super-Planckian radiative heat transfer between macroscale metallic surfaces due to near-field and thin-film effects. *Journal of Applied Physics* **128** (2020).

102. Lim, M., Song, J., Lee, S.S., Lee, J. & Lee, B.J. Surface-plasmon-enhanced near-field radiative heat transfer between planar surfaces with a thin-film plasmonic coupler. *Physical Review Applied* **14**, 014070 (2020).

103. Rincón-García, L. *et al.* Enhancement and saturation of near-field radiative heat transfer in nanogaps between metallic surfaces. *Physical Review Letters* **129**, 145901 (2022).

104. Polder, D. & Van Hove, M. Theory of radiative heat transfer between closely spaced bodies. *Physical Review B* **4**, 3303 (1971).

105. Rytov, S.M., Kravt͡sov, I.U.r.A. & Tatarskiĭ, V.i.a.n.I.i. *Principles of Statistical Radiophysics: Wave Propagation Through Random Media*, Vol. 4. (Springer, 1989).

106. Palik, E.D. *Handbook of optical constants of solids*, Vol. 3. (Academic press, 1998).

107. Joulain, K., Mulet, J.-P., Marquier, F., Carminati, R. & Greffet, J.-J. Surface electromagnetic waves thermally excited: Radiative heat transfer, coherence properties and Casimir forces revisited in the near field. *Surface Science Reports* **57**, 59-112 (2005).

108. Ben-Abdallah, P. & Joulain, K. Fundamental limits for noncontact transfers between two bodies. *Physical Review B* **82**, 121419 (2010).

109. Yeh, P. & Hendry, M. Optical waves in layered media. *Physics Today* **43**, 77 (1990).

110. Basu, S., Lee, B.J. & Zhang, Z. Near-field radiation calculated with an improved dielectric function model for doped silicon. (2010).

111. Prieto, G., Zečević, J., Friedrich, H., De Jong, K.P. & De Jongh, P.E. Towards stable catalysts by controlling collective properties of supported metal nanoparticles. *Nature Materials* **12**, 34-39 (2013).

112. Murdoch, M. *et al.* The effect of gold loading and particle size on photocatalytic hydrogen production from ethanol over $Au/TiO_2$ nanoparticles. *Nature Chemistry* **3**, 489-492 (2011).

113. Mohtadi, R. & Orimo, S.-i. The renaissance of hydrides as energy materials. *Nature Reviews Materials* **2**, 1-15 (2016).

114. Xu, Z. *et al.* Size-dependent catalytic activity of supported metal clusters. *Nature* **372**, 346-348 (1994).

115. Mauron, P., Bielmann, M., Bissig, V., Remhof, A. & Züttel, A. High-pressure and high-temperature differential scanning calorimeter for combined pressure-concentration-temperature measurements of hydrides. *Review of Scientific Instruments* **80** (2009).

116. MacLeod, B. *et al.* High-temperature high-pressure calorimeter for studying gram-scale heterogeneous chemical reactions. *Review of Scientific Instruments* **88** (2017).

117. Akiba, H. *et al.* Development of adiabatic calorimetry system for enthalpy of gas absorption/adsorption and its application to $H_2/D_2$ absorption into palladium nanoparticles. *Thermochimica Acta* **670**, 87-91 (2018).

118. Fischer-Wolfarth, J.-H. *et al.* An improved single crystal adsorption calorimeter for determining gas adsorption and reaction energies on complex model catalysts. *Review of Scientific Instruments* **82** (2011).

119. Smith, A.L. & Shirazi, H.M. Principles of quartz crystal microbalance/heat conduction calorimetry: Measurement of the sorption enthalpy of hydrogen in palladium. *Thermochimica Acta* **432**, 202-211 (2005).

120. Huang, S.-Y., Huang, C.-D., Chang, B.-T. & Yeh, C.-T. Chemical activity of palladium clusters: sorption of hydrogen. *The Journal of Physical Chemistry B* **110**, 21783-21787 (2006).

121. Fiorino, A. *et al.* Parallelized, real-time, metabolic-rate measurements from individual Drosophila. *Scientific Reports* **8**, 14452 (2018).

122. Hur, S., Mittapally, R., Yadlapalli, S., Reddy, P. & Meyhofer, E. Sub-nanowatt resolution direct calorimetry for probing real-time metabolic activity of individual C. elegans worms. *Nature Communications* **11**, 2983 (2020).

123. Lide, D.R. *CRC handbook of chemistry and physics*, Vol. 85. (CRC press, 2004).

124. Incropera, F.P., Dewitt, D.P., Bergman, T.L. & Lavine, A.S. Fundamentals of heat and mass transfer, John Wiley & Sons. *Inc., Hoboken, NJ.* (2002).

125. Assael, M., Botsios, S., Gialou, K. & Metaxa, I. Thermal conductivity of polymethyl methacrylate (PMMA) and borosilicate crown glass BK7. *International Journal of Thermophysics* **26**, 1595-1605 (2005).

126. Powell, R., Ho, C.Y. & Liley, P.E. *Thermal conductivity of selected materials*, Vol. 8. (US Department of Commerce, National Bureau of Standards Washington, DC, 1966).

127. Roder, H. Thermal conductivity of hydrogen for temperatures between 78 and 310 K with pressures to 70 MPa. *International journal of Thermophysics* **5**, 323-350 (1984).

128. McMAHON, H.O. Thermal radiation characteristics of some glasses. *Journal of the American Ceramic Society* **34**, 91-96 (1951).

129. Tava´ rez, A. & Gonza´ lez, J. Modeling the thermal behavior of solder paste inside reflow ovens. *Journal of Electronic Packaging* **125**, 335-346 (2003).

130. Vries, T.D. Specific Heat of Pyrex Glass from 25° to 175° C. *Industrial & Engineering Chemistry* **22**, 617-618 (1930).

131. Sharp, D. & Ginther, L. Effect of composition and temperature on the specific heat of glass. *Journal of the American Ceramic Society* **34**, 260-271 (1951).

132. Griessen, R., Strohfeldt, N. & Giessen, H. Thermodynamics of the hybrid interaction of hydrogen with palladium nanoparticles. *Nature Materials* **15**, 311-317 (2016).

133. Syrenova, S. *et al.* Hydride formation thermodynamics and hysteresis in individual Pd nanocrystals with different size and shape. *Nature Materials* **14**, 1236-1244 (2015).

134. Yamauchi, M., Ikeda, R., Kitagawa, H. & Takata, M. Nanosize effects on hydrogen storage in palladium. *The Journal of Physical Chemistry C* **112**, 3294-3299 (2008).

135. Behm, R., Penka, V., Cattania, M.G., Christmann, K. & Ertl, G. Evidence for ‘‘subsurface’’hydrogen on Pd (110): An intermediate between chemisorbed and dissolved species. *The Journal of Chemical Physics* **78**, 7486-7490 (1983).

136. Langhammer, C., Zhdanov, V.P., Zorić, I. & Kasemo, B. Size-dependent kinetics of hydriding and dehydriding of Pd nanoparticles. *Physical Review Letters* **104**, 135502 (2010).

137. Johnson, N.J. *et al.* Facets and vertices regulate hydrogen uptake and release in palladium nanocrystals. *Nature Materials* **18**, 454-458 (2019).

138. Jewell, L.L. & Davis, B.H. Review of absorption and adsorption in the hydrogen–palladium system. *Applied Catalysis A: General* **310**, 1-15 (2006).

139. Dantzer, P. & Millet, P. Advances in hydride phase growth: Automatic high precision calorimeter-volumetric devices, for thermodynamic and kinetics analyses. *Review of Scientific Instruments* **71**, 142-153 (2000).

140. Wadell, C. *et al.* Thermodynamics of hydride formation and decomposition in supported sub-10 nm Pd nanoparticles of different sizes. *Chemical Physics Letters* **603**, 75-81 (2014).

141. Robinson, D.B., Luo, W., Cai, T.Y. & Stewart, K.D. Metal hydride differential scanning calorimetry as an approach to compositional determination of mixtures of hydrogen isotopologues and helium. *International Journal of Hydrogen Energy* **40**, 14257-14270 (2015).

142. Bardhan, R. *et al.* Uncovering the intrinsic size dependence of hydriding phase transformations in nanocrystals. *Nature Materials* **12**, 905-912 (2013).

143. Ziegler, J.G. & Nichols, N.B. Optimum settings for automatic controllers. *Transactions of the American Society of Mechanical Engineers* **64**, 759-765 (1942).

144. Åström, K.J. & Wittenmark, B. *Computer-controlled systems: theory and design*. (Courier Corporation, 2013).

145. Ioannou, P. & Sun, J. Robust adaptive control Courier Corporation. *Courier Corporation* (2012).

146. Slussarenko, S. & Pryde, G.J. Photonic quantum information processing: A concise review. *Applied Physics Reviews* **6** (2019).

147. Takeda, S. & Furusawa, A. Toward large-scale fault-tolerant universal photonic quantum computing. *APL Photonics* **4** (2019).

148. Schneemann, A. *et al.* Nanostructured metal hydrides for hydrogen storage. *Chemical Reviews* **118**, 10775-10839 (2018).

149. Sakintuna, B., Lamari-Darkrim, F. & Hirscher, M. Metal hydride materials for solid hydrogen storage: a review. *International Journal of Hydrogen Energy* **32**, 1121-1140 (2007).

150. Aceves, S.M., Berry, G.D., Martinez-Frias, J. & Espinosa-Loza, F. Vehicular storage of hydrogen in insulated pressure vessels. *International Journal of Hydrogen Energy* **31**, 2274-2283 (2006).

151. Darvishi, Y. *et al.* Numerical Modeling and Evaluation of PEM Used for Fuel Cell Vehicles. *Materials* **14**, 7907 (2021).